



HAL
open science

Photo-switching of organic monolayers on silicon surfaces

Stefan Klaes

► **To cite this version:**

Stefan Klaes. Photo-switching of organic monolayers on silicon surfaces. Materials Science [cond-mat.mtrl-sci]. Université Paris Saclay (COMUE), 2017. English. NNT: 2017SACLX071. tel-01680118

HAL Id: tel-01680118

<https://pastel.hal.science/tel-01680118>

Submitted on 10 Jan 2018

HAL is a multi-disciplinary open access archive for the deposit and dissemination of scientific research documents, whether they are published or not. The documents may come from teaching and research institutions in France or abroad, or from public or private research centers.

L'archive ouverte pluridisciplinaire **HAL**, est destinée au dépôt et à la diffusion de documents scientifiques de niveau recherche, publiés ou non, émanant des établissements d'enseignement et de recherche français ou étrangers, des laboratoires publics ou privés.

Thèse présentée pour obtenir le grade de docteur délivré par

l'Université Paris-Saclay

préparée à

l'École Polytechnique

École doctorale N° 573 : Interfaces

Spécialité doctorale “Physique”

Par

Stefan Klaes

Photo Isomerization of Organic Photochromes on Silicon Surfaces

Thèse présentée et soutenue à Palaiseau, le 13 octobre 2017

Composition du jury:

François Ozanam	PMC, Palaiseau	Président
Emmanuelle Lacaze	INSP, Paris	Rapporteuse
Vladimir Khodorkovsky	CINaM, Marseille	Rapporteur
Rémi Métivier	PPSM, Cachan	Examineur
Philippe Allongue	PMC, Palaiseau	Directeur de thèse
Catherine Henry de Villeneuve	PMC, Palaiseau	Co-directrice de thèse

Acknowledgement

This work was performed in the *Laboratoire de Physique de la Matière Condensée* (PMC) at École Polytechnique thanks to a generous funding of LabEx Charmmmat.

I would like to express gratitude the members of the jury. In particular I would like to thank my referees Vladimir Khodorkovsky and Emmanuelle Lacaze who wrote a report including diverse suggestions. I am although grateful to Rémi Métivier and François Ozanam for examining my work and for the exciting discussion, remarks and ideas during the defense.

My deep gratitude goes to Philippe Allongue and Catherine Henry de Villeneuve who supervised this work. Philippe taught me a lot about science and the importance of scientific communication. I appreciate his rigorousness as much as his non-conventional humor. I am thankful for all the chemistry that Catherine showed me that was essential for this thesis. I am grateful for her regular help with the surface preparation as well as for her positive and friendly attitude. I am very thankful for the stimulating discussions we had together, often including François, which I will never forget.

sI would like to thank Fouad Maroun for his diverse support and advices about my work in general and nanoparticles in particular; but furthermore for his diplomatic critics, too. I am although grateful to Jean-Noel Chazalviel for our discussions about modeling photochromism on surfaces that led to the Monte Carlo simulation.

I would like to thank Karola Rück-Braun for the synthesis of the fulgimide compounds. I wish like to thank Sergii Snegir, Olivier Pluchery from INSP and Thomas Huhn from the University of Konstanz for their cooperation in attaching diarylethene on silicon surfaces that is finally not mentioned in the manuscript.

For the optimization of the experimental setup I have to thank André Wrack and Didier Lenoir for their mechanical and electronic work. In addition, I would like to thank Lucio Martinelli, who taught me a lot about experimental optics and diverse other fields. I wish to thank my internship students Louis Godeffroy (École Normale Supérieure) and Maverick

Chauwin (École Polytechnique) for their motivated participation in this work.

It is a pleasure to work in PMC and therefore I wish to thank many people for the working atmosphere: Anne Marie Dujardin her friendly and diligent help with everything concerning administration, Hongye for spreading a positive mood, Timothy for his friendliness, Brendan for being a chemistry adviser and gaming companion, my running team-mates Marco and Bon-Min, Yann for his mathematical propositions and many others, but naming everyone would clearly go beyond the scope of this acknowledgment.

Furthermore, I have to thank Johannes, Christin and Andres for their discussions and support during the defense. I would like to thank my family for their backing and everything they did for me. Last but not least, I have especially to thank Morgane for reminding me that science is not everything in life.

Contents

Resumé	1
General Introduction	5
Motivation	5
Molecular switches	5
Photochromic molecules	6
Photochromism of thin films	9
Photochromism in 2D monolayers	9
Photo-isomerization monitoring	10
Aim and Outline of the present work	11
1 Experimental Details	15
1.1 Introduction	15
1.2 Fulgimides	15
1.3 Preparation and characterization of fulgimide monolayer	16
1.3.1 Experimental procedures	16
1.3.2 Qualitative surface composition	19
1.3.3 Quantitative surface composition	21
1.4 Diluted photochromic monolayers	25
1.4.1 Amidation kinetics	26
1.4.2 Procedures	27
1.4.3 Quantitative surface composition	28
1.4.4 Surface topography	30
1.5 Experimental setup and procedures	32
1.5.1 Experimental setup for photo switching on surfaces	32
1.5.2 Experimental setup for photo switching in solution	32
1.5.3 Light flux calibration on surfaces and in solution	33
1.5.4 Influence of the light pulse duration	35
2 Photo-Switching Properties of Fulgimides in Solution	39
2.1 Introduction	39
2.2 Results	43
2.2.1 First commutations of as received C fulgimide	43
2.2.2 Isomeric composition at the photo stationary states	45
2.2.3 Photo degradation	47
2.2.4 Photoswitching kinetics	48
2.2.5 Isomerization cross section	50
2.2.6 Quantum efficiency	54
2.3 Discussion	56
2.4 Conclusion	58

3	Influence of the Light Polarization on Photo-Switching Properties of Fulgimide Monolayers	59
3.1	Introduction	59
3.2	Electromagnetic environment in different systems	64
3.3	Methodology of the data analysis	66
3.3.1	Quantitative monitoring of the photo switching	68
3.3.2	Determination characteristic parameters of the photo switching	70
3.4	Results	76
3.4.1	Isomeric composition at the photo stationary states	76
3.4.2	Photo degradation	77
3.4.3	Isomerization kinetics of successive commutations	78
3.4.4	Determination of the isomeric composition at the photo stationary states for different surface densities	79
3.4.5	Influence of the fulgimide density on the cross section	80
3.4.6	Light dependence of the photo-switching	81
3.5	Discussion	83
3.5.1	Influence of the surface density on the photo commutation	83
3.5.2	Polarization dependent isomerization	84
3.5.3	Isomerization transition dipole	84
3.6	Conclusions	87
4	Influence of Temperature on the Photo Commutation of Fulgimides on Silicon Surfaces	89
4.1	Introduction	89
4.2	Temperature influence on the switching kinetic	90
4.3	Monte Carlo simulations of the photo-switching of fulgimide on surfaces	95
4.3.1	Reaction mechanism for the ring opening reaction	95
4.3.2	Methodology	98
4.3.3	Results of the Monte Carlo simulation	102
4.4	Conclusions	106
5	Influence of Gold Nanoparticles on the Photo Commutation of Fulgimide Monolayer on Silicon Surfaces	107
5.1	Introduction	107
5.2	Preparation and characterization of gold nanoparticles monolayers	110
5.2.1	Gold nanoparticles synthesis and characterization	110
5.2.2	Surface preparation and characterization	111
5.3	Results	116
5.3.1	Infrared sensitivity	116
5.3.2	Qualitative kinetics	117
5.3.3	Kinetic parameters of the ring closing reaction	119
5.3.4	Kinetic parameters of the ring opening reaction	120
5.4	Discussion	125
5.4.1	Influence of the AuNP on the photo commutation	125
5.4.2	Dielectric environment of AuNP on Silicon	125
5.4.3	Influence electric field enhancement on the photo commutation	130

5.5	Conclusions	135
	General Conclusion	137
A	Supplementary Information for Chapter 1	141
A.1	Basic principle	141
A.2	Quantitative analysis	142
B	Supplementary Information for Chapter 3	147
B.1	Disappearance of impurities during successive commutations	147
B.2	Inert atmosphere FTIR-cell	148
B.3	Analytical models for the switching kinetics	149
B.4	Polarized switching	151
B.5	Perpendicular illumination with and without polarizer	152
C	Supplementary Information for Chapter 4	153
C.1	Temperature dependent setup	153
C.2	Temperature calibration	154
C.3	Determination of the temperature before illumination	155
C.4	Temperature during the irradiation	156
C.5	Experimental procedure for temperature dependent measurements	158
C.6	Differential equation for the ring opening reaction	159
C.7	Numerical solution of the differential equation	160
C.8	Monte Carlo simulations with different parameter	162
D	Supplementary Information for Chapter 5	165
D.1	Influence of separate plasmon excitation on the photo commutation	165
D.2	Temperature influence during the photo commutation	168
	Bibliography	169

List of Figures

1	Operation principle of a molecular switch	6
2	Examples of photochromes	7
3	Schematic photo isomerization for azobenzene	8
4	Schematized photochromism of organic monolayers	10
5	Switching kinetic measured by Henry de Villeneuve et al.	12
6	Switching kinetic measured by Schulze et al.	13
1.1	Multi-step protocol for fulgimide monolayer	16
1.2	Infrared absorbance after the different preparation steps	20
1.3	Infrared absorbance of C and E fulgimide	22
1.4	Fit of the infrared absorbance of carboxylic acid	23
1.5	Fit of the infrared absorbance of the succinimidyl ester	24
1.6	Fit of infrared absorbance of C fulgimide monolayer	25
1.7	Preparation of dilute fulgimide monolayer	26
1.8	Amidation kinetics	27
1.9	Infrared absorbance of monolayer with different densities	28
1.10	Different fulgimide densities vs. amidation solution	29
1.11	Topography of hydrogenated silicon	30
1.12	Topography carboxylic acid monolayer	31
1.13	Topography AFM images of a dilute fulgimide monolayer	31
1.14	Experimental illumination setup	33
1.15	Setup for the calibration measurement of the beams	34
1.16	Temporal development of the intensity of light pulses	36
2.1	Photochromism of indolyl fulgimide	39
2.2	Franck–Condon diagram for the ring opening reaction	41
2.3	UV-vis absorbance of Fulgimide	44
2.4	Reconstructed C fulgimide absorbance	44
2.5	PSS determination	46
2.6	Photo degradation	47
2.7	Determination of switching kinetics	48
2.8	Different kinetic curves of the ring opening reaction	49
2.9	Different kinetic curves of the ring closing reaction	50
2.10	Cross section of the ring closing reaction	51
2.11	Cross section of the ring closing reaction	52
2.12	Cross sections of the different isomerization cycles	53
2.13	Cross sections for 590 and 655nm	54
2.14	Reaction paths for the indolyl fulgimide under irradiation	57
3.1	Different strategies for photochromic monolayers	60
3.2	Electric field at the surface	65

3.3	Pure C and E fulgimide IR absorbance	67
3.4	Change of infrared absorbance due to visible illumination	67
3.5	Relative advancement of the commutation (1)	68
3.6	Relative advancement of the commutation (2)	69
3.7	Calibration of the number of switched isomers	69
3.8	Photo switching for different light fluxes	70
3.9	PSS estimation for dense C monolayer	71
3.10	PSS estimation for dilute C monolayer	72
3.11	PSS estimation under UV light	73
3.12	Numerical cross section for the ring opening reaction	73
3.13	Cross section determination by linear regression	74
3.14	Determination of the cross sections under UV light	75
3.15	Isomeric composition at the PSS for successive isomerizations	76
3.16	Photo-degradation on surfaces	77
3.17	Successive photo commutation cycles	78
3.18	Numerical cross section of successive isomerizations	79
3.19	Cross section for successive isomerization cycles	79
3.20	Isomeric composition at the PSS	80
3.21	Numerical cross sections for different surface densities	81
3.22	Cross section for different polarizations	82
3.23	Alignment of the C, E and Z fulgimide	83
3.24	Cross sections vs E-field intensity	85
3.25	Ratio of normalized cross sections	85
3.26	Transition dipole	86
4.1	Cross sections of the different isomerization cycles	90
4.2	Thermal influence on the photo switching	91
4.3	Arrhenius plot for the ring opening and closing reaction	92
4.4	Numerical cross sections at different temperatures	92
4.5	Numerical cross section and activation energy	93
4.6	Reaction paths for the ring opening reaction	95
4.7	Different activation energies in different environments.	96
4.8	Fulgimide alignment on silicon surfaces	97
4.9	Simulated commutations of fulgimide monolayer	100
4.10	Estimation of the PSS for the Monte Carlo simulation	101
4.11	Comparison experiments - simulation: dilute monolayers	102
4.12	Isomeric composition of PSS for different densities	103
4.13	Comparison: different temperatures	104
4.14	Comparison: different initial isomeric composition	104
5.1	UV visible spectrum of the AuNP	111
5.2	Size distribution of AuNP	112
5.3	Preparation cycle for gold nanoparticle monolayer	112
5.4	SEM: repetitive drop casting	113
5.5	SEM: fulgimide monolayer covered by AuNP	114
5.6	SEM: defects of AuNP-monolayer	114
5.7	Surface plasmon of AuNP	115
5.8	Infrared absorbance of AuNP	117
5.9	Photochromism with AuNP	118
5.10	AuNP influence on ring closing reaction	120
5.11	AuNP influence on ring opening reaction	121

5.12 AuNP influence on different polarizations	122
5.13 AuNP influence on ring opening reaction (655nm)	123
5.14 Calculation of E_{\parallel} at the silicon surface with AuNP	127
5.15 Calculation of E_{\perp} at the silicon surface with AuNP	128
5.16 Electric field enhancement for different zones	129
5.17 Numerical cross section: p polarized light	131
5.18 Numerical cross section: s polarized light	132
5.19 Zoom on kinetic hotspot (C→E)	133
A.1 IR calibration: absorbance of succinimidyl ester	145
A.2 IR calibration: integrated ester peaks	145
B.1 Removal of species during first UV irradiation.	148
B.2 Inert atmosphere FTIR-cell	148
B.3 Analytical models for switching kinetics (1)	149
B.4 Analytical models for switching kinetics (2)	150
B.5 Kinetic for diverse reactions, polarizations and densities	151
B.6 Switching kinetics with and without polarizer	152
C.1 Temperature calibration: thermal cell	153
C.2 Temperature calibration: silicon infrared bands	155
C.3 Temperature calibration: heated sample	156
C.4 Temperature calibration: during illumination (1)	157
C.5 Temperature calibration: during illumination (2)	158
C.6 Differential equation: solution cross section	160
C.7 Differential equation: kinetic curve	161
C.8 Parameter influence on Monte Carlo simulation (1)	162
C.9 Parameter influence on Monte Carlo simulation (2)	162
C.10 Parameter influence on Monte Carlo simulation (3)	163
D.1 Separature plasmon: ring closing reaction	166
D.2 Separature plasmon: ring opening reaction	167
D.3 Sample temperature during illumination with AuNP	168

List of Tables

1.1	Infrared bands of open and closed fulgimide	21
1.2	Light flux calibration in solution	35
1.3	Light flux calibration on surfaces	35
2.1	Isomeric composition at the visible and UV PSS	46
2.2	Cross sections and quantum efficiencies	55
2.3	Reaction rates per photon	57
3.1	Dielectric function of silicon	66
3.2	Local electric field intensities at the surface	66
3.3	Isomeric composition at the PSS	80
3.4	Cross sections for the ring opening and closing reaction	81
3.5	Cross sections for different polarizations	82
4.1	Cross sections for different temperatures	91
4.2	Monte Carlo simulation parameters	99
5.1	Cross sections with and without AuNP	123
5.2	Isomer contribution to measured absorbance	129
C.1	Experimental parameter for switches at different temperatures	158

List of Abbreviations

AFM	Atomic Force Microscopy
ATR	Attenuated Total Reflection
DAE	Diarylethene
DFT	Density Functional theory
EDC	N-(3-Dimethylaminopropyl)-N-ethylcarbodiimide
FTIR	Fourier Transformed Infrared Spectroscopy
MC	Monte Carlo
NHS	Nydrsuccinimide
PSS	Photo-Stationary State
SAM	Self Assembled Monolayer
SEIRA	Surface Enhanced Infra Red Absorbance
SEM	Scanning Electron Microscopy
SERS	Surface Enhanced Raman Spectroscopy
SFG	Sum Frequency Generation
SHG	Second Harmonic Generation
SPR	Surface Plasmonic Resonance
THF	Tetrahydrofuran
UV	Ultraviolet
vis	visible
XPS	X-ray Photoelectron Spectroscopy
k_B	Boltzmann constant
k_i	rate constant
T	Temperature
ϕ	Photon Flux
η	Quantum efficiency
σ	Photo isomerization cross section
σ_{abs}	Absorbance cross section
ν_a	Asymmetric stretch
ν_s	Symmetric stretch

Resumé

Les photochromes organiques sont des molécules qui peuvent commuter de manière réversible entre différentes conformations structurales par absorption de lumière. Les changements structuraux induits par illumination s'accompagnent en général d'une modification de leurs propriétés optiques. Parmi différentes familles, les composés indolyl fulgimide présentent des propriétés potentiellement intéressantes en vue de leur utilisation comme commutateurs optiques. En solution, l'illumination UV-Vis de ces composés permet de commuter de façon réversible entre deux types d'isomères thermiquement stables: des formes ouvertes (E,Z) et des formes cycliques fermées (C) qui présentent des bandes d'absorption bien séparées dans le domaine UV-Vis et en IR.

Dans ce travail nous nous sommes intéressés aux propriétés de photo-commutation de ces composés immobilisés sur des surfaces. Des isomères (E,Z) ou (C) ont été ancrés de façon covalente sur des surfaces de silicium pré-fonctionnalisées par des monocouches organiques. La cinétique de photo-commutation des monocouches de fulgimides a été étudiée *in situ* par spectroscopie FTIR en fonction de la densité de fulgimides et des conditions d'illumination (intensité et polarisation) et a été comparée à celle observée en solution.

Le manuscrit est conçu comme suit :

Le **chapitre 1** présente les principales techniques expérimentales utilisées dans cette thèse. L'approche développée pour la préparation de monocouche avec des densités de fulgimides variables est décrite. La composition chimique en surface (concentration en fulgimides) est déterminée par spectroscopie infrarouge à transformée de Fourier en géométrie ATR.

La topographie des monocouches est examinée par microscopie à force atomique. La deuxième partie du chapitre présente le dispositif expérimental qui a été spécifiquement développé pour l'illumination et le suivi *in situ* de la photocommutation sur les surfaces de silicium par spectroscopie FTIR.

Le **chapitre 2** présente une étude approfondie de la photocommutation des fulgimides en solution (acétonitrile). Dans cette étude, des conditions d'illumination similaires à celles utilisées pour étudier la commutation sur les surfaces, ont été utilisées de façon à pouvoir comparer les processus d'isomérisation (cinétique, composition isomériques aux états photostationnaires) et évaluer l'influence de l'environnement (surface ou solution) sur la photo-isomérisation. L'efficacité des isomérisations $C \leftrightarrow E$ (sous lumière visible) et $E \leftrightarrow C$ (sous lumière UV) a été évaluée en calculant les sections efficaces en solution pour chacune des réactions.

Le **chapitre 3** est dédié à l'étude des monocouches de fulgimides sur les surfaces de silicium. La photocommutation a été étudiée en fonction de la densité de fulgimides, et en faisant varier les conditions d'illumination (intensité et polarisation). La composition isomérique aux états photostationnaires et les paramètres cinétiques ont été déterminés à partir de mesures par spectroscopie FTIR. Les résultats montrent que 100% des fulgimides sont commutables en dessous d'une densité critique. Au-dessus, les résultats montrent qu'une fraction des fulgimides ne commute pas à cause d'effets stériques. Des sections efficaces d'isomérisation plus faibles sont observées sur les surfaces et varient en fonction de la polarisation. Il est montré que les différences observées - surface *versus* solution ou selon la polarisation - s'expliquent par des environnements diélectriques différents et donc des intensités différentes du *champ électrique local*. Par ailleurs, un effet d'orientation des photochromes est également mis en évidence.

Dans le **quatrième chapitre**, la photocommutation des fulgimides est mesurée en fonction de la température. Nous avons mis en évidence que

la réaction de cyclisation $E \leftrightarrow C$ (sous UV) ne dépend pas de la température, alors que la réaction inverse $C \leftrightarrow E$ (sous la lumière visible) est activée thermiquement et que l'énergie d'activation associée n'est pas constante mais augmente au cours de la commutation. Des simulations Monte Carlo prenant en compte l'environnement moléculaire local variable des fulgimides (type d'isomère au voisinage) au cours de l'isomérisation permettent de rendre compte des variations d'énergie d'activation et de section efficace observées expérimentalement.

Dans le **cinquième chapitre**, l'effet d'une augmentation du champ électrique local a été étudié. Pour cela des nanoparticules d'or ont été déposées au-dessus de la monocouche des fulgimides pour induire une amplification locale du champ électrique par résonance plasmon. En illuminant avec une longueur d'onde dans la bande d'absorption des plasmons des nanoparticules d'Or ($\lambda = 690\text{nm}$), un phénomène d'augmentation des sections efficaces a été mis en évidence qui dépend de la polarisation. Les amplifications observées expérimentalement sont interprétées de façon quantitative par des calculs numériques d'intensité du champ électrique au voisinage des nanoparticules d'or.

En conclusion, une approche expérimentale a été couplée à des simulations théoriques pour étudier l'influence de l'environnement sur les processus de photo-isomérisation de fulgimides immobilisés sur des surfaces de silicium. Ce travail montre que les propriétés diélectriques en surfaces et l'organisation moléculaire influencent de manière décisive la cinétique d'isomérisation.

General Introduction

Context

A molecular switch is a molecule that can reversibly be switched between two or more (meta-) stable forms. Certain functionalities are achieved by the change of the molecular state. The switching process is excited by an external stimuli, for example light, temperature, pH or electric current.

In fact molecular switching is a basic concept found in nature. A prominent example is the molecule Rhodopsin that is present in the human vision process [1, 2]. Rhodopsin undergoes structural changes due to the absorption of light. This is the first step of the visual phototransduction in which light is converted to an electric signal to inform our brain that our eyes see visible light.

The example of the human vision illustrates the interest of molecular switches. Consequently the chemical and physical research on switchable molecules is very active due to many potential applications. Switchable molecules modify the properties of a material if they are anchored to its surface. Possible applications of switchable molecules on surfaces are for example data and signal progressing [3–5], optical switches [6], switchable catalysis [7], cell culturing [8], data storage [9], micro-fluids [10] etc.

Molecular switches

A molecular switch is a molecule that exhibits at least two stable or more meta-stable forms and transitions between these forms exists, as displayed in figure 1. The molecule is in its ground form a and another stable or meta-stable form b exists. The transition from one form to the other can be

induced by the absorption of a photon or by electron injection, but other external stimuli, e.g. pressure, are existing, too. Thermally activated transitions are possible depending on the energy barrier between the two forms.

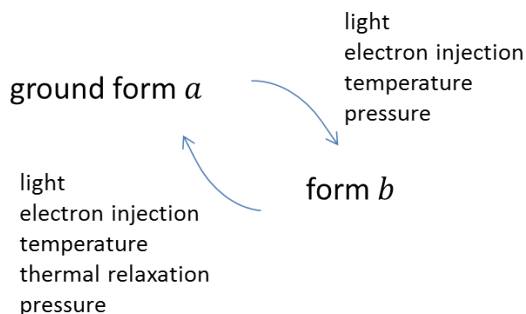


FIGURE 1: Operation principle of a molecular switch

The different forms of the molecule exhibit different properties, in particular optical properties as color (different visible absorbances), but furthermore, conductivity, geometry, dipole moments, refractive indices, electric polarizability and magnetic susceptibility may be different for the two forms.

Photochromic molecules

Photoswitchable molecules are molecular switches whose transitions are induced by the absorption of light. Photochromic molecules undergo a change in their color (chromic) by the absorption of light (photo). These molecules may be colorless in the energetically lower form and can be switched by the absorption of UV light to the colored form.

Two kinds of photochromes are distinguished: P- and T-type (photon and temperature). In P-type photochromes the energetically higher form *b* is thermally stable and therefore the back switching must be induced by a visible photon. In T-type photochromes the colored form *b* is not thermally stable and therefore the photochrome can spontaneously relax to the ground-form. This is represented by the height of the energy barriers E_B of the meta stable form with respect to the room temperature (T-type: $E_B \approx k_B T$; P-type: $E_B \gg k_B T$).

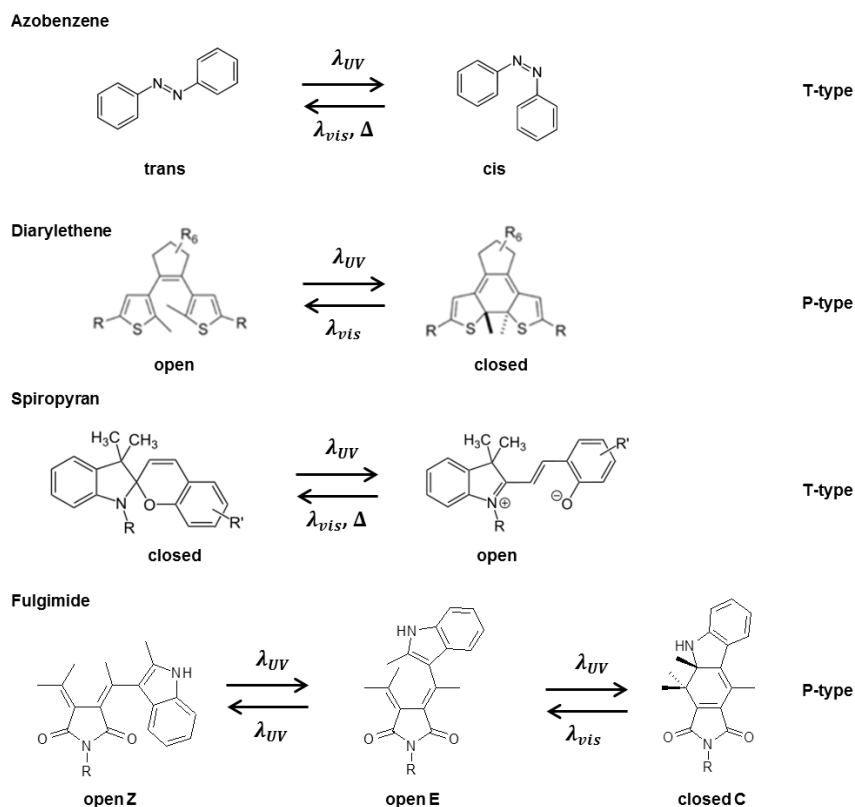


FIGURE 2: Examples of photochromes

Different photochromic compounds are existing (figure 2), the most famous being azobenzene. The chemical transformation of the azobenzene (T-type) consists of a trans cis isomerization around the double N=N bond which induces a large change in the dipole moment and prompted many studies of this system[11].

The reaction mechanism of azobenzene has been studied by pumped femtosecond spectroscopy [12–14]. The reaction mechanism for the trans→cis isomerization is shown in figure 3 [15, 16]. Two pathways for the trans→cis isomerization are available, by rotation around the N=N double bond or by inversion. Due to the absorption of a photon the closed isomer is excited from the trans form into a Franck Condon state on the S_2 or S_1 energy sphere. It then reaches a hybridized transition state. From the transition state two reaction channels are available, internal conversion back to the trans form or the trans→cis isomerization to the cis form. However, cis-azobenzene is not stable at room temperature and thermal back isomerization to the trans isomer occurs (T type). Therefore azobenzene like other

P type photochromes is not suitable for applications where thermal stability is required in both forms. Furthermore, the lack of thermal stability represents a significant burden for the study of the photo-switching kinetics of photochromes in different environments.

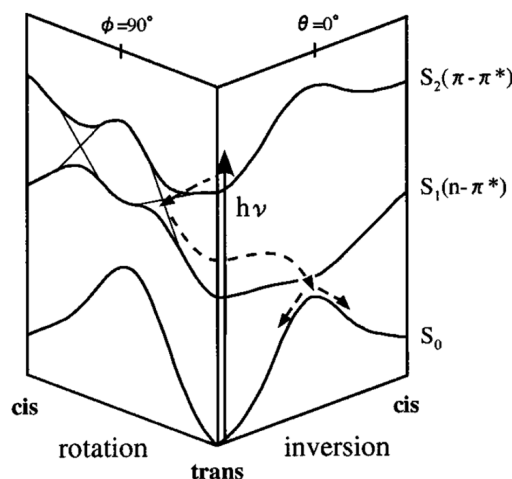


FIGURE 3: Schematic photo isomerization process for azobenzene taken from [12]

Other photochromic molecules are often switched from one form to the other by the rotation around a double bond or by a ring opening and ring closing reaction. The photo-isomerization of diarylethene and fulgimide (P-type) consist of the ring opening of cyclohexadiene to a hexatriene backbone or the reverse closing reaction. In spiropyran (T-type) the fragile carbon oxygen bond can be broken and again a ring opening reaction is obtained. In all cases to leave the ground form UV light is necessary and the back isomerization can be excited by visible light. Among photochromes, fulgimides are known to be resistant to fatigue upon repeated UV-Vis irradiation cycles [17, 18]. Depending on the side groups of the fulgide or fulgimide 10^4 switching cycles have been observed and therefore they can represent a very fatigue resistant molecular switch [19].

Many different systems consisting of several photochromic compounds have been designed. Photochromes can be bound to form dimers or polymers and thereby their photochromic properties may be coupled [20–22]. The photochromism can be significantly affected when a transition metal is coupled to photochromic compound [23–25]. Furthermore, the coupling

of photochromes with metallic nanoparticles is an emerging research field [26–31]. Even organic nanoparticles consisting of organic photochromes have been designed [32, 33].

Photochromism of thin films

Above mentioned photochromes have been incorporated in polymers to obtain thin films with photochromic properties. However, for photochrome based devices such as optical memories, it is desirable to immobilize the photochrome at the surface. Thin layers containing photochromes may be prepared by spin coating, Langmuir–Blodgett or layer-by-layer method [34, 35]. An alternative approach consists in binding photochromes on a surface. In this case, controlling the binding of the absorbed molecule and the substrate is critical for the switching behavior.

Photochromism in 2D monolayers

Many studies have also considered 2D monolayers of photochromes and showed that the molecule's electronic properties and structure may be influenced by coupling with the substrate. For instance, the potential energy surface in figure 3 in ultrahigh vacuum is significantly changed for photochromes absorbed on metal surfaces [36]. Two photons experiments have also demonstrated that the structure of excited state may be different at surfaces and in solution. As a result, photoswitching is often strongly impacted or even suppressed for compounds immobilized on a surface. For example, the switching ability of azobenzene is suppressed for azobenzene directly absorbed on gold substrates [37, 38]. The photo switching is restored by intercalating a spacer between the photochrome and the metallic surface to reduce electronic coupling with the substrate [39]. Different methods have been employed, the most popular one being the introduction of a functionalized self-assembled monolayer of thiols on gold surfaces (see figure 4). A more extended literature survey will be given in chapter 3.

Other studies considered semimetals like bismuth [40] to modify electronic coupling and these showed that PS is more efficient than on metallic substrates.

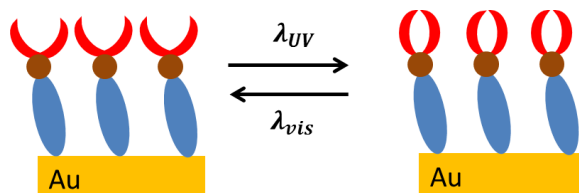


FIGURE 4: Schematized photochromism of organic monolayers on Au surface modified with a functionalized SAM of thiols to immobilized the photochromes on the substrate.

Photo-isomerization monitoring

In solution the photo-isomerization of photochromes can easily be measured by UV visible photo-spectroscopy because of the distinguishable visible absorbances of the different isomers. Immobilized on surfaces the readout of the photo commutation is more challenging due to the limited amount of photochromic compounds (ca. $1 \cdot 10^{-10}$ mol/cm²). Since numerous properties change due to the photo switching diverse measurement methods are used to monitor the switching kinetics. For example the isomerization of single molecules can be measured by scanning tunneling microscope [41], the global isomerization can be monitored by contact angle measurements [10], but both techniques do not allow studies of the switching kinetics of the monolayer. The photo-isomerization can be measured exploiting optical properties in the infrared, visible and high energy regions using different spectroscopies (infrared, Raman, visible absorption, X-ray etc.). An more detailed overview of the different measurement methods is given in the introduction in chapter 3.1.

The literature shows that photo-switching properties of photochromes attached surfaces are generally different with respect to those measured in solution. These are often explained by the particular environment of the photochromes at the surface. Steric hindrance is very often invoked but electronic coupling between substrate and photochrome and/or between

photochromes plays a role, too. This has justified the different strategies to uncouple the photochromes from the metallic surfaces, by introducing a spacer (often a self-assembled monolayer) or the use of semi-metals such as Bi [40] and semiconductors [42]. Nonetheless, disentangling of the different factors is difficult and, as will be shown later, requires a better precision while monitoring the photo-commutation.

Aim and outline of the present work

The very good thermal stability of fulgimides makes them good model systems to investigate above mentioned effects. These compounds have been synthesized in Japan in 1991 [43] and have been considered as potential molecular memories and switches [44]. The mechanisms of photo-isomerization were vastly investigated in liquid solutions [45–48] using pump-probe techniques [47, 49] because photo-isomerization is very fast (100 ps time scale). Temperature dependent studies in solution showed fulgimide photo-isomerization follows a complex energy landscape. Thermal stability of fulgimides was exploited to create logic gates [50, 51], memories and logic devices by incorporating them in polymer films [6, 9, 52–54].

Studies of fulgimide photoswitching on surface are very recent and were all conducted after their immobilization on a functionalized silicon substrate [55–58]. In all these works fulgimides were modified with an amino linker to anchor them via a peptide covalent bond on an acid terminated alkyl monolayer. The photo-isomerization was characterized by FTIR [55, 56, 58], XPS [56] and very recently by SHG [57]. Data essentially demonstrated the reversible photo-isomerization of fulgimide monolayers between two PSS, named as such because the monitoring signal was no longer depending on time or the photon dose. The exact isomeric composition at PSS was however not determined except in [55, 58] and data allowed postulating that some photochromes remain 'frozen' or inactive when the surface density exceeds a critical density. The photo-isomerization of fulgimides on silicon surfaces was first monitored by FTIR

by Henry de Villeneuve et al. [55] (see figure 5). Additional preliminary investigations as a function of surface density of immobilized fulgimides have been conducted in [55, 58]. These works showed that the photoswitching is much slower than in solution and that it does not obey a first order kinetic law. Nonetheless, a recent study, using SHG [57], reported a first order kinetic law with an effective cross sections ($2.3 \cdot 10^{-18} \text{ cm}^2$ (UV: E \rightarrow C) and $1.2 \cdot 10^{-18} \text{ cm}^2$ (Vis: C \rightarrow E)) as large as those measured in solution.

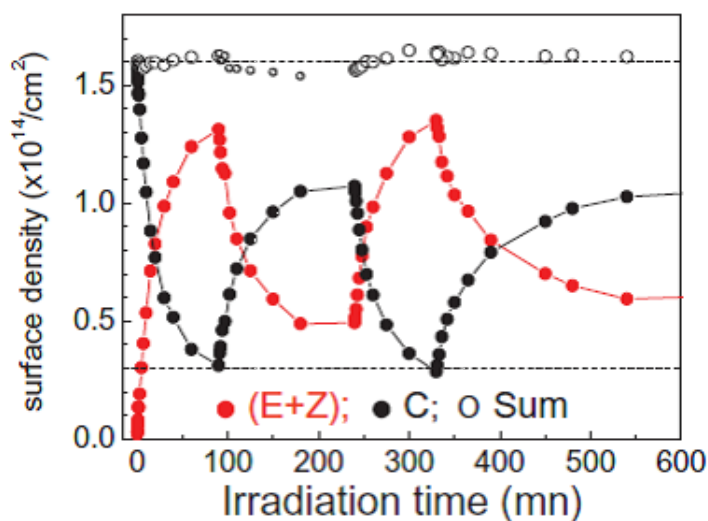


FIGURE 5: Time dependence of isomeric composition of a fulgimide monolayer on Si(111). The first few cycles are shown. Figure taken from [55]

All in all, one knows that (i) fulgimide monolayers can be reversibly switched between two photo stationary states and (ii) that the isomeric composition at PSS seems to depend on the surface density of immobilized fulgimides. However, there is some disagreement about photo-isomerization characteristics (cross sections and kinetic law) which needs to be revisited. In this work the photo-isomerization of fulgimides on silicon surfaces is investigated using calibrated FTIR [55, 58]. To vary the surface density of fulgimide a new approach is introduced in chapter 2 which is more flexible than the previous approach used in the group [58]. In addition, a new experimental approach to control the photon dose has been implemented (see chapter 1) and a new data analysis was also developed (see chapter 3). Both help to greatly enhance the precision on determination

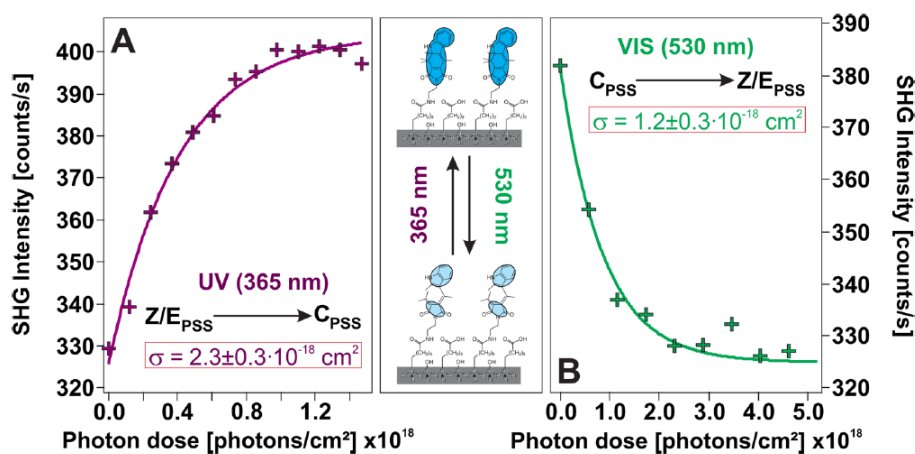


FIGURE 6: Changes in the SHG signal amplitude as a function of photon dose for a fulgimide monolayer on Si(111). (A) Increase of the SHG intensity as a function of photon dose at $\lambda = 365 \text{ nm}$ corresponds to the ring-closure reaction ($E/Z_{PSS} \rightarrow C_{PSS}$). (B) SHG intensity decrease as a function of light exposure at $\lambda = 530 \text{ nm}$ due to the ring opening (figure reproduced from [57])

of the effective cross sections.

Thanks to these new tools, the effective cross section σ and PSS may be measured with sufficient precision to discuss the influence of light polarization (chapter 3), the influence of sample temperature (chapter 4) and the influence of plasmonic gold nanoparticles (AuNP) absorbed on top of the fulgimide monolayer (chapter 5) on the photoswitching kinetics of fulgimides immobilized of a surface. Chapters 3 and 5 deal in essence with the question of the influence of electromagnetic field, while chapter 4 aims at discussing the energy landscape as well as the impact of the local environment.

Chapter 1

Experimental Details

1.1 Introduction

In the continuity of previous studies carried out in the group [55, 58] fulgimide monolayers were prepared using the multi-step protocol shown in figure 1.1, which was developed in this group [55, 58] based on the protocol of Moraillon et al. [59]. However, in this work we introduce a more reliable and flexible procedure to vary the surface density of the photochromes on the surface (section 1.4) and new experimental set-up for in situ illuminating and monitoring the isomerization process on the surfaces has been developed (section 1.14). The new fully automatized set-ups allow good control of the photon dose and faster FTIR measurements, for a more precise monitoring of the isomerization process in particular in early stage of the process. Calibration of the photon dose on the surface and/or in solution was carefully carried out and the photo-isomerization on the surfaces was compared to photo-isomerization in solution using the same (new) illumination set-up.

1.2 Fulgimides

Fulgimide compounds (powder) were generously supplied by Karola Rück-Braun (TU, Berlin). The synthesis of the compounds and details on their chemical characterizations are reference [56]. As shown in figure 1.1 these compounds are substituted with an amino-linker to immobilize them on the surface. They were packaged under N₂ atmosphere and stored in

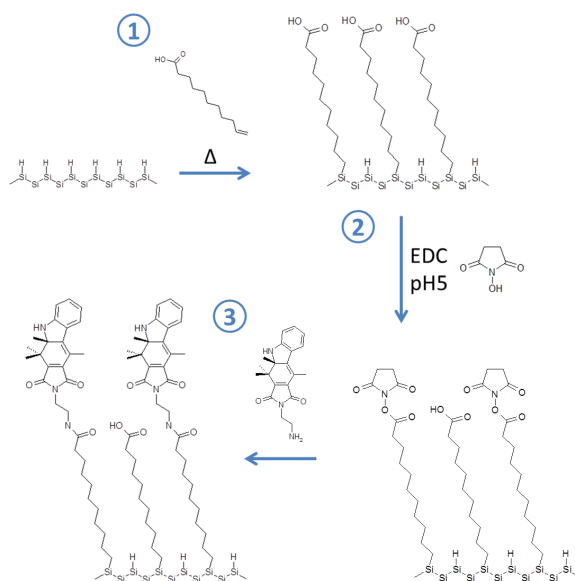


FIGURE 1.1: Multi-step protocol for the covalent linkage of amino-fulgimide onto hydrogenated silicon surfaces. Figure adapted from [55]

the dark at 4°C, and were protected as far as possible from light during the solution preparation and/or once anchored on the surfaces .

1.3 Preparation and characterization of fulgimide monolayer

1.3.1 Experimental procedures

Substrate preparation

N type silicon wafers¹ (Phosphor doped) with an (111) surface orientation of a thickness of 0.50 mm to 0.54 mm have been used as substrates. The (111) surface had a miss-cut of 0.2° towards the (112) direction to obtain terraces after etching. Both sides of the Float-zone silicon have been polished. The samples had a length of 12 mm to 15 mm and a height of 13 mm. The silicon is covered by a thin oxide layer.

The infrared spectroscopy in ATR geometry requires the infrared beam to enter and leave the silicon substrate from the lateral sides. Therefore the lateral sides of the silicon substrate have been polished in an angle of 45°. In ATR geometry around 24 to 30 internal reflections of the infrared beam

¹Siltronix

are obtained. After the polishing the silicon prisms have been cleaned in trichloroethylene, acetone and ethanol to remove traces of wax that has been used in the polishing process.

Silicon etching and hydrogenation

For the grafting of organic monolayers on silicon surface the oxide monolayer needs to be removed to get hydrogenated silicon surface. This can be achieved by chemical etching using fluoride solution (e.g. ammonium fluoride, hydrogen fluoride) [60, 61]. In this work chemical etching has been done using 40% NH_4F to favor anisotropic etching of silicon resulting in regular terraces flat at atomic scale [62].

To do so the silicon substrates are twice exposed to piranha solution using a mixture of 3 volumes 96% of H_2SO_4 to one volume of 30% H_2O_2 for at least 10 minutes. All non metallic materials were cleaned in piranha solution, too. Afterwards the samples are rinsed in copious amounts of ultra-pure water (18.2 $\text{M}\Omega\text{cm}$). Then the silicon is exposed to the 40% NH_4F containing small amounts of $(\text{NH}_4)_2\text{SO}_3$ for oxygen binding during 15 minutes to etch the oxide layer. After etching the substrates are rinsed again in ultra pure water and dried using an argon flow. Finally the sample is stored in an argon atmosphere for at least 10 minutes to dry the last remaining water and wait until its introduction into the grafting solution

Grafting of carboxydecyl monolayer

The grafting of carboxylic acid monolayer (step 1 in 1.1) was done following the protocol developed by Faucheux et al. [63]. 1-undecylenic acid $\text{CH}_2=\text{CH}-(\text{CH}_2)_8-\text{COOH}$ ² reacts with the freshly prepared SiH surface. For the grafting 15 ml undecylenic acid is poured into a Schlenk reactor and then out-gassed by argon at around 40°C for 10 minutes. The temperature is then increased to 100°C under continuous argon flow for at least 30 minutes to eliminate traces of water. Then the solution was let to cool down to 40°C and the hydrogen terminated silicon sample is added. The solution

²99% Acros Organics

and the sample were flushed with Argon for 20 minutes before the Schlenk has been hermetically closed. The grafting is activated by UV light irradiation ($\lambda = 316 \text{ nm}$ with 6 mWcm^{-2}) inside a home-build photo reactor for at least 3 hours.

After the grafting the Schlenk reactor is let to cool down. The sample is removed from the solution and cleaned twice in hot acetic acid at 70°C for around 30 minutes in order to remove residual undecylenic acid physisorbed atop the monolayer by hydrogen bounds [64]. Afterwards the sample is copiously rinsed in ultra-pure water to remove residual acetic acid and blown dry.

Surface activation

This step is required to activate the terminal carboxyl group and enable the linkage of amino-photochromes in soft conditions that preserve the organic photochrome.

For the attachment of amino groups (step 2) the carboxylic acid needs to be transformed to succinimidyl ester ($\text{COOH} \rightarrow \text{COOSuc}$) [59, 65]. To do so the carboxylic acid monolayer is immersed in freshly prepared 0.1 M hydro-succinimide (NHS), 0.1 M N-Ethyl-N'-(3-(dimethylamino) propyl) carbodi-imide (EDC) in MES buffer solution at pH 5.5 for one hour at 15°C under continuous argon flow.

Afterwards the activated surface is successively rinsed in 0.1M NaH_2PO_4 (pH=5), 0.01M NaH_2PO_4 (pH=5) and ultra-pure water for each time 10 minutes at 40°C . Finally the sample is dried using an argon flow.

Anchoring of amino-Fulgimide

The final step of the sample preparation is the linkage of amino-fulgimide by aminolysis of the succinimidyl ester groups.

The amino photochromes are covalently coupled to the surface by reaction with the COOSuc activated surface (step 3). This is achieved by immersion of the COOSuc surfaces into acetonitrile containing 5mM of closed

C or open E/Z amino terminated fulgimide. The Schlenk containing acetonitrile and the fulgimide is then out-gassed for 5 minutes to remove O₂. The Schlenk is closed and the reaction let to proceed for two hours at room temperature. Subsequently the photochromic monolayer is cleaned three times in an acetonitrile bath at 40°C for about 10 minutes and then blown dry. Once prepared, the sample with the fulgimide monolayer are stored in the dark and under nitrogen atmosphere until their characterization or study of their photo commutation properties.

As far as possible all preparations and experiments with the photochromes are performed in the dark.

1.3.2 Qualitative surface composition

The Fourier transformed infrared absorbance spectra (p polarization) after the different preparation steps are shown in the figure 1.2. The reference spectrum for all spectra is the hydrogenated silicon prior to any modification of the same sample. Thereby the positive and negative infrared bands correspond to gained and lost absorption dipoles. The contribution of water vapor on all FTIR is automatically corrected using different reference spectra of water-vapor. A first order polynomial correction of the baseline of the absorption spectra may have been applied if necessary.

The carboxylic acid monolayer after the first preparation step is displayed on top. The negative band at 2083 cm⁻¹ of the carboxylic acid spectrum corresponds to the ν SiH stretching mode and therefore shows loss of SiH bonds. The other negative infrared bands at 2334 cm⁻¹ and 2361 cm⁻¹ correspond to a lower CO₂ content during the carboxylic acid measurement with respect to the measurement of the hydrogenated silicon and can be ignored. The large positive infrared band at 1715 cm⁻¹ belongs to the carbonyl ν C=O stretching of the carboxylic acid. The large infrared bands at 2853 cm⁻¹ and 2922 cm⁻¹ are assigned to the symmetric and asymmetric ν CH₂ stretching modes, respectively. The broadening of the CH₂ peaks is due to the different environments at the beginning, middle and end of the alkyl chain. The infrared bands of silicon oxide are in the interval between

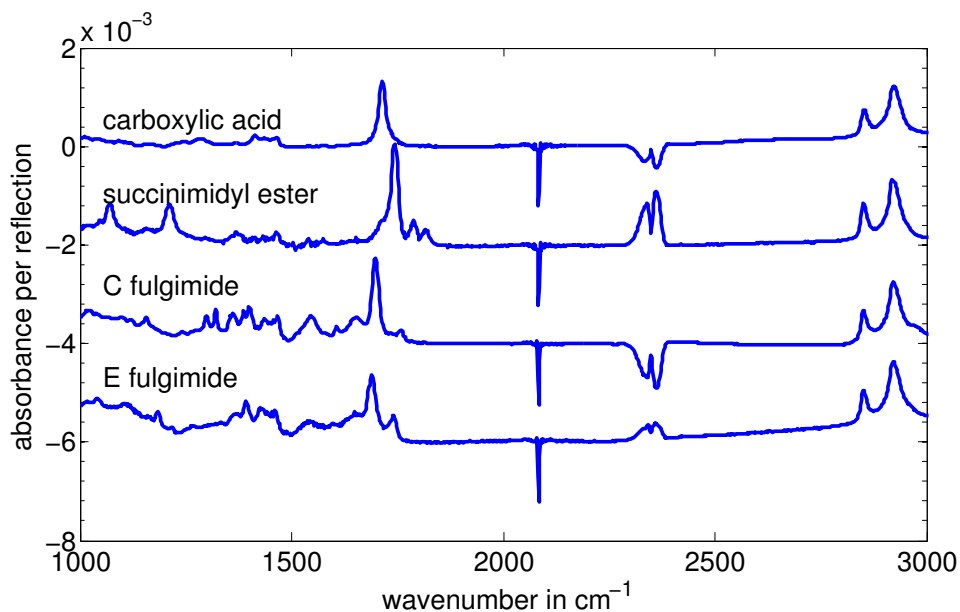


FIGURE 1.2: Infrared absorbance after the different preparation steps in p polarization on Si(111). The freshly etched hydrogen terminated surface served as reference.

1000 cm^{-1} and 1200 cm^{-1} . The loss of the SiH bonds and the gain of the infrared bands corresponding to the carboxylic acid and CH₂ clearly indicates the successful grafting of the undecylenic acid. The absence of any oxidation peaks indicates a good grafting yield. Qualitatively the infrared spectrum corresponds to other infrared spectra reported in the literature [58, 63].

The infrared absorbance after the functionalization of the carboxylic acid monolayer (step 2) is shown in figure 1.2 (second curve). The $\nu\text{C}=\text{O}$ band of the carboxylic acid at 1715 cm^{-1} is replaced by three new bands at 1745 cm^{-1} , 1787 cm^{-1} and 1817 cm^{-1} that are assigned to the three carbonyl groups of the ester and the succinimidyl group. The negative SiH and the CH₂ peaks basically remain unchanged with respect to the carboxylic acid surface after grafting. The three peaks in the carbonyl region indicate successful activation of the carboxylic acid to the succinimidyl ester.

After the fulgimide coupling the IR absorbance spectrum changes significantly between 1200 cm^{-1} and 1800 cm^{-1} . The infrared spectra after aminolysis (step 3) using C and E fulgimide are displayed. Very similar absorbance spectra are obtained for C and E fulgimide monolayer. In the

carbonyl region several bands are present that are listed in table 1.1. The infrared bands are in agreement with measurement of the same components in solution and on surfaces [55, 56, 66]. The bands can be assigned to particular vibrations by density functional theory calculations [66]. The diverse assigned to the fulgimide clearly indicate their presence on the surface. The amide band at 1654 cm^{-1} indicates the covalent bonding of the fulgimide to the surface.

C Fulgimide	E/Z Fulgimide	Band assignment
1546 cm^{-1}	1543 cm^{-1}	$\nu\text{C}=\text{C}$ indolyl ring
1605 cm^{-1}	1595 cm^{-1}	$\nu\text{C}-\text{H}$ phenyl ring
-	1620 cm^{-1}	$\nu\text{C}=\text{C}$ indolyl ring
1654 cm^{-1}	1654 cm^{-1}	$\nu\text{N}-\text{C}=\text{O}$ amide
1698 cm^{-1}	1690 cm^{-1}	$\nu_a\text{C}=\text{O}$ malmeide group
1758 cm^{-1}	1739 cm^{-1}	$\nu_s\text{C}=\text{O}$ malmeide group

TABLE 1.1: Infrared bands of open and closed fulgimide in the carbonyl region

In figure 1.3 the infrared absorbance of closed and open fulgimide monolayer in the carbonyl region is shown. The most significant difference of the infrared absorbance is the asymmetric and symmetric $\nu\text{C}=\text{O}$ of the maleimide group whose peak positions and heights of C and E monolayer clearly differ. For the C fulgimide the asymmetric and symmetric maleimide positions are 1698 cm^{-1} and 1758 cm^{-1} , respectively, for the open E/Z fulgimide the asymmetric and symmetric maleimide positions are 1690 cm^{-1} and 1739 cm^{-1} .

1.3.3 Quantitative surface composition

The surface concentration of the carboxylic acid monolayer has been determined by the FTIR absorbance. This has been done following the procedure developed in this group [59, 63]. For this procedure the integrated infrared absorbance bands at the surface are compared to reference infrared bands of the same compound in solution at known concentrations. For the comparison on surfaces the infrared spectrum needs to be measured in both s and

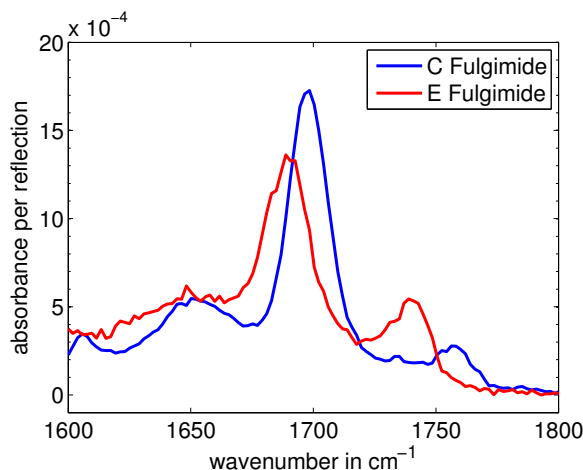


FIGURE 1.3: Infrared absorbance in p polarization of C and E fulgimide monolayer in the carbonyl region. The reference is hydrogenated silicon, both infrared spectra are in p polarization.

p polarization to take normal and perpendicular orientations of the dipoles into account. The absorbance bands are normalized with respect to their electric field in solution or on the surface. Geometrical factors accounts the isotropy in solution or the anisotropy on silicon. The method is explained in detail in the annex [A.2](#).

In figure [1.4](#) the $\nu\text{C}=\text{O}$ peak of the carboxylic monolayer is displayed. For the determination of the surface concentration of the carboxylic acid groups the integrated peaks needs to be compared to solution. The blue curve shows the measured absorbance, the thin black lines the individual peaks and the red curve the addition of the peaks. A Voigt profile has been fitted to the $\nu\text{C}=\text{O}$ peak centered at 1714 cm^{-1} . A small shoulder is added to take impurities corresponding to ester groups $\nu\text{C}=\text{O}$ at 1740 cm^{-1} . Not respecting the shoulder increases the integrated absorbance by only 1%. The absorbance spectrum measured by an s polarized infrared beam is very similar and fitted in the same way.

The surface density for the acid monolayer shown in the figure is $2.8 \cdot 10^{14}\text{ cm}^{-2}$ which corresponds to 2.8 carboxylic acid per nm^2 . The surface densities for all examined samples are between $2.6 \cdot 10^{14}\text{ cm}^{-2}$ and $2.9 \cdot 10^{14}\text{ cm}^{-2}$, the shown absorbance is therefore representative. These values are in agreement with previously determined surface concentrations of

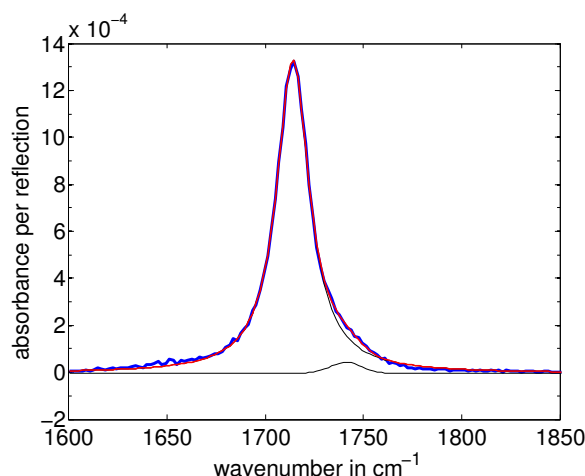


FIGURE 1.4: Infrared absorbance of carboxylic acid in p polarization on Si(111) in the carbonyl region. The blue curve corresponds to the measured absorbance and the red line shows the fitted absorbance. The individual fits are shown in black

carboxylic acid monolayers [58, 59, 63]. Compared to the number of SiH bonds sites available onto of the Si(111) surface ($7.8 \cdot 10^{14} \text{ cm}^{-2}$) this corresponds to a coverage of around 33% to 37%.

The determination of the surface density of the succinimidyl ester layer is particularly important because not only the succinimidyl ester surface characterized by this procedure but the number of photochromes is determined by the number of disappeared succinimidyl ester groups, too. However, the three infrared bands in the carbonyl region at 1745 cm^{-1} , 1787 cm^{-1} and 1817 cm^{-1} strongly overlap. Furthermore, the 1745 cm^{-1} band has a significant shoulder towards lower wavenumbers. Diverse optimized parameter give similar χ^2 resulting in significant incertitudes on the surface density. Therefore the new fitting procedure introduced before has been used to stabilize the procedure.

The overlap of the succinimidyl ester on surfaces is much stronger than in solution due to the band widening in molecular crystals. In solution the bands are well separated and can be fitted without problems. The ratio of the integrated peaks of the three different carbonyl bands has first been determined in solution. On surfaces the succinimidyl ester is then fitted with a self made fitting program that conserves the ratios determined in solution.

This is explained in detail in the annex. Thereby succinimidyl ester densities of between $2.0 \cdot 10^{14} \text{ cm}^{-2}$ and $2.4 \cdot 10^{14} \text{ cm}^{-2}$ have been determined indicating a successful activation of 70% to 85% of the acid groups.

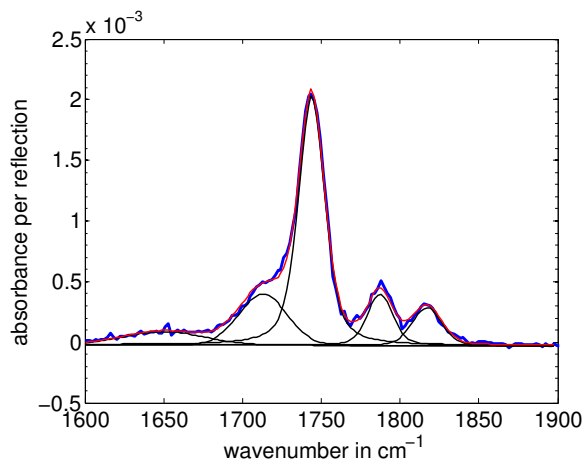


FIGURE 1.5: Infrared absorbance of the succinimidyl ester in the carbonyl region measured by p polarized infrared

The surface density of the fulgimide monolayer is determined by the number of disappeared succinimidyl ester groups. In figure 1.6 the fulgimide absorbance of a as prepared C monolayer is shown using the succinimidyl ester monolayer before amidation as reference. Thereby the infrared bands at 1745 cm^{-1} , 1787 cm^{-1} and 1817 cm^{-1} are negative and the bands corresponding to the fulgimide are positive. Non-activated acid groups are canceled out to the ester reference. The spectrum shows the absorbance by a p polarized infrared beam, a similar result is obtained for the beam in s polarization. The fitting of this monolayer is particularly challenging because of the strong overlap of the different bands. Therefore for the fitting of the disappeared succinimidyl ester groups the same peak positions and widths have been used as before. Furthermore, again the ratios between the three peaks are fixed by the calibration in solution. Thereby the degrees of freedom are significantly reduced and the fit is more robust. For the monolayer whose infrared spectrum in p polarization is shown the number of disappeared succinimidyl esters is $1.8 \cdot 10^{14} \text{ cm}^{-2}$. It is assumed that for every disappeared ester one fulgimide is bonded to the monolayer.

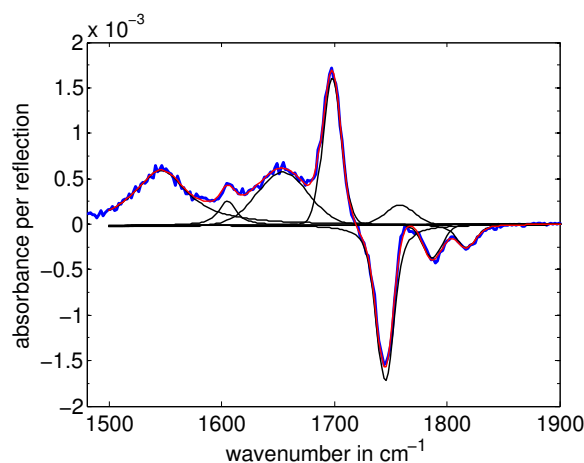


FIGURE 1.6: Infrared absorbance of a monolayer of C fulgimide in the carbonyl region using succinimidyl ester as reference. The number of disappeared ester is determined by fitting different infrared bands (black line), the sum of the individual peaks is displayed in red.

1.4 Diluted photochromic monolayers

In the work of [58] diluted fulgimide monolayers are prepared by controlling the density of anchoring sites on the silicon surface. In his PhD Thang showed grafting silicon using mixtures of decene/undecylenic acid leads to segregation into domains on the surface which is not suitable for the purpose of this study. He used mixed monolayers prepared from mixture of *w*-decene and *w*-ester because there was no evidence of domain formation. This required, however, to convert the ester group into COOH by hydrolysis, which reaction yield is not unity. Moreover the quality and purity of the ester monolayers were generally not as good as that of acid monolayers.

For these reasons a new approach is introduced here where the first monolayer is an acid monolayer as in figure 1.1. The dilution of the fulgimides on the surface is obtained by exposing the succinimidyl ester monolayer to a solution containing fulgimides and ethylamine. A random grafting is expected and the final fulgimide surface density is controlled by the relative concentration of the fulgimides and ethylamine, as schematically shown in figure 1.7. The relative surface concentration of fulgimides and ethylamine is piloted by the concentration of precursors in solution.

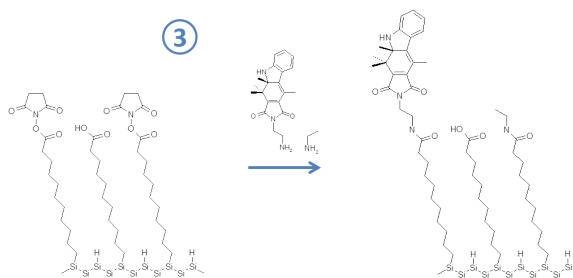


FIGURE 1.7: Preparation of dilute fulgimide monolayer

1.4.1 Amidation kinetics

For the preparation of dilute monolayers the amidation solution did not only consist of Fulgimide but of a mixture of fulgimide and ethylamine ($\text{CH}_3\text{-CH}_2\text{-NH}_2$). Ethylamine is used because it is a small amine that can be coupled to the surface and its ethyl group is not expected to strongly interact with the photochromes. By mixing the fulgimide and ethylamine both amidations happen simultaneously and a mixed monolayer are obtained. The order of magnitude of amidation mixtures to obtain desirable photochromer densities on the surface is not known.

The characteristic amidation time is estimated by time resolved monitoring the amidation of open fulgimide and ethylamine in acetonitrile. This is realized by mounting a succinimidyl ester monolayer in a cell where it is in contact with the amidation solutions (cell in appendix B.2). During the amidation the infrared absorbance spectrum of the sample is continuously measured. The results are shown in figure 1.8. The number of disappeared succinimidyl ester is shown against the amidation time. The concentrations of the fulgimide and ethylamine amidation solutions are 0.5 mM.

When ethylamine is in contact with the succinimidyl ester monolayer the amidation is much quicker compared to the coupling of fulgimide. The beginning of the amidation has not even been observable for ethylamine due to the time delay between the start of the infrared absorbance recording and the injection of the amidation solution. Furthermore, using ethylamine all succinimidyl ester could have been removed. Less succinimidyl ester are replaced by the bulky fulgimides than by the small ethylamine. The characteristic amidation times can roughly be estimated to be in the order

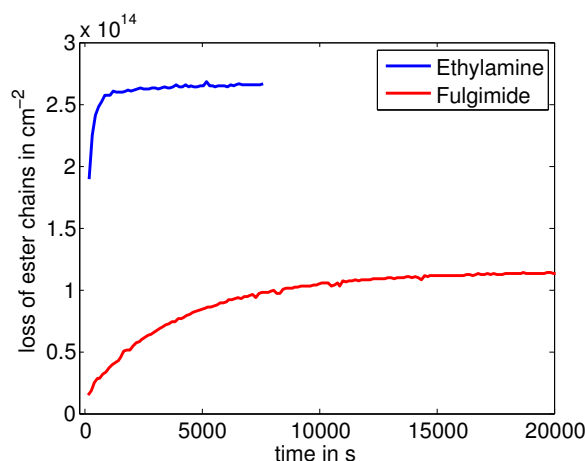


FIGURE 1.8: Disappeared succinimidyl ester determined by FTIR for diluted amidation solutions of open fulgimide and ethylamine against amidation time

of $\tau_{ful} = (4000 \pm 500) \text{ s}$ and $\tau_{ethyl} = (200 \pm 150) \text{ s}$. These characteristic times are too long to be explained by mass transport limitations of precursors towards the surface. The rate determining step of amidation must be the binding step which requires that the precursor adopt an adequate conformation on a 2D restricted environment. This is obviously easier for a short chain (ethylamine) than for the amino linker attached to bulky fulgimide compound.

1.4.2 Procedures

The experimental procedure for dilute fulgimide monolayer is a variation of the anchoring of amino terminated fulgimide (step 3) that is described above.

The COOSuc surfaces are immersed into acetonitrile containing 5mM of closed C or open E/Z amino terminated fulgimide and different amounts of ethylamine. Due to the quicker amidation with ethylamine with respect to the amino fulgimide an excess of fulgimide has been used. Different fulgimide-ethylamine ratios have been used: for the different samples the ethylamine concentration is smaller by a factor of 0.17, 0.26, 0.33, or 0.66 with respect to the fulgimide concentration. As for the dense fulgimide monolayer the Schlenk containing the fulgimide and ethylamine is out-gassed using argon, the reaction proceeds at least 2 hours and finally the

samples are cleaned in acetonitrile and dried using argon.

1.4.3 Quantitative surface composition

In figure 1.9 the different infrared absorbance spectra corresponding to different mixtures of C fulgimide and ethylamine are shown (the ratio of 0.26 has been done with E fulgimide and is therefore not listed). The different mixtures are obtained using a constant amount of fulgimide (5mM) and a variable amount of ethylamine. The left and right panel show the infrared absorbance using hydrogenated silicon and succinimidyl ester as reference, respectively. The intensity of infrared band associated to the asymmetric maleimide C=O stretching at 1698 cm^{-1} clearly differs for the different curves.

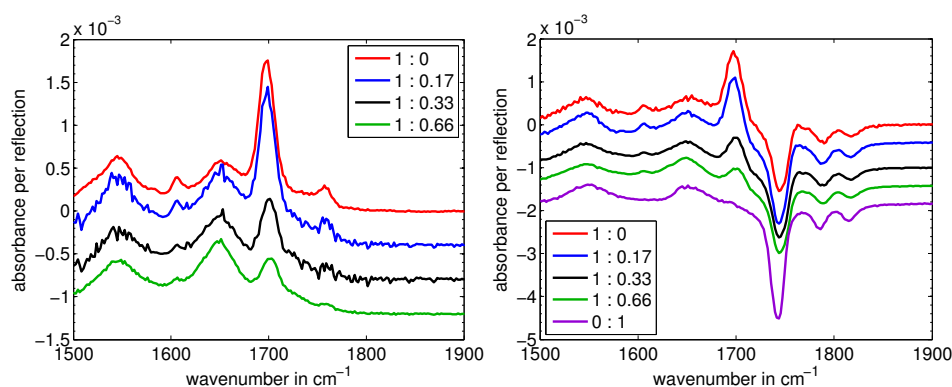


FIGURE 1.9: Infrared absorbance spectra after using different mixtures of fulgimide and ethylamine in p polarization using hydrogenated silicon (left) and succinimidyl ester (right) as reference.

The intensity of all infrared bands associated to the fulgimide differ strongly for different mixtures. The less ethylamine is in the amidation solution the more intense is the fulgimide peak at 1700 cm^{-1} . On the other hand the amide group at 1650 cm^{-1} and the number of disappeared succinimidyl ester groups are rather constant for all experiments. This indicates the successful preparation of dilute monolayer consisting of fulgimide and ethyl groups attached on the surface.

The photochromic density can not be determined from the disappeared succinimidyl ester because the latter are replaced by ethylamine, too. Their density has therefore been determined using the spectra in right panel of

figure 1.9. The dilute monolayer must be a linear composition of the dense fulgimide monolayer (red) and the ethylamine monolayer (purple). The density of the pure C monolayer is determined by the number of disappeared esters. Accordingly the number of fulgimides on dilute monolayers can be calculated by the linear decomposition of the dilute fulgimide monolayer by a dense fulgimide and ethylamine monolayer.

The determined densities of the fulgimide monolayers are shown in figure 1.10 as a function of the fulgimide/(fulgimide + ethylamine) concentration. We note that the data points are aligned on a straight line that does not pass through the origin. This is in perfect agreement with the fact that the amidation kinetics of ethylamine is much faster (figure 1.8).

The density of the fulgimide monolayer spans from 0.6 to $1.8 \cdot 10^{14} \text{ cm}^{-2}$ (factor 3). Further decreasing the fulgimide density would strongly affect the sensitivity of the measurement 1.9 and no precise study of the switching kinetics would be possible.

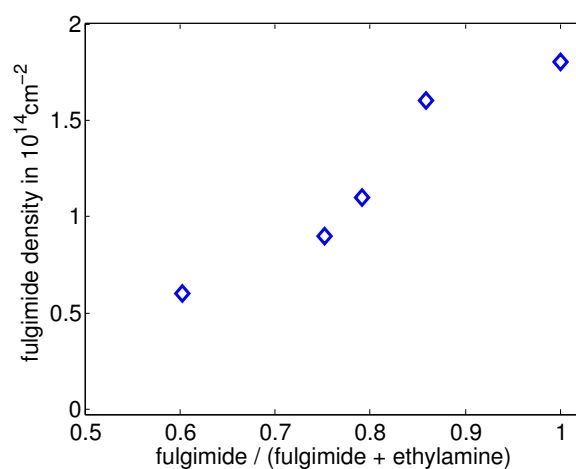


FIGURE 1.10: Different densities of dense and dilute fulgimide monolayer prepared by ethylamine and C fulgimide

1.4.4 Surface topography

In dilute monolayers the photochromes can form aggregates. Therefore every step of the sample preparation is controlled by atomic force microscopy (AFM).

A representative AFM image of topography of hydrogen terminated silicon after etching is shown in the left figure 1.11. The surface exhibits a staircase structure with flat terraces and atomic steps (0.31 nm high). The atomically flat terraces of around 100 nm width are visible all over the surface. The surface shows only small amounts of impurities. In the right panel a line profile is displayed for the black line (labeled 1) of the left figure showing the different terraces and their height difference. The height variation on the surface is not significant. The root mean square roughness is 0.17 nm.

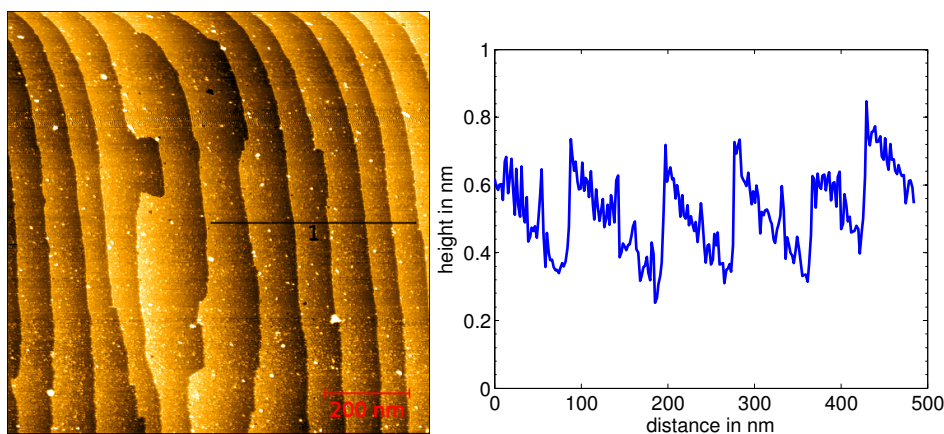


FIGURE 1.11: Topography AFM images of hydrogenated silicon (left) and a profile line (right).

The morphology of the carboxylic acid monolayer is shown in 1.12. The staircase structure of the silicon surface remains clearly visible, no significant change of the surface topography is detected. Therefore a good surface coverage is indicated that corresponds to the determined surface densities of carboxylic acid monolayers. However, due to the monolayer the edges are smoother. Only a very small amount of impurities is present. The roughness (RMS) is similar as for the hydrogen terminated surface 0.18 nm.

A representative AFM image of the topography of a dilute fulgimide monolayer ($0.9 \cdot 10^{14} \text{ cm}^{-2}$) is shown in figure 1.13. The image was captured

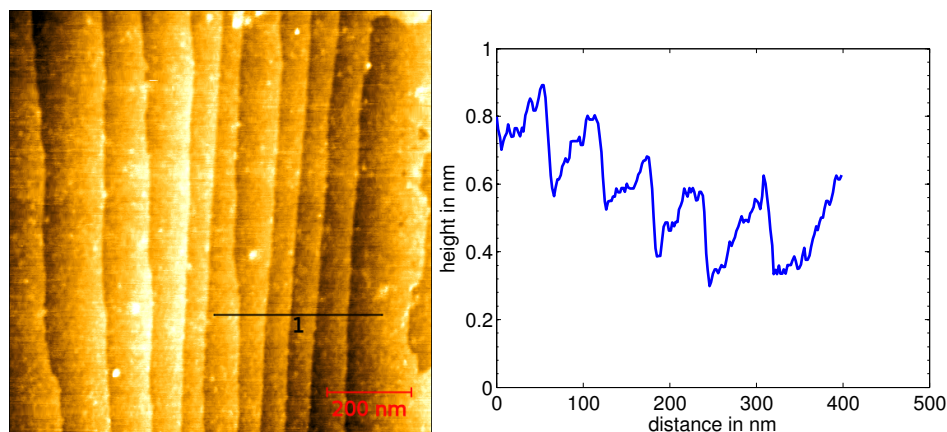


FIGURE 1.12: Topography carboxylic acid monolayer (left) and profile (right).

after several switching measurements. The silicon staircases of 0.31 nm are still observable through the organic monolayer. The surface looks homogeneous without residual of fulgimide or ethylamine aggregates. Local differences between the ethylamine and fulgimide are not observable due to the lack of resolution. The roughness (RMS) is about 0.20 nm.

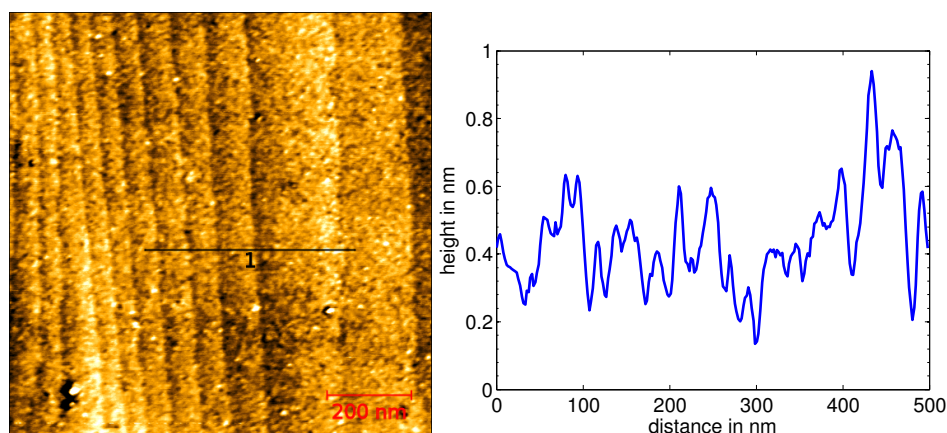


FIGURE 1.13: Topography AFM images of a dilute fulgimide monolayer (left) and corresponding profile (right).

1.5 Experimental setup and procedures

The photo commutation of fulgimide is measured on surfaces and in solution. For a good monitoring of the switching kinetics the photochromes are switched in situ inside the infrared or UV-visible photo-spectrometer for the experiments on surfaces or in solution, respectively. The illumination setup used in the group before [58] is improved by more powerful LEDs, an fully automated control of the light pulse intensity and duration and better control of the polarizers. The illumination setup is adapted to the experimental conditions.

1.5.1 Experimental setup for photo switching on surfaces

The illumination setup for the photo isomerization on silicon surfaces can be seen in figure 1.14. The surface can be illuminated by different LEDs with wavelengths of 365 nm (UV)³, 525 nm (green)⁴, or 590 nm (yellow)⁵. LED specific lenses are fixed directly on-top of every LED to reduce the divergence of the beam. The light is moreover paralleled using a plano convex lens so that an area of the size of the measured sample (15 mm x 3 mm) is illuminated homogeneously. Furthermore, a red laser⁶ of 655nm may be used to illuminate the surface. This laser is not fixed to the setup but separately mounted.

The LEDs can illuminate the surface in an angle of 45° or 90°.

1.5.2 Experimental setup for photo switching in solution

To monitor the photo-isomerization of photochromes in solution, 10 μ M or 20 μ M of solely C-Fulgimides are solved in 2ml of acetonitrile. They are stored in a closed cuvette of quartz glass with transparent sides. The cuvettes are placed inside the UV visible photo-spectrometer⁷. The solution can be illuminated with the same LEDs as on surfaces. The LEDs have

³Nichia Corporation NVSU233A

⁴Nichia Corporation NCSG119T

⁵Nichia Corporation NCSA119T

⁶Roithner LaserTechnik GmbH, RLDH660-40-3

⁷Agilent Technologies, Cary

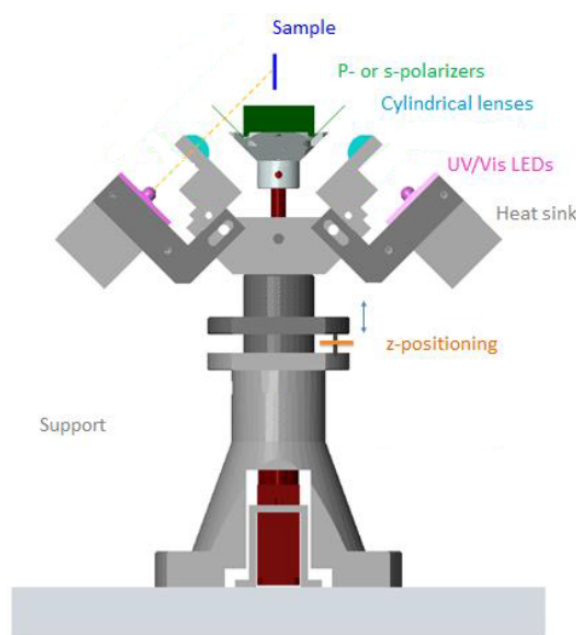


FIGURE 1.14: Experimental illumination setup for the in situ irradiation inside the FTIR spectroscope (changed schema, original schema from [58])

the same lenses mounted directly on-top of each LED but to ensure that the photon flux is homogeneous on a centimeter scale no additional lens is used.

1.5.3 Light flux calibration on surfaces and in solution

The experimental setup for the light flux calibration is depicted in figure 1.15. The forward current ΔI of a power supply is controlled by an analog voltage input ΔV that can be created by labview or the infrared spectroscopy software OPUS. The forward currents then aliment the two visible or UV LEDs. The photon flux of the different LEDs is calibrated using a silicon photo-diode⁸. The photosensitive area is a circle with a diameter of 1mm for the calibration of the 365 nm and 525 nm and 2mm for 590 nm and 655 nm. The photo current can be converted to a light flux using the responsivity of the photo diode of 0.05 A/W, 0.24 A/W, 0.35 A/W and 0.42 A/W for 365 nm, 525 nm, 590 nm and 660 nm, respectively. Systematical uncertainties of the photo diode and its responsivity used in the light flux calibration are in the same directions for all measurements and are therefore

⁸Hamamatsu S2387-R33

not listed.

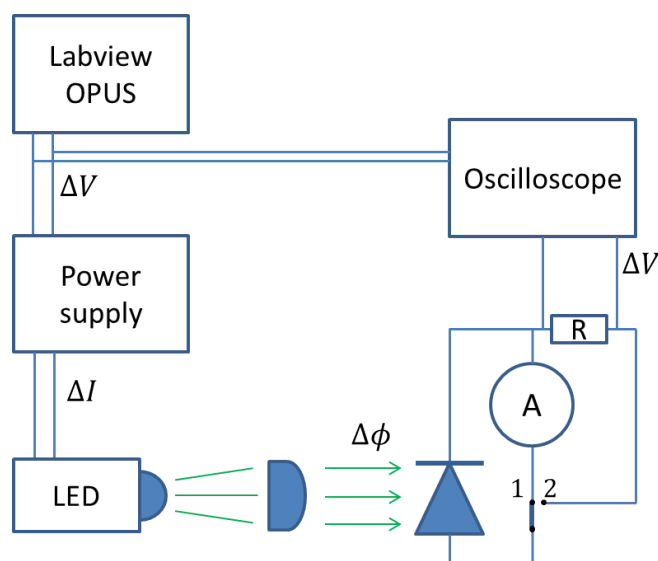


FIGURE 1.15: Setup for the calibration measurement of the beams

First the light fluxes are calibrated using continuous light. The photo current of the photo diode is measured using a multi-meter⁹ (switch position 1 in figure 1.15). The same geometry is used as in the experiment in solution and on surfaces, the photo-diode is in the sample position. The resulting light flux calibrations for the different wavelengths in solution and on surfaces are listed in 1.2 and 1.3, respectively.

The forward current of the 365 nm (525 nm) LED may be reduced to 92 mA (128 mA) and 31.7 mA (37 mA) to reduce the light flux by a factor of 0.32 and 0.1, respectively.

Linear polarizers for visible and UV light may be installed in the optical path. The polarizers are controlled by a motor and thereby can be removed or placed inside the beam path during the experiments. The UV and visible polarizers reduce the light flux by a factor of 0.25 and 0.40, respectively. If the sample is illuminated by p polarized light the incident angle is 45° , for s polarized light an incident angle of 90° is used.

The photon flux for the measurements in acetonitrile is corrected by the transmission of the quartz cuvette.

⁹Keithley

	Forward current	Cuvette transmission	Photo current	Photon flux Φ
365 nm	300 mA	92.9%	74 μA	$3.35 \cdot 10^{16} \text{ cm}^{-2}\text{s}^{-1}$
525 nm	700 mA	93.2%	1600 μA	$2.22 \cdot 10^{17} \text{ cm}^{-2}\text{s}^{-1}$
590 nm	700 mA	93.3%	230 μA	$9.32 \cdot 10^{16} \text{ cm}^{-2}\text{s}^{-1}$
655 nm	93 mA	93.3%	400 μA	$5.79 \cdot 10^{16} \text{ cm}^{-2}\text{s}^{-1}$

TABLE 1.2: Light flux calibration in solution

	Forward current	geometry factor	Photon current	Photon flux Φ
365 nm @ 45°	300 mA	$1/\sqrt{2}$	20 μA	$6.6 \cdot 10^{16} \text{ cm}^{-2}\text{s}^{-1}$
525 nm @ 45°	700 mA	$1/\sqrt{2}$	138 μA	$1.4 \cdot 10^{17} \text{ cm}^{-2}\text{s}^{-1}$
590 nm @ 45°	300 mA	$1/\sqrt{2}$	725 μA	$1.4 \cdot 10^{17} \text{ cm}^{-2}\text{s}^{-1}$
365 nm @ 90°	300 mA	-	20 μA	$9.4 \cdot 10^{16} \text{ cm}^{-2}\text{s}^{-1}$
525 nm @ 90°	700 mA	-	138 μA	$1.9 \cdot 10^{17} \text{ cm}^{-2}\text{s}^{-1}$
655 nm @ 90°	93 mA	-	400 μA	$7.1 \cdot 10^{16} \text{ cm}^{-2}\text{s}^{-1}$

TABLE 1.3: Light flux calibration on surfaces

1.5.4 Influence of the light pulse duration

For a meaningful monitoring of the photo switching on surfaces it is desirable to measure precisely the photo isomerization at the very beginning of the commutation and at the saturation. Consequently the sample has to be measured after very short and very long illumination times that differ by orders of magnitude. Therefore light pulses of different illumination durations are used to illuminate the surface. The duration of the light pulses increases during the commutation. After every light pulse the infrared or UV visible absorbance is measured. This process is repeated until the absorbance spectrum shows no further change due to the illumination. The influence of the different light pulses is discussed in the following section to examine the expected linearity of the illumination time and the number of irradiated photons.

The LEDs are piloted via a power supply using an analog voltage. The relation between the output voltage and the light flux is examined. Therefore an ohmic resistance has been coupled to photo current and the voltage

at the resistance has been measured by an oscilloscope (switch position 2 in 1.15). Thereby the voltage is proportional to the photon flux.

In figure 1.16 an input voltage is turned on for 36.8 ms and the response of the LEDs is measured by the voltage drop at the ohmic resistance. The oscilloscope is triggered by the LED input voltage. Four different regions for the light flux during an LED pulse can be identified. After the voltage is turned on at $t=0$ the light flux is slightly retarded by about 4.0 ms for the green and about 6.5ms for the UV light. This is due to the fact that some capacities are charged. The light flux reaches its maximal value within a few ms (region 1). Heating of the active layer of the LED subsequently reduces the efficiency for the green and UV LED. This thermal stabilization of the LED has been characterized more precisely using longer voltage pulses, but the saturation is already visible at 40 ms (region 2 and 3). The continuous light flux of the LED is calibrated after thermal stabilization, thus the saturation corresponds to the light flux mentioned in table 1.2 and 1.3. After the voltage input is turned off again the light intensity slowly drops because the capacities charged at the beginning are slowly dis-charged (region 4). This roughly corrects the retarded turning-on of the LED.

The infrared photo-spectroscopy software creates a systematical error by increasing the duration of all voltage pulses by about 16.8 ms.

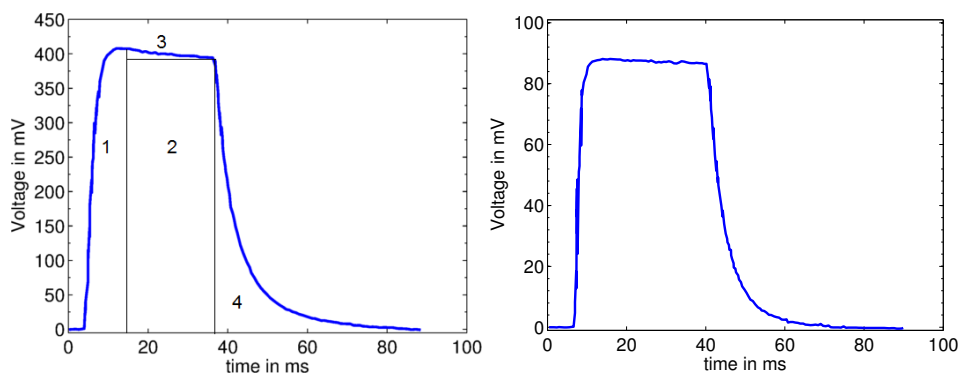


FIGURE 1.16: Temporal development of the intensity for green (left) and UV (right) light pulses

Finally the number of photons is calculated individually for every light pulse by addition of the number of photons in the different regions. Region 1 is numerically integrated, region 2 is linear to the voltage input duration

and responsible for most of the photons even for short pulse durations. The decrease due to heating the active layer (region 3) and the sweep after turning of the voltage (region 4) can be very well described by exponential functions and then be integrated.

The first light pulse of every experiment has been $T_{pulse} = 100$ ms and thereby there is a significant correction due to the systematical increase of the light pulse duration by 16.8 ms for experiments on surfaces. The minor corrections due to on and off turning of the LEDs and heating of the active layer are taken into account.

Chapter 2

Photo-Switching Properties of Fulgimides in Solution

2.1 Introduction

The indolyl-fulgimide exhibits three different forms that can be seen in figure 2.1: the closed C form and the two colorless open E and Z form. The closed C form absorbs visible and UV light whereas the open E and Z isomers only absorb UV light. The trans-cis isomerization between the E and Z form is triggered by the absorption of UV light. Under UV illumination the hexatriene backbone of the E isomer can be closed and C isomer is obtained. The back isomerization is obtained by the inverse ring opening reaction under visible light. The closed form has a large delocalized π -electron system whereas for the open form the π -electron system is not delocalized about the whole molecule which results in different properties [57]. The three different isomers are thermally stable and therefore suitable to study the photo commutation [67, 68].

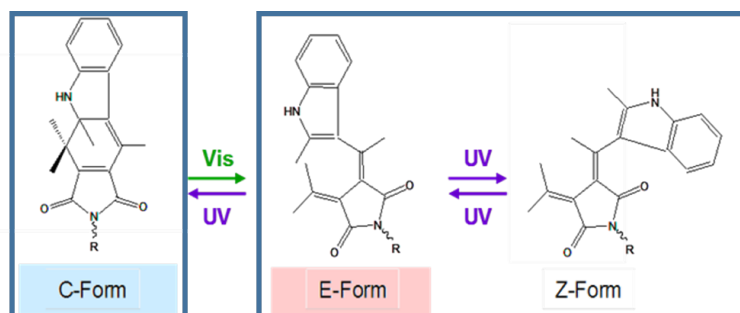


FIGURE 2.1: Photochromism of indolyl-fulgimide under UV and visible irradiation

The photo isomerization of fulgimide in solution has been extensively studied [44, 47, 69–72]. Fulgimide show a fatigue effect due to thermal or photo chemical degradation [17, 18]. Synthesis of different fulgides, notably with different side groups, have been done to improve the fatigue resistance [68, 70]. Thereby photo-chemical extremely stable fulgide have been obtained that undergo 10000 photo-chemical cycles before degrading 13% [19].

The isomerization mechanism of the ring opening and closing reactions of fulgimide and fulgide have been studied on the molecular scale by the Zinth group [45–49, 73–79] using ultrafast reaction dynamics. The photo induced ring opening isomerization appears to be thermally activated and has reaction times of about 2 to 15 ps. The reaction time and quantum efficiency strongly depend on the polarity of the solvent [73]. This indicates that the optical excitation the C isomer after a Franck Condon state is reached and the isomer relaxes to at least one meta-stable excited state [78]. The energy barriers of the meta-stable excited state depend on the environment and can be thermally overcome. The quantum efficiencies are between 0.5% to 11% and depend on the relative height of the energy barriers [46]. Other models assume two meta stable excited states [74, 79, 80]. Schematic reaction schemes for the ring opening reaction based on one or two meta-stable excited states are shown in figure 2.2.

In the left figure 2.2, the reaction scheme of Draxler et al. (2009) is shown where the C isomer is excited by a visible photon and reaches a Franck Condon state [46]. After 200 fs the isomer relaxes to a meta-stable excited state with a lifetime of 9 ps [46]. Two reaction channels are available, the interval conversion (IR) back to the closed isomer and the photo-chemical reaction (PC) to the open isomer. The right panel of figure 2.2 shows the reaction scheme developed by Nenov et al. (2012) in the same group [74]. Again the isomer is excited to the Franck Condon state and relaxes to a meta-stable local minimum Min_C . Again two radiationless reaction channels are available: back to the closed form or to the so called $\text{CoIn}_{C/cZc}$ state. From the $\text{CoIn}_{C/cZc}$ rapid decays to to the open and closed states are possible.

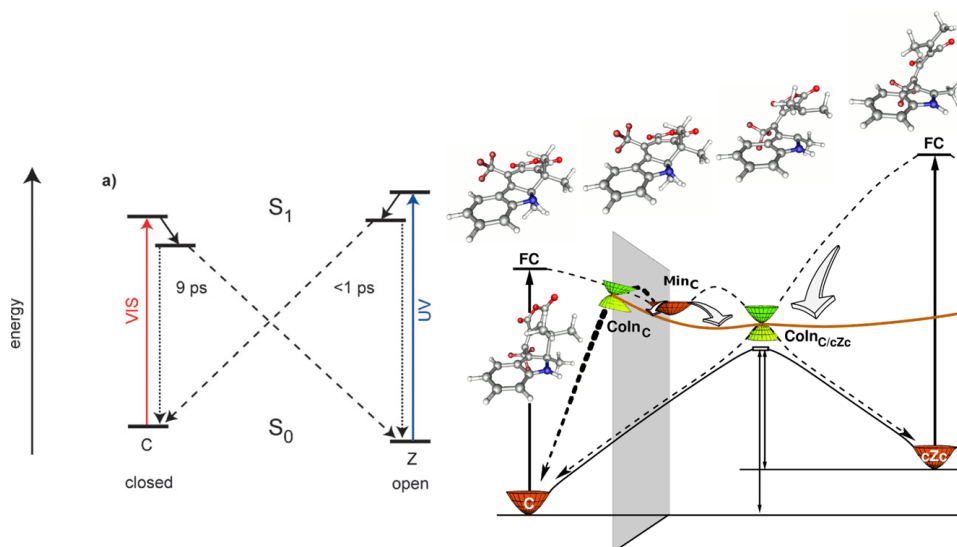


FIGURE 2.2: Franck–Condon diagram representing the reaction schemes for the ring opening reaction. The left model based on one meta-stable excited state is proposed by Draxler et al. [46], the right model including the corresponding molecular structures by Nenov et al. [74].

The ring closing reaction ($E \rightarrow C$) is induced by the absorption of a UV photon by the open E isomer. Thereby the electronic system of the E isomer is excited. From the excited state the molecule can directly relax to the closed state or remain in the open E form. After excitation the photo-processes happens on ultra-fast timescales 0.3 ps to 0.5 ps [81]. The $E \rightarrow C$ isomerization shows no temperature dependence and is therefore considered to be thermally barrierless [73]. The quantum efficiency is of around 5% to 20% [49, 73, 81]. The solvent interactions and excitation wavelength only have minor influence on the quantum efficiency or timescales [73, 81].

The photo-switching kinetics of fulgimides in solution reveals first order kinetics for the ring opening reaction, whereas the ring closing reaction kinetic was described by either mono or bi exponential functions [58, 82]. An influence of the solvent polarity and viscosity is expected [83–85].

The kinetics of photocommutation of fulgimides in solution has already been investigated by Thang in his PhD [58].

The main purpose of this chapter is to briefly characterize again the process by UV visible photo-spectroscopy. Our aim is measuring precisely the characteristic parameters (effective cross section and PSS) which will serve

as benchmark to discuss kinetic parameters which will be measured with fulgimide monolayers. Importantly, the same calibrated conditions of illumination and photon doses will be used in the two situations.

2.2 Results

2.2.1 First commutations of as received C fulgimide

Open (E/Z mixture) or closed (C) fulgimide were used as received and dissolved in acetonitrile for UV-Vis spectroscopic characterizations. The left panel in figure 2.3 shows the UV-Vis spectrum of C isomer solution (red line) before any light illumination. This spectrum shows a marked difference with respect to literature [56]. The high absorption in the range 350 nm-450 nm was in fact not observed in [56] but in [58] with the same compound used in the present work. Exposing this C-solution to Vis-light (530 nm) for sufficiently long time to promote complete $C \rightarrow E/Z$ ring opening reaction yields the blue line spectrum in the right panel of figure 2.3. Comparison of this spectrum with that of as received E/Z isomer (red line 2.4) reveals a shoulder at 400 nm-450 nm and the difference of the two spectra (black line) gives a wide optical absorption band centered around 400 nm. Subtracting numerically this band to the spectrum of C-solution yields the blue spectrum in the left panel of 2.3. This *corrected* UV-Vis spectrum is now consistent with past reports [56].

These characterizations highlight that the as received C-isomer presents unwanted species responsible for the supplementary band around 400 nm that is not observed for the as received E/Z isomer. Moreover, figure 2.3 evidences that these species are still present after irradiation with 530 nm light. UV-illumination of the E/Z solution corresponding to the blue spectrum in figure 2.3 (right panel) leads to C/E/Z mixture whose spectrum (red line) is shown in figure 2.4. This spectrum may be well accounted by linear combination of *corrected* C and as received E/Z spectra (gray line). In addition this spectrum is also very similar to that measured after several UV-Vis irradiation cycles (black line). We therefore conclude that the 400 nm band has disappeared after the first UV-irradiation.

In light of UV-Vis characterizations, it is impossible to identify the unwanted chemical species present in the initial C-solution. RMN analysis did not give further insights. No sizable change of the NMR spectra was

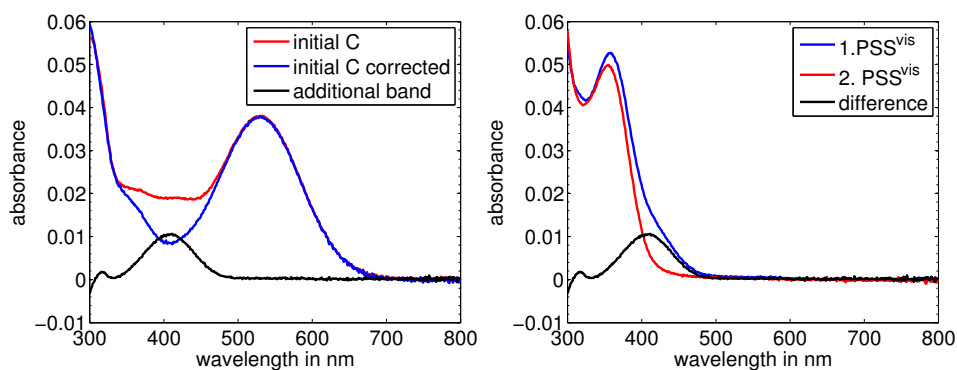


FIGURE 2.3: UV-Vis spectra of different fulgimide solutions (concentration) dissolved in acetonitrile. Left panel: Solution prepared with as received C-isomer (red), after correction (blue) from absorption related to unwanted species (black in 2.4). Right panel: solution prepared with as received E/Z isomer (red) and after Vis irradiation of as received C-isomer solution (blue). The black line shows a broad absorption band at 400 nm assigned to unwanted species in initial C-solution (see text).

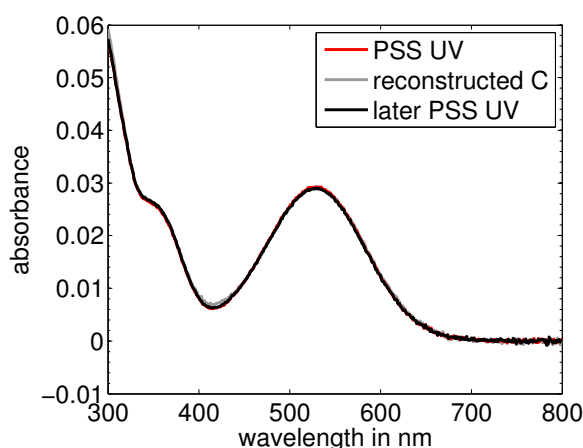


FIGURE 2.4: Red: Spectrum obtained after UV-irradiation of E/Z solution corresponding to blue spectrum in (b). Black : PSS spectrum obtained after nth UV-Vis cycles. Grey: linear combination of corrected C-spectrum (blue in left panel of 2.3) and E/Z spectra (red in right panel of 2.3).

observed after UV illumination of C isomer solution although the UV-Vis indicates clearly changes with the disappearance of the 400 nm band (NMR data from Long PhD[58]).

We suspect that these unknown stem from the very last step of synthetic route to obtain C-isomers. In fact, as described in [56], the C-isomers are obtained by dissolving purified E/Z isomer in benzene and illuminating the solution with UV light. The resulting mixture C/E/Z in benzene is then

treated by flash chromatography to separate isomers. To explain the disappearance the 400 nm after UV irradiation we hypothesize that the related species were interacting by π -stacking with the polar C isomers. Upon Vis irradiation the 'duplex complex' (C + unknown species) remains stable but it makes sense that UV illumination may split the complex. In this scenario the unknown species would be dispersed in solution and they are not associated with any sizable UV-Vis absorption band which speaks for small molecules (e.g. solvent molecules from last separation step to obtain C-isomers).

In the context of the present work, several arguments suggest that the above mentioned unwanted impurities have no significant impact on photo commutation processes in solution and at surfaces.

1. Red and black spectra in figure 2.3 overlap very well.
2. The characteristic parameters of photo-isomerization in solution of Long [58] are identical for the first (C isomers + unwanted species are present) and subsequent cycles.
3. Long found the same at surfaces. We also reproduce this in chapter 3 with a better precision. Moreover, additional IR characterizations about photo-isomerization at surfaces (Chapter 3) (see annex B.1 of chapter 3) if present on the surface do not influence the switching behavior

For the determination of the cross sections all solutions are switched between the PSS^{UV} and PSS^{vis} after the 400 nm band disappeared. It has been shown that the presence of the additional absorbance band at 400 nm does not influence the isomerization kinetic [58].

2.2.2 Isomeric composition at the photo stationary states

The UV visible absorbance at the PSS^{vis} after several irradiation cycles is compared to the absorbance of a as prepared E/Z fulgimide solution (see left panel of figure 2.5). This spectrum indicates that the PSS^{vis} consists of

100% open E/Z fulgimide. However, by UV visible spectroscopy we cannot distinguish between the two open E and Z isomers.

The UV-Vis spectrum at the PSS^{UV} is compared in the right panel of figure 2.5 to the corrected spectrum of the initial C solution. In the PSS^{UV} the visible absorbance peak does not reach the same height as initially the corrected C solution. In fact the visible peak at 530 nm is smaller by a factor of 0.77. For the comparison only wavelengths greater than the additional absorbance band are considered (greater than 500 nm). Due to the Beer-Lambert law (linear relation between absorbance and concentration) one can conclude that only 77% of the open fulgimide switched back and therefore the PSS^{UV} consists of 77% C and 23% E/Z fulgimide.

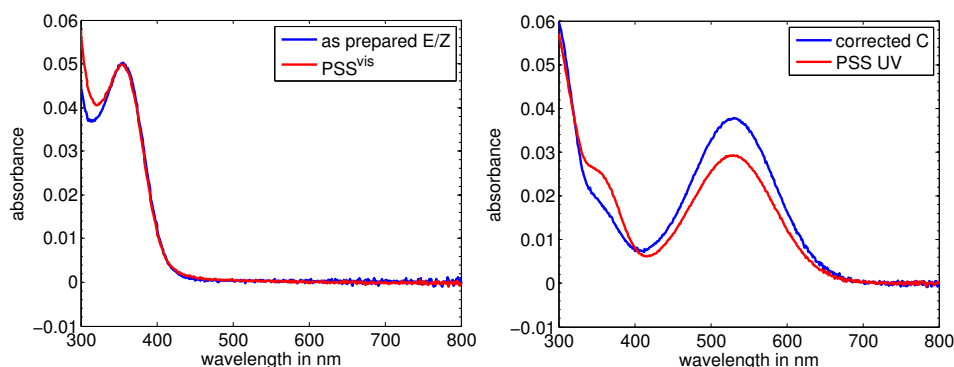


FIGURE 2.5: Left panel: UV-vis absorbance for the visible PSS (red) and a as prepared E/Z solution (blue) show both no visible absorption. Right panel: comparison between the corrected C spectrum (blue, from left panel of 2.3) and the UV PSS (red) show a mixed isomeric composition for the UV-PSS

	E/Z form	C form
PSS^{vis}	100%	0%
PSS^{UV}	23%	77%

TABLE 2.1: Isomeric composition at the visible and UV photo stationary states in acetonitrile

The visible and UV PSSs are the same independent whether the initial solution consists of as received C or E/Z fulgimide. One can switch the solution several times from one PSS to the other without any change of the

isomeric composition at the PSS. The same or very similar photo stationary states have been reported in the literature before [49, 58, 69].

2.2.3 Photo degradation

In the following the possible photo chemical degradation resistivity is examined. The fulgimide are illuminated by UV light for long times and then the solution has been switched to the PSS^{vis} and back to the PSS^{UV}. The evolution of the visible absorbance band can be seen in the left panel of figure 2.6. Increasing UV exposure is represented by redder curves. The visible peak at the PSS^{UV} and of the UV peak at 365 nm at the PSS^{vis} decreases due to the UV irradiation. This indicates the loss of C and E/Z fulgimide whose photochromism is photo-chemically destroyed.

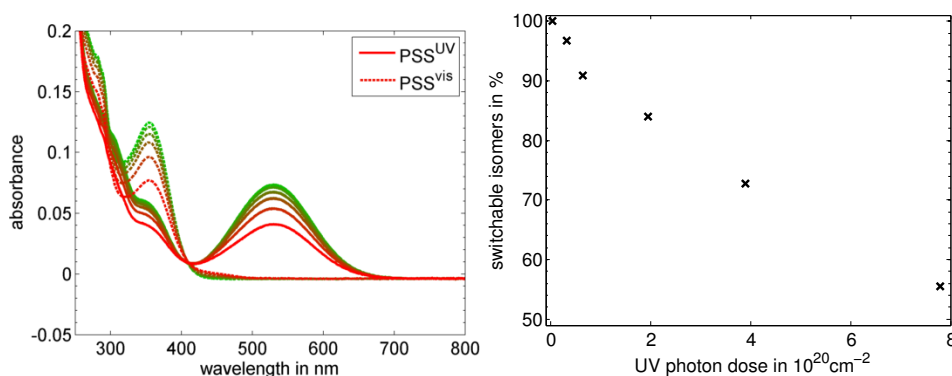


FIGURE 2.6: The left panel shows PSS^{UV} (solid lines) and PSS^{vis} (dashed lines) for increasing long time UV irradiation. The redder the curve the higher the UV exposure. The right figure shows the corresponding decrease of the number of switchable isomers against the number of UV photons that irradiated the solution.

The evolution of the visible absorption and thus the number of switched isomers is examined with respect to the UV photon dose (2.6 right). The number of switchable isomers decreases by around 50% after being exposed to a UV-photon dose of $8 \cdot 10^{20}$ per cm^2 . To reach the PSS^{UV} a much smaller photon dose of $2.4 \cdot 10^{18} \text{ cm}^{-2}$ is necessary. Assuming a linear decrease of the number of switchable isomers, for the photon dose to reach the PSS^{UV} ($2.4 \cdot 10^{18} \text{ cm}^{-2}$) the number of switchable isomers is expected to decrease by only 0.35% per cycle which is negligible.

2.2.4 Photoswitching kinetics

In figure 2.7 the absorbance curves corresponding to one ring opening commutation are shown. Initially the photochromes are in the PSS^{UV} (blue), after every visible light pulse they undergo intermediate states (gray or black) until the PSS^{vis} (red) is reached. The visible peak disappears due to the visible illumination that induces $C \rightarrow E$ isomerization. Each intermediate absorbance spectra between the two PSS is a linear combination of the two absorbance spectra at the PSS states. Therefore every intermediate absorbance spectrum $abs(t, \lambda)$ can be written in term of the absorbance spectra at the PSS states:

$$abs(t, \lambda) = \alpha(t) \cdot abs_{PSS^{vis}}(\lambda) + (1 - \alpha(t)) \cdot abs_{PSS^{UV}}(\lambda) \quad (2.1)$$

Now all kinetic information is included in the parameter $\alpha(t)$ that represents the relative advancement of the isomerization. Exemplary this kinetic parameter $\alpha(t)$ is shown for the $C \rightarrow E$ commutation excited by light of 525 nm and a subsequent $C \rightarrow E$ commutation by UV light. Since the isomeric composition at the photo stationary states are known the number of switched E/Z isomers can be calculated from $\alpha(t)$.

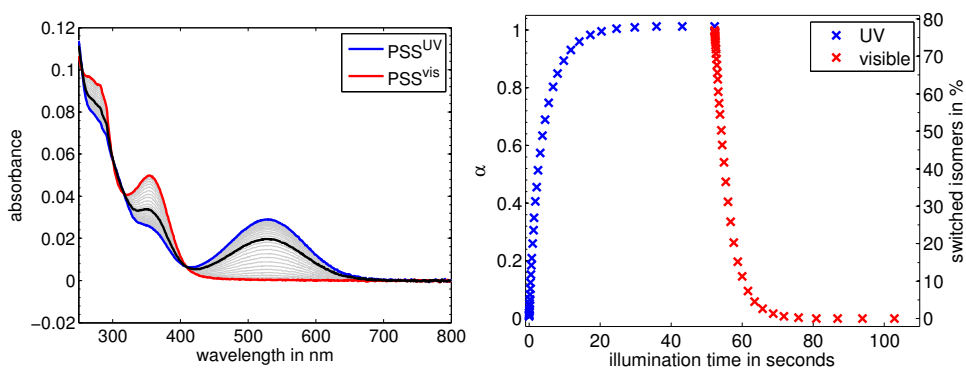


FIGURE 2.7: Left: evolution of the UV visible absorbance spectrum starting from the PSS^{UV} (blue) to the PSS^{vis} due to visible irradiation. Intermediate curves (black) are linear combinations of the PSSs. Thereby the kinetic parameter $\alpha(t)$ and the number of switched photochromes is determined (right).

Fulgimide in solution ($20 \mu\text{M}$ in acetonitrile) have been irradiated by

green illumination ($\lambda = 525 \text{ nm}$) from the PSS^{UV} to the PSS^{vis} using different light fluxes. The corresponding kinetic curves are shown in the left panel of figure 2.8 using a logarithmic time axis. The kinetic curve of the of the highest, middle and lowest light flux is displayed in black, red and blue, respectively. If the light flux is lower a longer illumination time is needed to switch the same amount of isomers as for a higher photon flux. The kinetic curve with the lowest light flux (blue) is therefore shifted by one order of magnitude with respect to the highest light flux (black curve). In the right panel the kinetic curves of the same experiments are shown against the photon dose instead of the illumination time. Now the three different curves perfectly overlap each other.

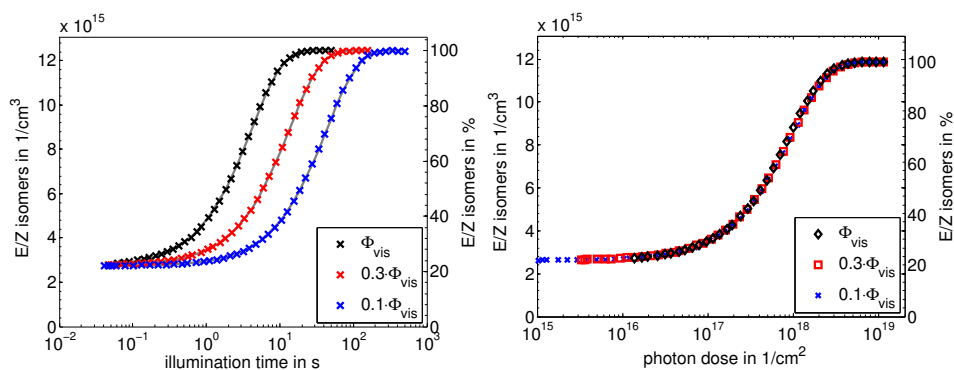


FIGURE 2.8: Left: Different kinetic curves of the ring opening reaction. The absolute and relative number of open isomers is shown against the illumination time for different photon fluxes. The right figure shows the same curves but against the number of irradiated photons per unit area instead of the illumination time.

The corresponding result for the ring closing reaction excited by UV light are shown in figure 2.9. The fulgimide are switched from the PSS^{vis} to the PSS^{UV} using different UV light fluxes. The right panel shows the number of E/Z isomers vs. the photon dose. A similar behavior for both isomerization directions is obtained. The photon dose to reach saturation is however very different, the ring closing reaction is more efficient.

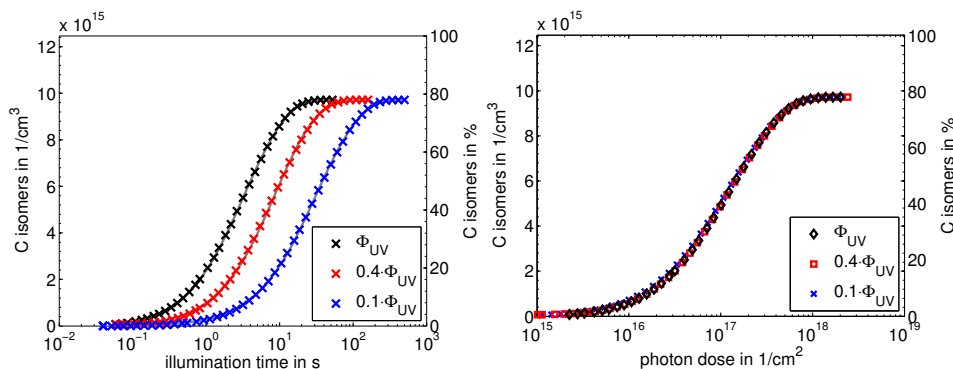


FIGURE 2.9: Left: Kinetic curves of the ring closing reaction under UV light for different photon fluxes. The number of C isomers is displayed as a function of the illumination time. Right: same kinetic curves as a function of the photon dose.

2.2.5 Isomerization cross section

In analogy to the absorption cross section the isomerization cross section is defined. The absorption cross section σ_{abs} is defined as the number of absorbed photons dn within a small path dx with respect to the total number of photons n and concentration c_{abs} :

$$\sigma_{abs} = -\frac{dn}{dx} \frac{1}{c_{abs}n} \quad (2.2)$$

Thereby σ_{abs} is measured in cm^2 and represents the covered area due a single molecule for a photon flux.

In the same spirit an isomerization cross section is defined by the relative number of *switched* isomers dC per unit time dt divided by C and the photon flux ϕ :

$$\sigma_{iso} = -\frac{dC}{dt} \frac{1}{C\phi} \quad (2.3)$$

Similar to σ_{abs} the isomerization cross section σ_{iso} is measured in cm^2 . Like for the absorption cross section this definition enables the determination of an intrinsic molecular parameter by an experiment using many photochromes. In the following the index 'iso' of the isomerization cross section σ_{iso} is skipped.

Using the photon dose $n = \phi t$ the experimental irradiation flux ϕ and time can be replaced. The instantaneous cross section σ can directly be

calculated numerically from the definition of the cross section in equation 2.3 by

$$\sigma_{num}(n) = \frac{C(n + \Delta n) - C(n)}{\Delta n} \frac{1}{C} \quad (2.4)$$

using the numerical derivative of the data.

The definition of σ is a differential equation that is solved by a single exponential function of the form

$$C = C_{PSS} \exp(-\sigma n) \quad (2.5)$$

Using a constant number of fulgimide $C + E/Z = 1$, equation 2.5 is equivalent to $E/Z(n) = (1 - C_{PSS} \exp(-\sigma n))$. Knowing the PSS we can rewrite the expression to:

$$E(n) = E_{PSS} \cdot (1 - \exp(-\sigma n)) \quad (2.6)$$

$$\Leftrightarrow \ln(1 - E(n)/E_{PSS}) = -\sigma n \quad (2.7)$$

The numerical cross section for the ring opening reaction with green light of 525 nm is shown for different light fluxes in the left panel of figure 2.10. The cross section is constant during the commutation at around $1 \cdot 10^{-18} \text{ cm}^{-2}$ for all different light fluxes.

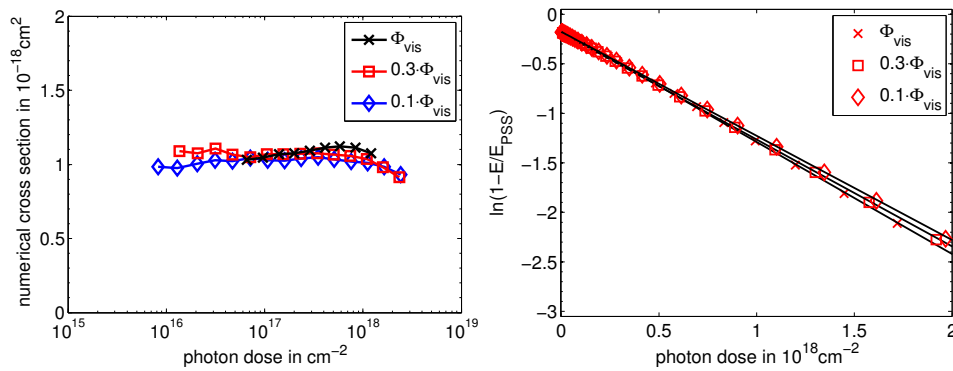


FIGURE 2.10: Left: Numerical cross section of the ring opening reaction of fulgimide under irradiation of different light fluxes of 525 nm. Right: first order kinetics of the ring opening reaction of fulgimide in under green light of 525 nm in acetonitrile and linear regression (black) to determine $\sigma_{C \rightarrow E}$

The right panel of the figure 2.10 shows the data of figure 2.8 plotted

as $\ln(1 - E(n)/E_{PSS})$ vs. the photon dose (525 nm) for the three different photon fluxes. The cross section σ is given by the negative slope that is determined by linear regression. The obtained cross sections for the highest, middle and lowest photon fluxes are $\sigma_{C \rightarrow E} = 1.11 \cdot 10^{-18} \text{ cm}^{-2}$, $1.08 \cdot 10^{-18} \text{ cm}^{-2}$ and $1.05 \cdot 10^{-18} \text{ cm}^{-2}$, respectively. The cross sections determined by the linear regression are in good agreement with the numerical cross sections.

The numerical cross section of the ring closing reaction is shown in figure 2.11 for different UV fluxes. The cross section is first constant but then decreases for all photon fluxes at around $5 \cdot 10^{16} \text{ cm}^{-2}$.

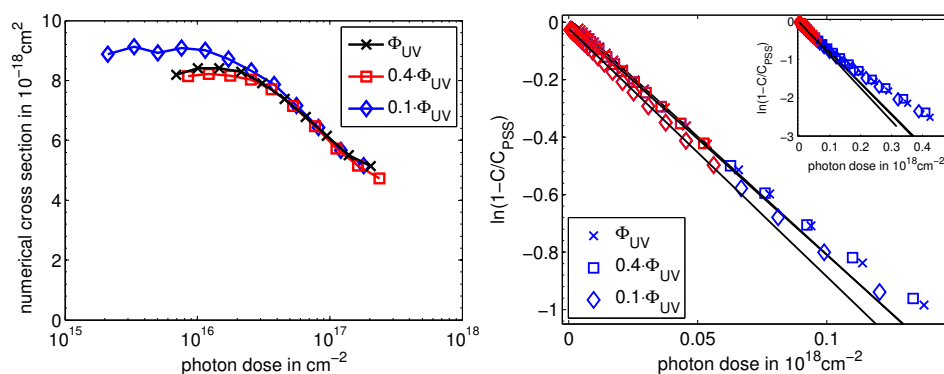


FIGURE 2.11: Left: Numerical cross section of the ring closing reaction for different light fluxes. Right: Determination of the cross section using a linear regression that is calculated by the red crosses at the beginning of the isomerization. Inset: whole isomerization with increasing gap between linear fit and experiment.

The right panel shows again the kinetic curve as $\ln(1 - C(n)/C_{PSS})$ against the photon dose n as before under visible light. The figure is zoomed at the beginning of the commutation, the inset shows the whole commutation. In the whole commutation the data points are not aligned on a straight line. Therefore the linear regression to determine the cross section is only valid for the first 60% of the isomers where the numerical cross section is constant ($< 4 \cdot 10^{16} \text{ cm}^{-2}$). Above this dose, σ is continuously decaying. This behavior was approximated by a bi exponential function [58].

Thereby the isomerization cross section σ can be determined for the experiments shown in 2.8 and 2.9. The cross sections for the ring opening and

closing reaction are shown for different photon fluxes in figure 2.12. The first two isomerization cycles have been done with the highest photon flux, isomerization cycles 3 and 4 with a photon flux reduced by a factor of 0.3 and the cycle 5 and 6 with a photon flux reduced by one order of magnitude. The switches with different photon fluxes result in the same cross sections with high reproducibility.

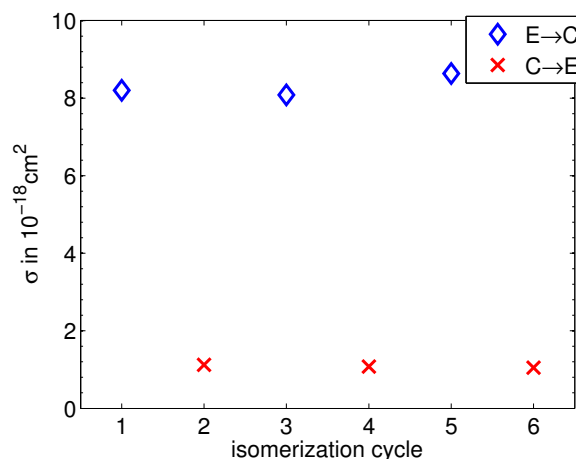


FIGURE 2.12: Cross sections of the different isomerization cycles including different photon fluxes for the ring closing (blue diamonds) under UV light and ring opening reaction (red crosses) under green light.

For the purpose the studies presented in chapter 5 the ring opening cross sections has been determined for the red laser of 655 nm and the yellow LED of 590 nm. The corresponding kinetic curves are shown in figure 2.13. The cross section for the ring opening reaction using 590 nm is $\sigma_{C \rightarrow E, 590nm} = (0.24 \pm 0.02) \cdot 10^{-18} \text{ cm}^2$.

For the red laser of 655 nm (blue diamonds) the slope and hence σ are much smaller than for the 590 nm (red crosses). In fact the red laser is only badly absorbed by the fulgimide because its wavelength is at the limit of the visible absorbance of the closed Fulgimide. The corresponding cross section is $\sigma_{C \rightarrow E, 655nm} = (0.12 \pm 0.01) \cdot 10^{-18} \text{ cm}^2$.

The determined cross sections for the different commutations in solution for the different excitation wavelength are listed in table 2.2.

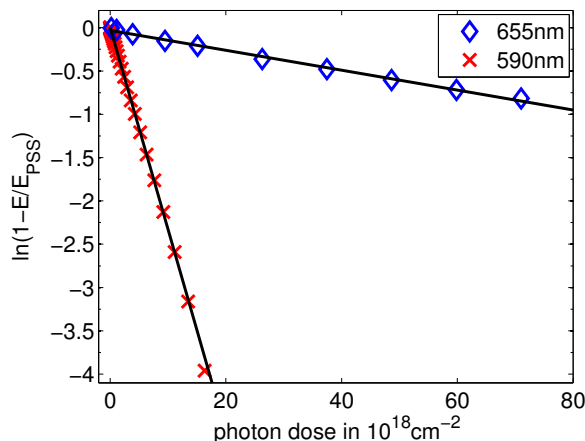


FIGURE 2.13: Kinetic curves of the ring opening reaction excited by the red laser of 655 nm (blue diamonds) and the 590 nm-LED and linear regressions.

2.2.6 Quantum efficiency

The absorbance abs depends on the molar extinction coefficient ϵ , the concentration c_{abs} and the pathlength l by

$$abs = \epsilon c_{abs} l \quad (2.8)$$

The absorbance cross section σ_{abs} is proportional to the molar attenuation coefficient by

$$\sigma_{abs} = \frac{10^3 \ln(10)}{N_A} \cdot \epsilon \quad (2.9)$$

with the Avogadro constant N_A .

The quantum efficiency η is defined as the probability that the absorbed photon leads to an isomerization and thereby represents the ratio of the absorbance and isomerization cross sections:

$$\eta = \frac{\sigma_{iso}}{\sigma_{abs}} \quad (2.10)$$

The different absorption and isomerization cross sections and resulting quantum efficiencies are listed in table 2.2. The error on $\sigma_{C \rightarrow E, 525nm}$ and $\sigma_{E \rightarrow C, 365nm}$ of around 4% that has been determined by the isomerization cycles with different photon fluxes can be considered as representative for the isomerization cross section in solution.

	365 nm	525 nm	590 nm	655 nm
$\sigma_{C \rightarrow E}$ in 10^{-18} cm^2	-	1.08 ± 0.04	0.24 ± 0.02	0.12 ± 0.01
$\sigma_{E \rightarrow C}$ in 10^{-18} cm^2	8.31 ± 0.29	-	-	
ϵ in $10^3 \text{ cm}^2/\text{mol}$	8.0	4.3	2.5	0.4
σ_{abs} in 10^{-18} cm^2	30.3	16.4	9.4	1.5
η	0.27	0.066	0.026	0.008

TABLE 2.2: Extinction coefficient ϵ , Isomerization and absorbance cross sections along with resulting quantum efficiencies η for the ring closing and opening isomerization with different wavelengths

The isomerization cross section of the ring opening reaction decreases for higher wavelengths due to the decreasing absorption (σ_{abs}). Anyway the quantum efficiency decreases with increasing wavelengths. Similar quantum efficiencies between 0.1% to 10% for the ring opening reaction of fulgimides have been reported for polar solvents dependent on the excitation wavelength [45, 46, 49, 73, 76].

The ring opening isomerization has at least one intermediate state and thereby its quantum efficiency is thermally activated [46, 77]. The relation between the quantum efficiency and the excitation wavelength has been examined by Brust et al. [76]. The photons of the 525 nm-LED are energetically higher than the photons of the laser at 655 nm. If now both photons excite the same reaction the energetically higher photon possesses an optical excess energy that is not consumed by the initial excitation. A part of this optical excess energy is transformed to heating the photochrome and thereby the reaction is effectively done at a higher temperature. Therefore for thermally activated photo-isomerizations the cross section increases with increasing optical excess energy, hence decreasing wavelengths.

The decreasing cross sections for increasing wavelengths will not be further discussed and only serve as a reference in chapter 5.

2.3 Discussion

According to the accepted paths for fulgimides (scheme 2.1) the following differential equation is derived under the illumination of visible light:

$$\frac{dC}{dn} = -k_{vis}C \quad (2.11)$$

The differential equation due to green light therefore reveals first order kinetics

$$C(t) = C_{PSS} \exp(-k_{vis}n) \quad (2.12)$$

and the solution should contain 100% E/Z at the visible PSS. This is in perfect agreement with results in table 2.1 and fig. 2.10, which shows that a single exponential law accounts for observation. The reaction rate k_{vis} equals our cross section: $k_{vis} = \sigma = 1.08 \cdot 10^{-18} \text{ cm}^2$.

Under the irradiation of UV light three coupled differential equation are obtained:

$$\frac{dC}{dn} = k_{EC}E \quad (2.13)$$

$$\frac{dE}{dn} = -k_{EC}E - k_{EZ}E + k_{CE}C + k_{ZE}Z \quad (2.14)$$

$$\frac{dZ}{dn} = -k_{ZE}Z + k_{EZ}E \quad (2.15)$$

These differential equations and the scheme in figure 2.1 evidence that the ring closure is not first order reaction rate as demonstrated in figure 2.11 where sigma is not a constant throughout the whole process. The differential equations can be solved by a bi exponential function. The single and bi exponential models of the ring opening and closing reactions are fitted to the experiments in figure 2.8 and 2.9, respectively, by the gray lines for the different light fluxes. The predicted models are in very good agreement with the experimental results.

However, the scheme is unable to explain the PSS^{UV} . In fact, under prolonged UV illumination the solution should consist of 100% C isomers.

The fact that PSS^{UV} does not consist of 100% C form, suggests an additional C→E path, marked by a red arrow in figure 2.14. This additional step was also introduced by Long ([58]) to discuss the fact the UV photoisomerization reactions are not first order reactions.

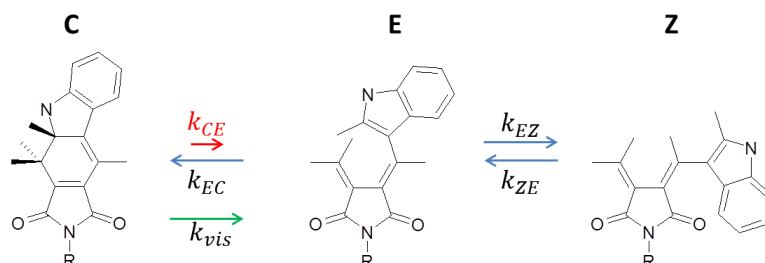


FIGURE 2.14: Reaction paths for the indolyl-fulgimide under visible (\rightarrow) and UV (\leftrightarrow) irradiation

In support of this modification, we measured that some slow ring opening occurs when starting from a C-solution (data not shown) which are in accordance with the experiments reported in [58]. The differential equation 2.13 therefore contains the additional term $-k_{CE}C$. Considering the PSS^{UV} ($\frac{dC}{dt} = 0$) in the chemical equilibrium one can express k_{CE} as a function of the other rates:

$$k_{CE} = \frac{23}{77} \frac{1}{1 + \frac{k_{EZ}}{k_{ZE}}} \cdot k_{EC} \quad (2.16)$$

Finally measurements performed by the group of Rück-Braun that synthesize the molecules measure an isomeric composition at the PSS^{UV} to be 77% C, 21% E and 2% Z isomers using high-performance liquid chromatography [56]. Thereby the reaction rates for the ring opening and closing isomerization are calculated and listed in table 2.3.

rate	k_{vis}	k_{EC}	k_{CE}	k_{EZ}
	$1.01 \cdot 10^{-18} \text{ cm}^2$	$6.7 \cdot 10^{-18} \text{ cm}^2$	$1.8 \cdot 10^{-18} \text{ cm}^2$	$2/21 \cdot k_{ZE}$

TABLE 2.3: Numerical values for the reaction rates in acetonitrile per photon of 525 nm or 365 nm.

The cross sections and quantum efficiencies of the ring closing reaction (table 2.2) are higher ($\geq 20\%$) than for the ring opening reaction which is in agreement with the literature [49, 73, 78].

2.4 Conclusion

The photo isomerization of indolyl-fulgimide was studied in acetonitrile by UV visible spectroscopy. Reversible switching between the visible and UV photo stationary states has been shown. The isomeric composition of the PSS^{vis} and PSS^{UV} has been determined. The PSS^{vis} consists purely of open fulgimide. On the other hand the isomeric composition at the PSS^{UV} consists of 23% open fulgimide and 77% closed fulgimide.

The isomerization cross sections and quantum efficiencies were determined for the ring opening and ring closing reaction under visible and UV light to be $1.1 \cdot 10^{-18} \text{ cm}^2$ and $8.3 \cdot 10^{-18} \text{ cm}^2$, respectively. The cross section and quantum efficiency for the ring opening reaction strongly depend on the wavelength of the exciting light due to optical excess energy.

The ring opening reaction follows first order kinetics due to its single reaction path. The ring closing reaction does not obey this law because several isomerization paths are possible.

Chapter 3

Influence of the Light Polarization on Photo-Switching Properties of Fulgimide Monolayers

3.1 Introduction

The observation of photochromism in 2D monolayer has raised large attention and proved to be very much dependent on the system molecule - substrate. Besides the electronic interaction between the molecules and the substrate mentioned in the general introduction, geometrical factors must be taken into consideration. The isomerization of a molecule includes conformational changes and consequently a minimum free volume is necessary around the photochromic compound. The atomic groups that are rearranged during the isomerization should not be strongly interacting with surface or monolayer. Therefore, if the packing density of the photochrome exceeds a critical value, some photo-isomerization is hindered. For example azobenzene monolayers show no photochromism for surface densities higher than $2.5 \cdot 10^{14} \text{ cm}^{-2}$ [86], but for diluted monolayer the isomerization of azobenzene was observable [87].

Therefore different strategies have been introduced to increase the free space around the photochrome compounds including for example dilution [58, 87], curved surfaces [88] and bulky platforms [89]. In figure 3.1 a dense

SAM is schematized (A). The photochrome density of SAMs on gold can be reduced by mixing azobenzene-thiols with shorter alkane-thiols (B) [87, 90]. Asymmetrical azobenzene thiol were also employed (C) [91–93]. A nice approach was proposed based on a molecular platform consisting of several thiols for one single azobenzene (D) [89, 94, 95]. However, these strategies may lead to aggregation (B), unfavorable orientation of the photochromes (C) or are chemically expensive (D).

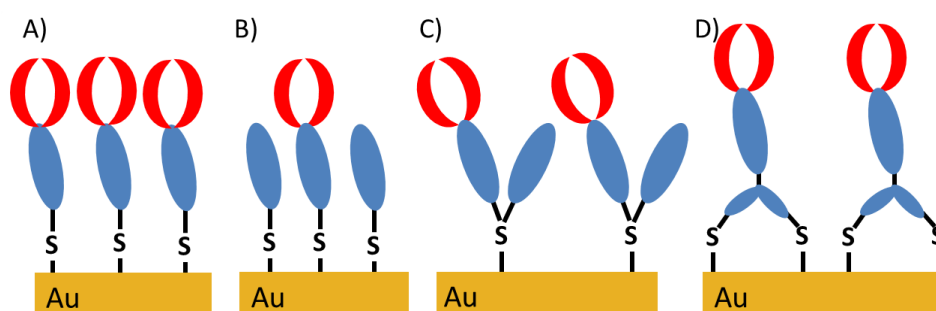


FIGURE 3.1: Dense photochromic SAM (A) and different strategies to increase the free volume around the photochromes: mixed azobenzene-thiol alkane-thiol SAM (B), unsymmetrical azobenzene thiol (C) and molecular platforms (D).

In spite of all these attempts, it was found that azobenzene monolayers with different densities commute with the same cross section and that only the total number of switched photochromes is affected [90]. The commutation speed of the cis trans and trans cis isomerization is indeed the same for different dilutions.

The photo switching of photochromes attached to surfaces was monitored by various techniques. The isomerization of single isomers can be observed by image giving methods like scanning tunneling microscope (STM) [39, 41, 96, 97] or conductive AFM [98] to study the local isomerization. The photo commutation can be indirectly measured by the macroscopic contact angle exploiting different polarities of the isomers [10, 99, 100]. However, none of these techniques allow measuring the dynamics of the photo isomerization. The switching can be read out by electro-chemical measurements [101–103].

Global characteristics of the photo switching process can be studied by optical methods such as UV visible absorbance spectroscopy [6, 9, 89, 99],

reflectance spectroscopy [9, 104], fluorescence [105] or surface plasmon resonance (SPR) spectroscopy [106]. All those methods allowed to measure the switching kinetics of the isomerization of azobenzene SAM [89, 92, 106]. Furthermore, surface enhanced Raman spectroscopy (SERS) [107, 108] or infrared spectroscopy [55, 56, 109] allow to study the switching kinetics of photochromic monolayers.

Two photon techniques have been used for instance on gold in ultra high vacuum, e.g. the isomerization kinetics of absorbed azobenzene at different temperatures have been examined by like two-photon photoemission [36]. The isomerization kinetics of photochromic monolayers have also been measured using second harmonic generation (SHG) [57], sum frequency generation [87, 110, 111] or near-edge X-ray absorption fine structure (NEXAFS) [104].

Although many different measurement techniques have been used to study the photo isomerization at surfaces, quantitative information about the photochrome density and number of switched compounds are the exception [55].

The photo-switching kinetics of photochromes at the surface is generally different from solution. The cis-trans isomerization kinetics of diluted azobenzene monolayers shows significant deviations from the expected first order kinetics [92]. This is interpreted as steric hindrance and includes that the steric effects increase during the commutation. Nevertheless, for other diluted systems there is indication for mainly first order kinetics [89, 106]. But discrimination between single exponential and more complex switching kinetics requires very precise data. Due to bad signal to noise ratios often first order kinetics are simply assumed.

From previous studies it appears obvious that the photo commutation is modified in 2D monolayers. It is, however, difficult to disentangle the influence of the possible effects responsible for the experimental observations. Theoretical studies based on quantum mechanical and molecular mechanics showed that the switching properties of azobenzene can be reduced due to Van der Waals interaction with the substrate [112] and that electronic

coupling with the substrate may completely suppress the photochromism [39]. On the other hand, electronic coupling between two azobenzenes does not affect the quantum efficiency with respect to an isolated photochrome whereas embedding the same dimer inside a monolayer significantly lowers the quantum efficiency [113] although electronic interaction between adjacent azobenzene should be similar (π -stacking) in both situations.

Besides above mentioned effects, another important difference between the photo switching in solution and in 2D at surfaces is the different local electromagnetic environment. This point has been rarely considered for photochromic 2D monolayers although it is a well-known question in photo-chemistry at metal surfaces [114]. The dielectric environment is taken into consideration in terms of electronic interaction of the photochrome with its local environment at the surface and photochrome-solvent interaction via the dielectric constant [76, 115, 116]. To the best of my knowledge the effect of the dielectric environment on the electric field \vec{E} of the exciting light was not systematically examined although this should play a crucial role in the light absorption process.

The primary aim of this chapter is therefore investigating the influence of local electromagnetic environment on the characteristic parameters of photoswitching in 2D. Fulgimide monolayers on silicon surfaces (see **chapter 1**) will be used as model system. As indicated in the general introduction, fulgimide photo-isomerization has been investigated only very recently on silicon substrates [55–58]. In the PhD of Long preliminary measurements are made but no conclusion could be made due to the lack of sufficient precision on effective σ values.

In this chapter we first revisit past characterizations with an improved experimental setup, as well as a new procedures to analyze FTIR data for better precision on the determination of the effective cross sections (σ). Thanks to these improvements we are able to discuss the influence of light polarization on σ . The kinetics of photo-isomerization will be monitored by FTIR as done before [55, 58] as a function of surface density of immobilized fulgimides, photon flux and light polarization. In the continuation of this

chapter, we will examine the influence of plasmonic Au nanoparticles in **chapter 5**.

3.2 Electromagnetic environment in different systems

The photo isomerization is induced by the absorption of a photon. The absorption of light depends on the alignment between the electric field \vec{E} of the photon and the transition dipole \vec{P} of the molecule. For parallel orientation the absorption cross section σ_{\parallel} may be bigger than for perpendicular orientation σ_{\perp} . The absorbance of the molecule can be written as:

$$\sigma_{abs} \propto \sigma_{\perp} \sin^2(\theta) + \sigma_{\parallel} \cos^2(\theta) \quad (3.1)$$

with the $\theta = \angle(\vec{P}, \vec{E})$ [117–119]. Given that $\sigma_{\parallel} \gg \sigma_{\perp}$ and respecting the intensity of the electric field one obtains:

$$\sigma_{abs} \propto \int |\vec{E} \cdot \vec{P}|^2 dV \quad (3.2)$$

Thus the isomerization cross section is expected to depend on the electric field via the absorption cross section:

$$\sigma_{iso} \propto \sigma_{abs}(\vec{E}) \quad (3.3)$$

For comparison of experiments in solution and on surfaces the angle dependency needs to be taken into account as done by Krekieh et al. [89].

In solution the environment is homogeneous and the fulgimide have an isotropic distribution. The effective electric field seen by photochromes depends on the electromagnetic properties of the solvent and is given by the Polo-Wilson equation [120]:

$$\frac{\vec{E}_{sol}^2}{\vec{E}_{vac}^2} = \frac{1}{n} \left(\frac{n^2 + 2}{3} \right)^2 \quad (3.4)$$

where n is the refractive index of the solvent.

The local environment of the photochromes attached on a surface is no longer isotropic. The local electric field experienced by the photochrome depends on the incident angle of the light θ , the wavelength, its polarization and the dielectric function $\epsilon_{si} = \epsilon_1 + i\epsilon_2$ of silicon. The electric field of the

incident light at \vec{r} at time t can be written by

$$\vec{E}(\vec{r}, t) = \vec{E}_{vac} \exp(i\vec{k}\vec{r} - \omega t) \quad (3.5)$$

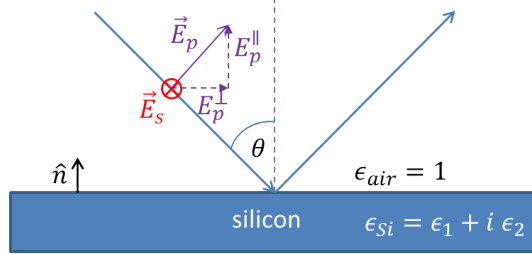


FIGURE 3.2: The different electric fields at the silicon air interface

The electric field is divided in the components \vec{E}_s and \vec{E}_p : \vec{E}_s is purely perpendicular to the surface normal \hat{n} whereas \vec{E}_p has a parallel component to \hat{n} (see 3.2). The displacement field $\vec{D} = \epsilon_{Si}\vec{E}$ represents the electronic effect of the charges in silicon due to an electric field \vec{E} .

At the surface the electric field can be calculated by Maxwell's equations. For a non magnetic medium one obtains the boundary conditions:

$$D_{\parallel} \text{ continuous (no surface free charge)} \quad D_{\parallel air} - D_{\parallel si} = 0 \quad (3.6)$$

$$E_{\perp} \text{ continuous} \quad E_{\perp air} - E_{\perp si} = 0 \quad (3.7)$$

Thereby the electric field for the different polarizations can be calculated for air at the interface. For the s polarization \vec{E}_s one obtains[121]:

$$E_s = \left(1 - \frac{\sqrt{\epsilon_{si} - \sin^2(\theta)} - \cos(\theta)}{\sqrt{\epsilon_{si} - \sin^2(\theta)} + \cos(\theta)} \right) E_{vac} \quad (3.8)$$

and the two components of the p polarizations:

$$E_p^{\parallel} = \left(1 + \frac{\epsilon_{si} \cos(\theta) - \sqrt{\epsilon_{si} - \sin^2(\theta)}}{\epsilon_{si} \cos(\theta) + \sqrt{\epsilon_{si} - \sin^2(\theta)}} \right) \sin(\theta) E_{vac} \quad (3.9)$$

$$E_p^{\perp} = \left(1 - \frac{\sqrt{\epsilon_{si} - \sin^2(\theta)} - \cos(\theta)}{\sqrt{\epsilon_{si} - \sin^2(\theta)} + \cos(\theta)} \right) \cos(\theta) E_{vac} \quad (3.10)$$

wavelength	ϵ_1	ϵ_2
365 nm	35.22	35.28
525 nm	17.44	0.44

TABLE 3.1: Dielectric function of silicon ϵ_{si} for UV and green light [122]

The intensity of the local electric field can thereby be calculated in units relative to its value in vacuum. Table 3.2 gives $c_{loc} = \left| \frac{E_{loc}}{E_{vac}} \right|^2$. The electric field parallel to the surface normal c_p^{\parallel} is about one order of magnitude higher than the in plane components c_p^{\perp} and c_s . The total electric field in p polarization is $c_p = c_p^{\perp} + c_p^{\parallel}$. In fact for a perfect conductor the in plane electric field should even vanish.

wavelength	acetonitrile c_{sol}	$\theta = 45^\circ$			$\theta = 0^\circ$		
		c_s	c_p^{\parallel}	c_p^{\perp}	c_s	c_p^{\parallel}	c_p^{\perp}
365 nm	1.20	0.034	1.42	0.017	0.063	0	0.063
525 nm	1.20	0.086	1.12	0.043	0.149	0	0.149

TABLE 3.2: Local electric field intensities for the different environments for UV and green light.

3.3 Methodology of the data analysis

The methodology used to analyze the isomerization kinetics is explained by one example about a dense C monolayer with a density of $1.8 \cdot 10^{14} \text{ cm}^{-2}$.

The open and closed fulgimide can be distinguished by different infrared absorbance bands in the carbonyl region [66]. This is displayed for two different pure monolayers consisting only open or closed monolayer in figure 3.3. A pure C and E monolayer with surface densities of $N_{pureC} = 1.8 \cdot 10^{14} \text{ cm}^{-2}$ and $N_{pureE} = 1.7 \cdot 10^{14} \text{ cm}^{-2}$ are shown in blue and red. The peak positions of the main peak for the closed and open fulgimide monolayer are 1698 cm^{-1} and 1689 cm^{-1} , respectively. These intense infrared bands in the carbonyl regions will be used to monitor the photo switching of the fulgimide monolayer.

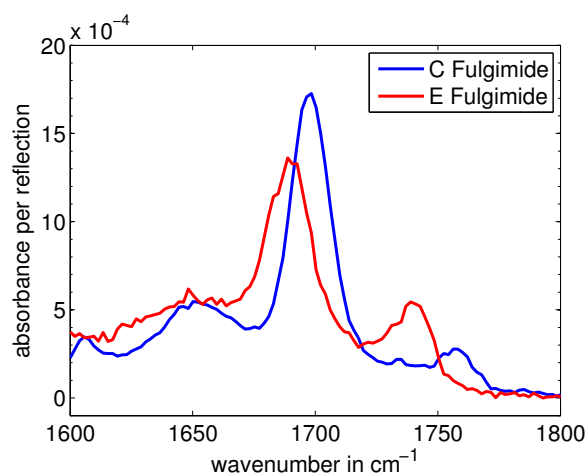


FIGURE 3.3: Infrared absorbance in the carbonyl region of pure C and E fulgimide monolayer. The reference is the hydrogen terminated silicon surface.

The as prepared C monolayer of figure 3.3 is irradiated by green light of 525 nm. The infrared absorbances in the carbonyl region after successive light pulses are displayed in figure 3.4.

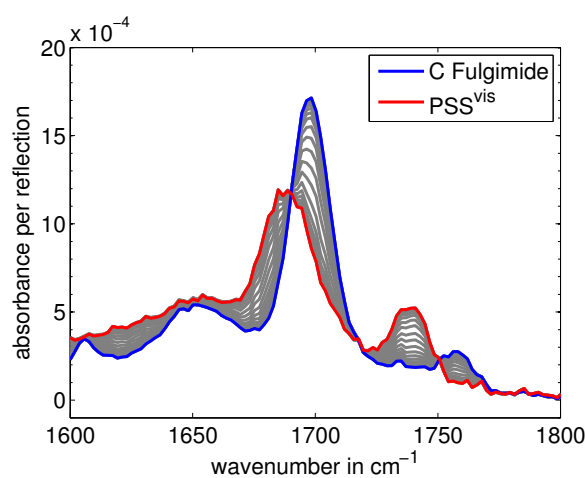


FIGURE 3.4: Change of the infrared spectrum of a as prepared C monolayer due to visible illumination.

A continuous change of the infrared spectrum due to the illumination is monitored. The irradiation is continued until no change of the infrared spectrum is observed any more and the visible photo stationary state (PSS^{vis}) is reached. A comparison with the as prepared E/Z monolayer indicates that most closed fulgimides should have been switched to open isomers because the final infrared spectrum after irradiation strongly resembles that of a as prepared E monolayer. The peak position changes from

1690 cm^{-1} to 1689 cm^{-1} , which is indeed the peak position in figure 3.3.

Subsequent illumination with UV light reverses the change of the infrared spectrum: the main peak tends again to greater wavenumbers. However, the obtained peak position and infrared spectrum at the UV photo stationary state (PSS^{UV}) do not exactly correspond to the ones of the initial as prepared C fulgimide monolayer. This introduces a fatigue or photo degradation effect that will be discussed later.

3.3.1 Quantitative monitoring of the photo switching

For a quantitative determination of the photo switch one must monitor the change of the infrared absorbance. The best way is using differential spectra as displayed in figure 3.5 (left). The reference of the differential spectra is that of the sample just before the first light pulse. All spectra can be overlaid until the final one, using a scaling factor α .

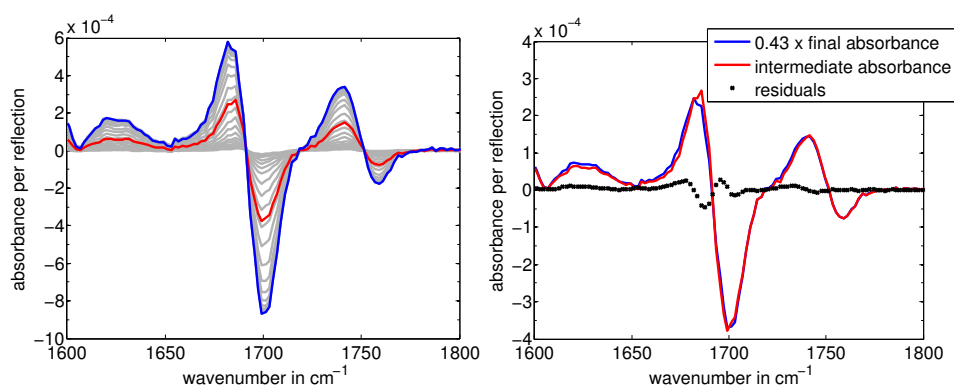


FIGURE 3.5: Left: Differential curves of the ring opening reaction for a dense monolayer. Right: scaled final absorbance using 0.43 to match the intermediate red spectrum

In the right panel of 3.5 the final (blue) absorbance from the left figure is multiplied by a scaling factor $\alpha = 0.43$ to match the intermediate red curve. The residuals are shown in black.

The relative advancement of the reaction was therefore quantitatively described by the scaling factor $0 < \alpha < 1$.

$$\alpha(t) = \frac{abs(t)}{abs(t_{max})} \quad (3.11)$$

Figure 3.6 shows the time dependence of the scaling factor α . The relative advancement at the beginning is relatively quick and then slowly saturates to 1.

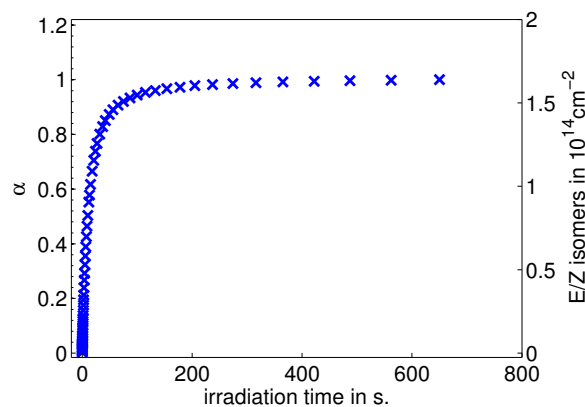


FIGURE 3.6: Scaling factor $\alpha(t)$ and the number of switched isomers $N(t)$ for the C \rightarrow E isomerization of the dense C monolayer ($1.8 \cdot 10^{14} \text{ cm}^{-2}$).

The number of switched isomers at the end of the commutation $N(t_{final})$ must now be determined. To do so the change of the infrared absorbance due to the isomerization of a single isomer is calculated by the difference of the as prepared C and E infrared absorbances normalized with their densities. The expected differential infrared absorbance of a single isomer per unit area is displayed in the left panel of figure 3.7. The curve follows the same characteristics like the differential absorbances during the commutations, both curves are homothetic.

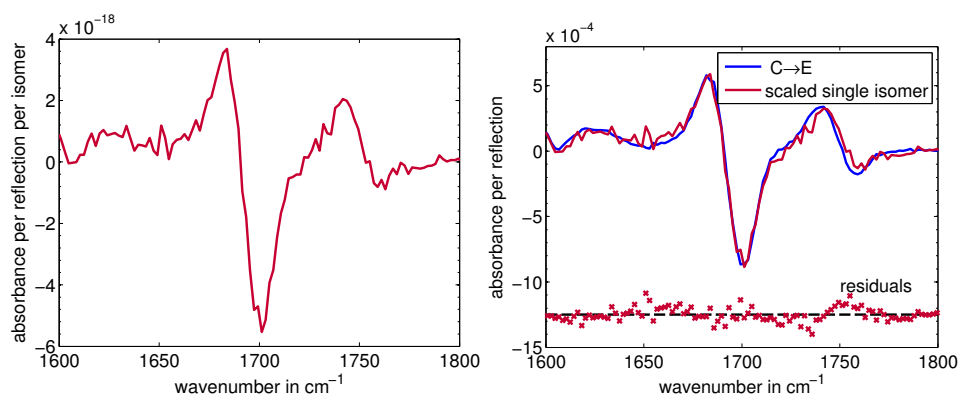


FIGURE 3.7: Left: Change of the infrared spectrum due C \rightarrow E or a single isomer. Right: scaled differential absorbance of a single isomer to fit the differential curve of a commutation of a whole monolayer (blue curve before in 3.5). Residuals are displayed in black.

The right panel of 3.7 shows again the differential absorbance spectrum at the end of the isomerization (from 3.5). In red the characteristic absorption of the isomerization of a single isomer is scaled up to match the blue curve. The residuals (red crosses) do not show any systematics. The scaling factor of $1.6 \cdot 10^{14}$ represents the number of switched isomers per cm^2 .

The number of open E-isomers $E(t)$ at the irradiation time t can be determined by

$$E(t) = \alpha(t) \cdot E(t_{final}) \quad (3.12)$$

Therefore the relative advancement in figure 3.6 can be extended by the quantitative number of switched isomers on the right y-axes.

3.3.2 Determination characteristic parameters of the photo switching

It is more meaningful to study the photo switching as a function of the photon dose instead of illumination time. As in solution the photo switching of fulgimide monolayer has been studied as a function of the light flux. The non polarized photon fluxes for the ring opening and ring closing isomerization have been varied by one order of magnitude.

The kinetic curves for the different commutations can be seen in figure 3.8. The left panel shows the kinetic curves for the ring opening reaction, the right panel the ring closing reaction for the different light fluxes.

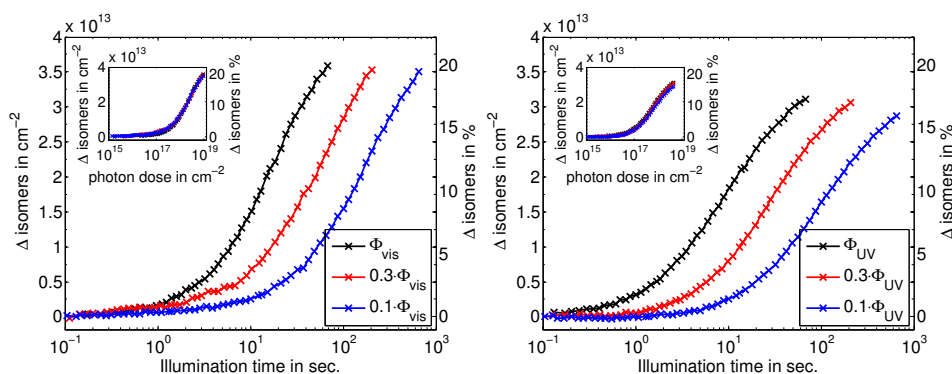


FIGURE 3.8: Photo switching curves for the ring opening (left) and closing reaction (right) using different light fluxes vs the illumination time. The insets show the same curves normalized with the number of irradiated photons.

As in solution (see figure 2.8) all curves overlap when plotted as a function of the photon dose. Therefore all results will be discussed as a function of the photon dose instead of irradiation time.

Determination of the photo stationary states

For a complete data analysis one needs to reach the PSS, which is experimentally difficult because limited light exposure is desired to avoid possible photo degradation. It is shown below that the PSS can nevertheless be accurately determined after partial photo commutations.

In figure 3.9 the number of switched isomers is shown (black curve) against the photon dose on a logarithmic x-axis for C→E isomerization of a dense C monolayer ($1.6 \cdot 10^{14} \text{ cm}^{-2}$). The illumination time has been sufficiently long to reach the PSS^{vis} ($1.5 \cdot 10^{14} \text{ cm}^{-2}$) which has a density of $1.6 \cdot 10^{14} \text{ cm}^{-2}$). In the same figure the logarithmic derivative $\frac{dE(n)}{d \ln(n)}$ of the plot is displayed (blue crosses).

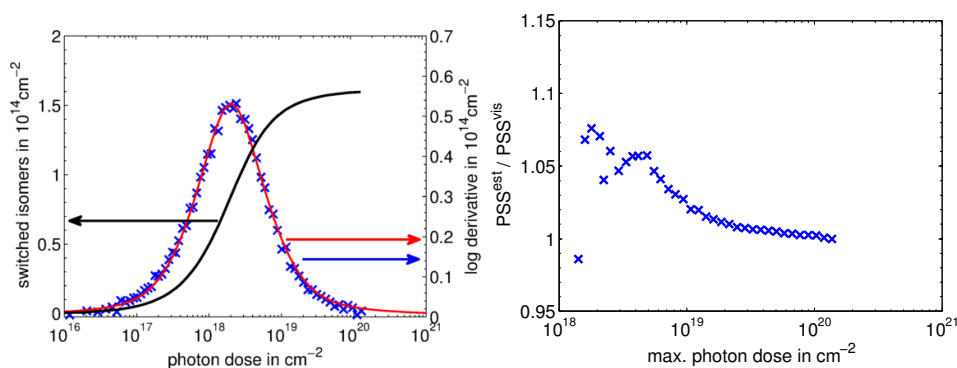


FIGURE 3.9: Left: Photo switching kinetics of a dense C monolayer (black) and its derivative (blue crosses). The derivative follows a pseudo Voigt peak (red). Thereby the photo stationary state can be estimated whose uncertainty is estimated in the right panel as a function of the maximal photon dose.

The logarithmic derivative can be fitted by a pseudo Voigt function $p(n)$ that is plotted in red. For the stabilization of the fitting procedure the degrees of freedom of the pseudo Voigt function are reduced by forcing same Lorentzian and Gaussian width and a fixed Gaussian/Lorentzian ratio. This behavior is indeed observed for all commutation experiments for all samples, regardless the surface density of the monolayer.

For partial photo commutations that have been stopped before reaching PSS, we estimated the expected PSS by extrapolating the plots with the fit of the derivative: $E_{PSS} = E(t_{final}) + \int_{n_{max}}^{\infty} p(n)dn$. The uncertainty of the estimated PSS depends on the photon dose where the commutation is stopped. The panel of 3.9 gives the error on the estimated PSS as a function of the maximal photon dose. The error becomes neglectable above 10^{19} photons/cm² for the ring opening reaction. For earlier stopped isomerization the PSS is overestimated to until around 5%.

To convince the reader figure 3.10 shows the same analysis for a ring opening reaction of a dilute C monolayer of $0.6 \cdot 10^{14}$ cm⁻². Though the numerical derivative is more noisy due to lower photochrome density, the estimation of the PSS is not significantly affected. The uncertainty remains below 5%.

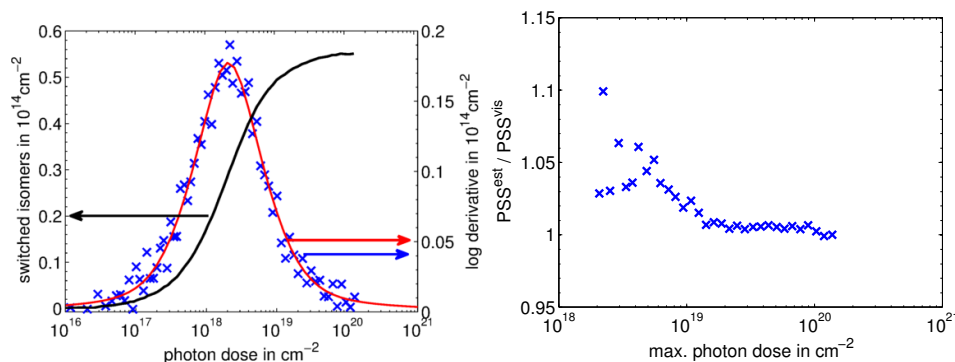


FIGURE 3.10: Photo switching kinetics of a dilute as C monolayer ($0.6 \cdot 10^{14}$ cm⁻²) and its logarithmic derivative. Right: estimation of the uncertainty of the PSS as a function of the irradiated number of photons.

For the ring closing isomerization the PSS is estimated in the same way in figure 3.11. Again the derivative follows the same pseudo Voigt profile. The PSS is estimated like for the ring opening reaction by extrapolation of the fit. The uncertainty of the estimated PSS can not be estimated because in no isomerization the PSS has been experimentally obtained to avoid photo degradation under UV light.

To ensure a reliable estimation the PSS a photon dose should be reached when the derivative has passed its maximum.

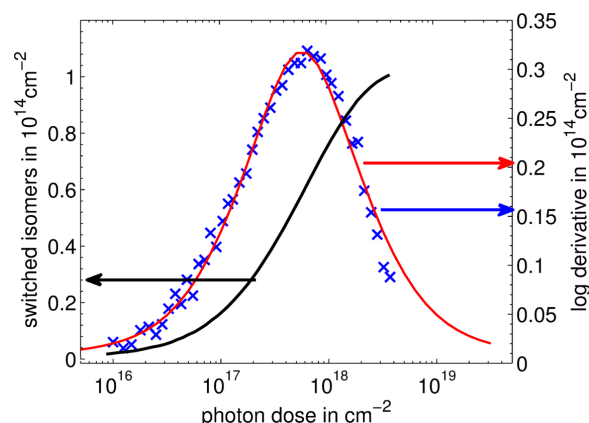


FIGURE 3.11: Ring closing kinetics under UV light (black) and its logarithmic derivative.

Determination of the cross section

On surfaces the isomerization cross section is determined in a similar way as in solution. The numerical cross section (2.4) for the ring opening reaction of a dense C monolayer ($1.6 \cdot 10^{14} \text{ cm}^{-2}$) is shown in figure 3.12 against the photon dose. First the numerical cross section is constant and then decreases continuously, thus overall no first order kinetics are observed.

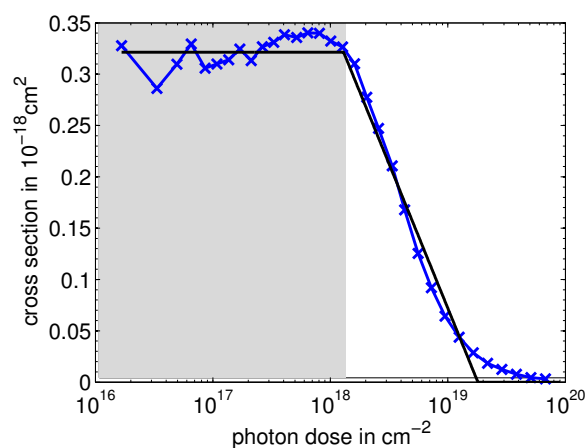


FIGURE 3.12: Numerical cross section for the ring opening reaction

However at the beginning of the isomerization the cross section in the gray area is constant. In these first interval the isomerization can be described by first order kinetics. The gray region is determined by modeling a constant and then linearly decreasing function to σ_{num} .

This linear region is then used to determine the cross section by linear regression using $\ln(1 - E/E_{PSS}) = -\sigma n$ as in solution. The fit is shown in

figure 3.13. The data points in the linear gray region are marked red, the other points that corresponds to greater photon doses are marked in blue. The inset shows the whole photo isomerization including higher photon doses.

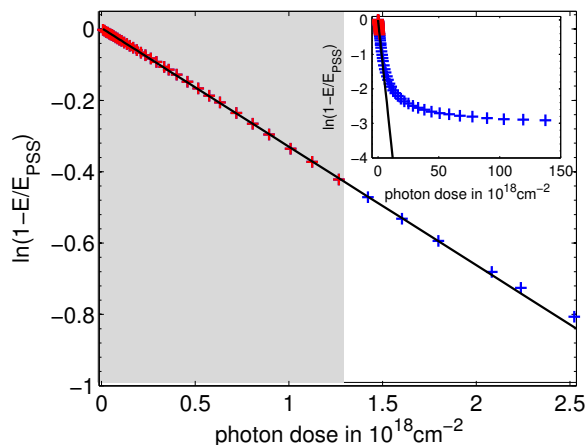


FIGURE 3.13: Determination of the cross section by exponential fit in the linear region defined by the left figure

The slope in the linear region is $\sigma_{C \rightarrow E} = 0.33 \cdot 10^{-18} \text{ cm}^{-2}$. This cross section determined by the fit matches the first numerically determined cross sections σ_{num} . For higher number of photons the switching kinetics is significantly slower and does not follow the initial linear slope. This corresponds to the decreasing σ_{num} at higher photon doses.

The ring closing reaction under UV light is analyzed in the same way. For the same sample as before $\sigma_{num, E \rightarrow C}$ is shown in 3.14. As for the ring opening reaction σ_{num} is constant before and then decreases. Therefore the same model is applied as for the ring opening reaction. First order reaction dynamics are assumed at the beginning of the isomerization and the cross section is calculated using a linear fit. The calculated cross sections $\sigma_{E \rightarrow C} = 1.25 \cdot 10^{-18} \text{ cm}^2$ again corresponds to the plateau of the numerical cross section.

The determination of the cross section by the linear regression reveals more stable results than for example the plateau of the numerical cross section. The numerical derivative in 3.12 for σ_{num} is more sensitive to noise because only two adjacent data points are considered. Including one data point more or less in the linear regression does not significantly change the

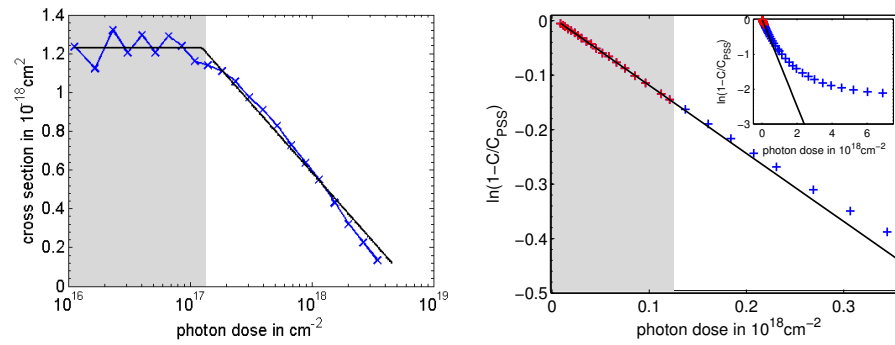


FIGURE 3.14: Left: numerical cross section for the ring closing reaction. Right: determination of the cross section by exponential fit in the linear region defined by the left figure

result because the data points around the border of the linear regime are well matched by the slope. Therefore in the following all mentioned cross sections are determined by fitting the first order dynamics at the beginning and therefore σ_{fit} is simply called σ .

3.4 Results

3.4.1 Isomeric composition at the photo stationary states

The as prepared E fulgimide monolayer ($1.7 \cdot 10^{14} \text{ cm}^{-2}$) is irradiated several times successively with UV and green light for 65 s. The isomeric composition was determined as explained in figure 3.19. The isomeric compositions at the photo stationary states for successive isomerizations are displayed in figure 3.15. First all isomers are in the open E or Z form. After the first isomerization with UV light 65% of the isomers are in the closed form, and 35% remain in the open form. After further successive commutations the PSS slowly drifts to more C fulgimide. This is due to the fact that initially the monolayer consisted of 100% open isomers. After a few switching cycles the number of switched isomers and the PSS are stabilized. Many isomerization cycles can be performed.

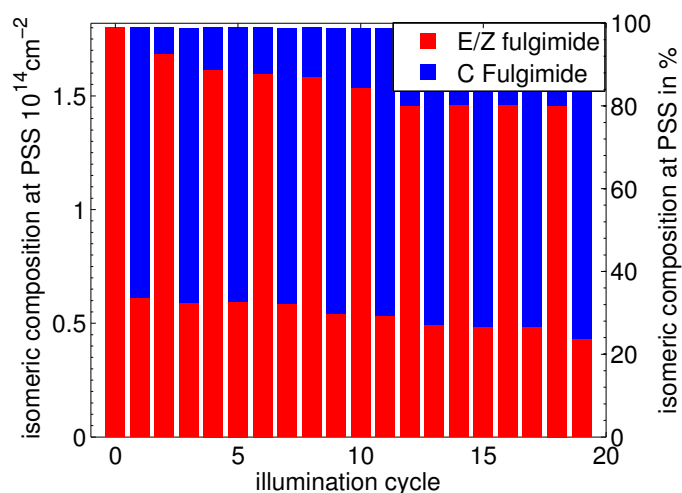


FIGURE 3.15: Isomeric composition at the PSS for successive isomerizations

3.4.2 Photo degradation

The number of switched isomers of the successive isomerizations in figure 3.15 slowly decreases. This indicates the photo degradation under UV light that has been observed in solution, too.

Therefore the same experiment of successive commutations have been performed with an illumination time of 1000s instead of 65s to examine the photo degradation.

It is expected that the photo degradation effect can be reduced by controlling the local atmosphere around the sample [123]. To do so the sample is placed inside a home build cell with controlled atmosphere (see appendix B.2). The evolution of the number of switched isomers is shown in figure 3.16 for different atmospheres.

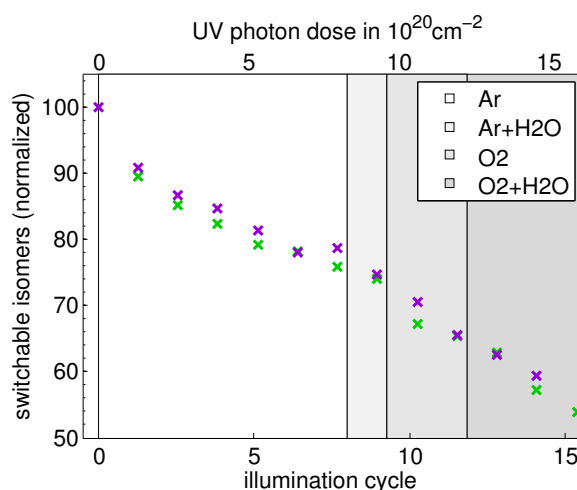


FIGURE 3.16: Number of switched isomers by UV (violet) and green light (green) for increasing UV expose in different environments

The number of switched isomers decreases progressively during the illumination cycles. In solution the photo-degradation is induced by UV light and therefore the top x axes displays the UV photon dose. The gas atmosphere does not appear to have any influence on the degradation of the fulgimide. The number of switched isomers decreases to 50% after a UV photon dose of about $1.5 \cdot 10^{21} \text{ cm}^{-2}$. In 3.11 the photon dose is about $5 \cdot 10^{18} \text{ cm}^{-2}$ and therefore 2.5 orders of magnitude smaller.

The number of UV photons has therefore to be well adjusted to measure the ring closing reaction while avoiding the fatigue effect to ensure reproducible experimental conditions for many experiments. Thus the PSS^{UV} is experimentally never reached completely because this would include a very high photon dose that would damage the sample.

3.4.3 Isomerization kinetics of successive commutations

The switching kinetics of all 19 commutations for the as prepared E monolayer ($1.7 \cdot 10^{14} \text{ cm}^{-2}$) whose PSS have been discussed above (in 3.15) are quantitatively analyzed.

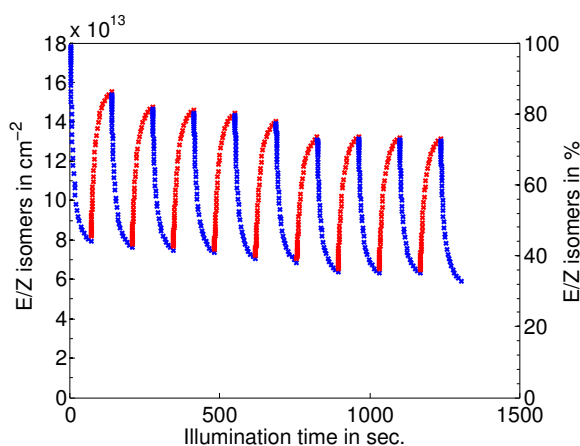


FIGURE 3.17: Successive photo commutation cycles due to UV and visible irradiation

In figure 3.18 the numerical cross sections are calculated for the different isomerizations. The top panels shows the numerical σ_{num} for several $\text{E} \rightarrow \text{C}$ and $\text{C} \rightarrow \text{E}$ photo commutations against photon dose. Despite their different initial isomeric compositions at the beginning the cross sections show similar behaviors for both ring opening and closing reactions. Only the first photo switching of the initial open monolayer reveals a higher cross section. After the first isomerization the switching kinetics are stabilized.

Except for the first photo-isomerization of the as prepared C monolayer (figure 3.19) the number of switched isomers is constantly around $0.9 \cdot 10^{14} \text{ cm}^{-2}$ for every commutation. This demonstrates the photo-degradation was negligible with our procedure

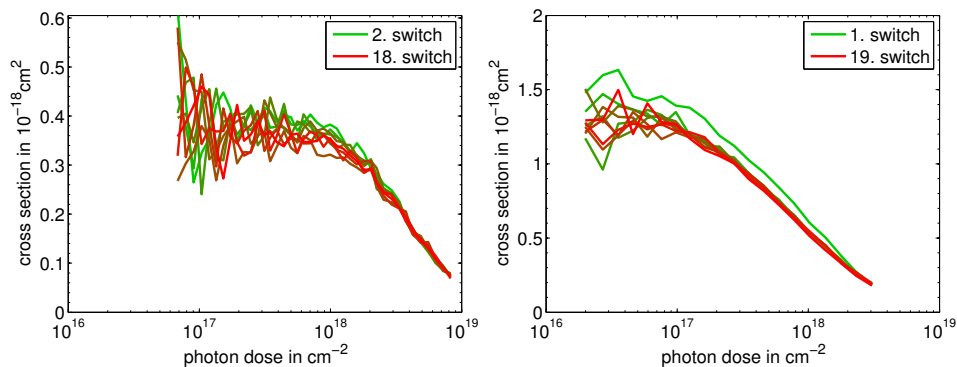


FIGURE 3.18: Numerical cross sections vs. photon dose for successive $C \rightarrow E$ (top left) and $E \rightarrow C$ (top right) commutations.

The cross sections σ for the successive isomerizations are displayed in the right panel of figure 3.19. Except for the first UV-cross section $\sigma_{1,E \rightarrow C} = 1.5 \cdot 10^{-18} \text{ cm}^2$ the cross sections of the subsequent commutations are around $1.3 \cdot 10^{-18} \text{ cm}^2$.

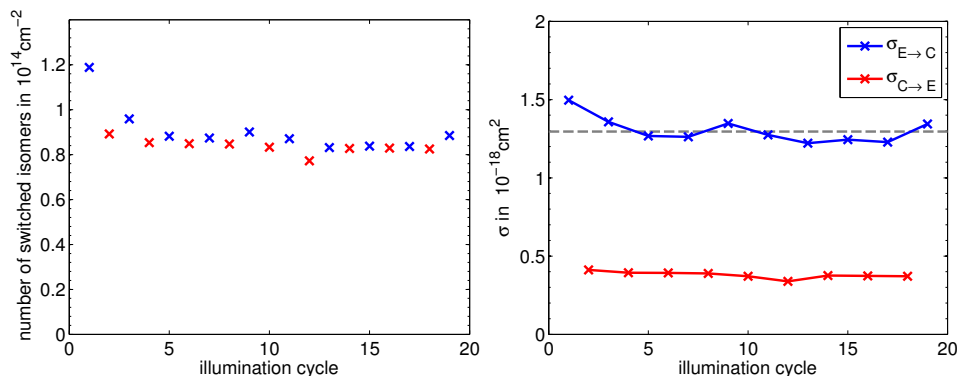


FIGURE 3.19: Evolution of the number of switched isomers (left) and cross sections (right) for successive isomerization cycles of a as prepared E monolayer ($1.7 \cdot 10^{14} \text{ cm}^{-2}$).

3.4.4 Determination of the isomeric composition at the photo stationary states for different surface densities

Figure 3.20 shows that the isomeric composition at the first visible photo stationary state of as prepared C monolayers depends on the photochrome density. The isomeric composition at the PSS^{vis} consists of between 90% E/Z isomers for densest monolayer and of about 100% E/Z isomers below $0.9 \cdot 10^{14} \text{ cm}^{-2}$. Overall the yields of the ring opening reaction due to visible light are close to unity, in particular for dilute monolayer.

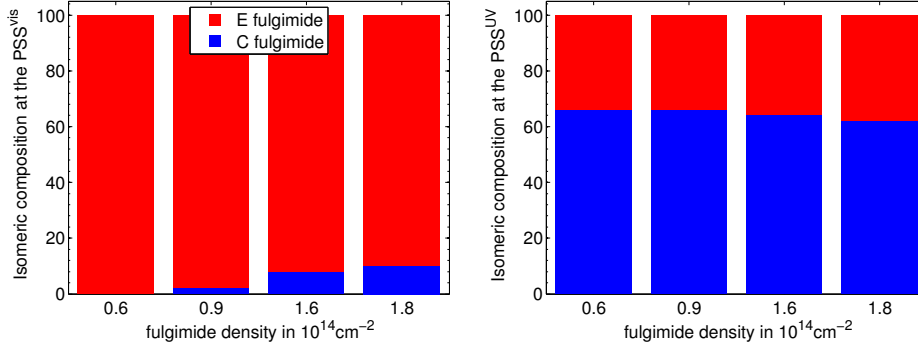


FIGURE 3.20: Isomeric composition at the PSS for the ring opening reaction of as prepared C Fulgimide monolayer (left) and back isomerization (right) for different surface densities

The back isomerization due to UV light shows that a as prepared C surface is never reached. The monolayer is composed of 2/3 of C and 1/3 of E/Z isomers. The same isomeric composition of the PSS^{UV} is reached for the as prepared E/Z monolayer ($1.7 \cdot 10^{14} \text{ cm}^{-2}$) in 3.15. There is a small influence of the monolayer density.

	surface density in 10^{14} cm^{-2}			
	0.6	0.9	1.6	1.8
PSS ^{vis}	100 / 0	98 / 2	92 / 8	90 / 10
PSS ^{UV}	34 / 66	34 / 66	36 / 64	38 / 62

TABLE 3.3: Isomeric composition of C monolayers at the PSS^{vis} and subsequent PSS^{UV}

3.4.5 Influence of the fulgimide density on the cross section

The first ring opening reaction has been investigated as a function of the fulgimide density. All C fulgimide monolayers have been illuminated by non polarized light by an incident angle of 45° . Figure 3.21 shows that the ring opening photo commutation shows similar behavior for all monolayer densities. The cross sections $\sigma_{C \rightarrow E}$ are between $0.33 \cdot 10^{-18} \text{ cm}^2$ to $0.36 \cdot 10^{-18} \text{ cm}^2$ below 10^{18} photons per cm^2 but then continuously decreases.

Afterwards all surfaces have been switched back using UV light. The right panel of figure 3.21 shows that all ring closing reactions present again

a behavior that is independent of the photochrome density. The corresponding cross sections determined by a linear regression for both reactions are given in table 3.4.

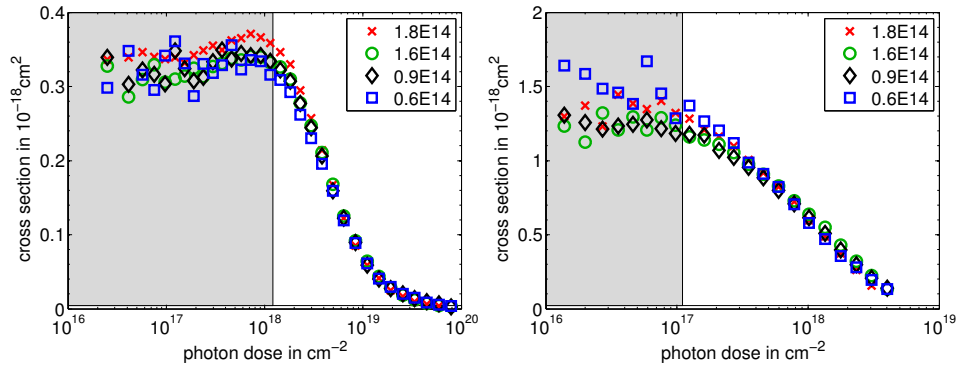


FIGURE 3.21: Left: ring opening commutation for a as prepared C monolayer with different surface densities. Right: subsequent back switching due to UV light for the same fulgimide monolayers.

surface density in 10^{14}cm^{-2}	0.6	0.9	1.6	1.8
$\sigma_{C \rightarrow E}$ in 10^{-18}cm^2	0.330	0.336	0.333	0.358
$\sigma_{E \rightarrow C}$ in 10^{-18}cm^2	1.511	1.314	1.249	1.452

TABLE 3.4: Cross sections for the first ring opening and subsequent ring closing reaction for different photochrome densities

3.4.6 Light dependence of the photo-switching

The effect of light polarization has been investigated on surfaces which have been switched several times with non polarized light to stabilize the photo commutation (as in figure 3.19). For the commutation by p polarized light the incident angle was 45° whereas to obtain s polarized light a normal incidence was used (see 1.5.1). Before a ring closing reaction is measured the sample has been illuminated with unpolarized green light to obtain the PSS^{vis} as the initial state. For the ring opening reaction a quasi PSS^{UV} has been reached by unpolarized UV light. Thereby it is ensured that only commutations from a comparable initial state are compared. Several commutations have been done to determine the cross sections.

Raw kinetic curves for the different commutations under polarized light are presented in the appendix B.5. The resulting cross sections for the ring opening and closing reactions are displayed in figure 3.22. Under p polarized light the cross sections (blue) are systematical higher than under s polarized light for both photo isomerizations (red). The p polarized cross sections are rather stable. For an increasing surface density the cross section for s polarized light decreases. The higher cross sections in acetonitrile are shown as a reference (filled symbols). The cross sections are also listed in table 3.5.

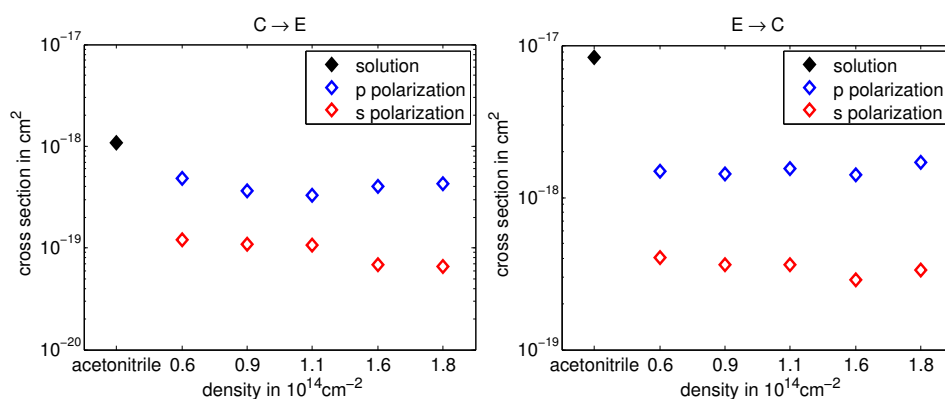


FIGURE 3.22: Cross section for different polarizations for the ring opening (left) and closing reactions (right)

cross section in 10^{-18} cm^2	polarization	surface density in 10^{14} cm^{-2}				
		0.6	0.9	1.1	1.6	1.8
$\sigma_{C \rightarrow E, p-pol}$ (green)	p	0.48	0.36	0.33	0.40	0.42
$\sigma_{C \rightarrow E, s-pol}$ (green)	s	0.120	0.108	0.107	0.068	0.060
$\sigma_{E \rightarrow C, p-pol}$ (UV)	p	1.49	1.43	1.55	1.41	1.69
$\sigma_{E \rightarrow C, s-pol}$ (UV)	s	0.40	0.36	0.36	0.29	0.33

TABLE 3.5: Cross sections for the ring opening and ring closing reaction under s and p polarization for various densities

3.5 Discussion

3.5.1 Influence of the surface density on the photo commutation

The critical packing density for fulgimide on silicon monolayers is $1.3 \cdot 10^{14} \text{ cm}^{-2}$ [55]. The alignment and packing of the indolyl-fulgimide is displayed in figure 3.23.

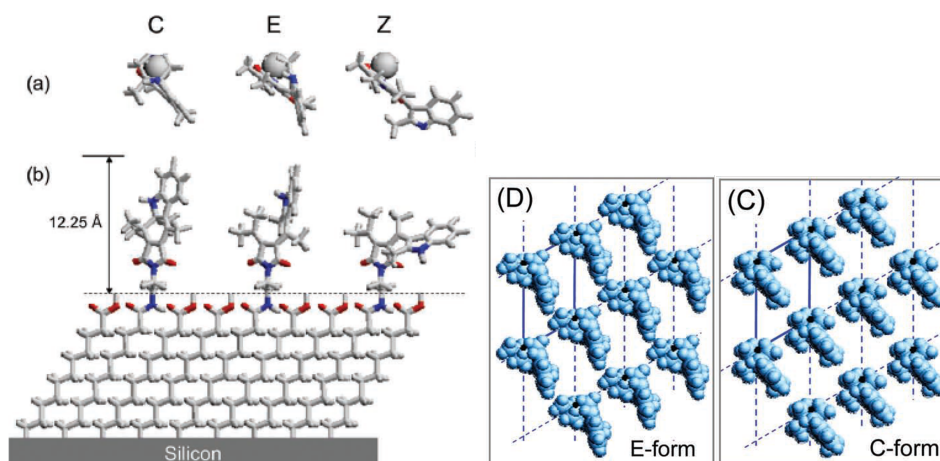


FIGURE 3.23: Alignment of the C, E and Z fulgimide and the surface packing of pure E and C monolayers. Taken from [55]

Despite the high photochrome density of $1.8 \cdot 10^{14} \text{ cm}^{-2}$ the surface remains photo switchable. However, C monolayers with densities above the critical packing show a significant number of non switched isomers in the first PSS^{vis} 3.20. On the other hand for monolayers with a lower surface density mainly all isomers of the C fulgimide monolayer are switchable as in solution.

For the ring closing reaction on the other hand all surfaces show similar PSS^{UV} of about 2/3 C and 1/3 E/Z isomers. The surface density only has a minor influence. The slightly higher C fraction for the dense monolayer after (E→C) can be motivated by the non switched C isomers that remained on the surface after the first C→E commutation.

This indicates that the isomeric composition at the PSS^{UV} is dominated by the chemical equilibrium of the $\text{C} \rightleftharpoons \text{E}$ reaction under UV irradiation as derived from the experiments in solution (2.14 and 2.16). The different isomeric composition at the PSS^{UV} on surfaces (66 / 34) with respect to the

solution (73 / 23) can therefore be understood in a relative change of the different k_{ij} reaction rates for the open isomers that appear to interact with the surface due to their alignment.

Recall that according to our definition (see 2.3) the cross section σ is defined by the isomers that are switchable and that the non-switched isomers have no influence on σ at the beginning of the isomerization below a critical photon dose. Thereby the surface density only has a minor influence on the photo isomerization cross section σ for both the ring opening and closing reaction 3.21.

The decreasing numerical cross section at different densities will be further discussed in greater detail in the next chapter.

3.5.2 Polarization dependent isomerization

In figure 3.24 the cross sections of a dense monolayer ($1.6 \cdot 10^{14} \text{ cm}^{-2}$) are shown as a function of the relative local field intensities (see 3.2) for the ring opening and closing reactions. For non-polarized light the cross sections are within the interval stated in the literature [57, 58]. The cross sections for the corresponding photo commutation in acetonitrile is displayed as a reference (filled symbol). The cross section due to s and p polarized light lay on the same gray dashed line passing through origin which is consistent with the fact that the photo-switching process is stimulated by the absorption of the photon by the photochrome which is proportional to the intensity of the local electric field.

Even when the electric field intensity is considered in the isotropic case in solution the cross section is higher than on the surfaces (anisotropic case), in particular for the ring closing reaction in the right panel (E→C). The exact cross section of the anisotropic environment in solution furthermore depends on the polarity [73, 124] and viscosity [83, 85] of the solvent.

3.5.3 Isomerization transition dipole

Due to the electric field intensity dependence it is more meaningful to normalize the cross section with its local electric field intensity c_{loc} defined at

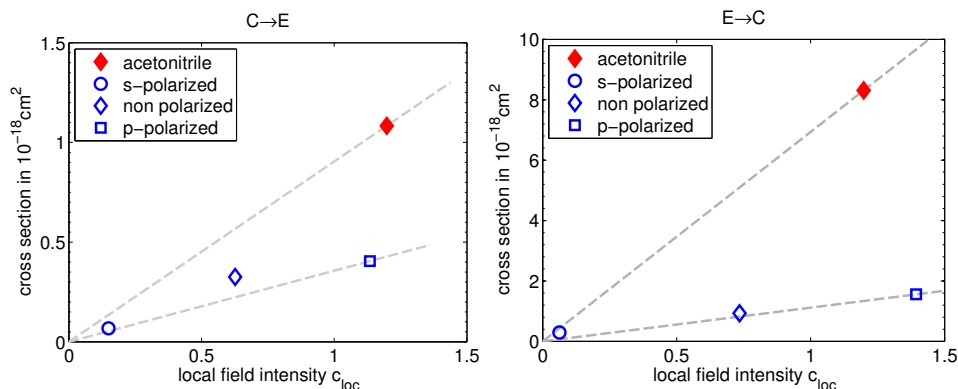


FIGURE 3.24: Cross sections for ring opening and closing isomerizations for a dense fulgimide monolayer against the intensity of the local electric field.

the beginning of this chapter:

$$\bar{\sigma}_{s,p} = \frac{\sigma_{s,p}}{c_{s,p}} \quad (3.13)$$

In figure 3.25 the ratios of the different normalized cross sections for s and p polarization are displayed for the ring opening and closing isomerization at different densities. Normalized with the electric field intensity the cross section for s polarized light is higher than for p polarized light, in particular for the ring closing reaction (E→C). The ratio changes for different surface densities.

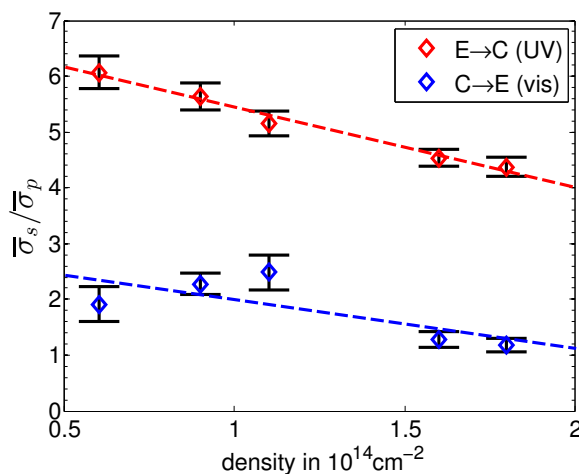


FIGURE 3.25: Ratio of the electric field intensity normalized cross sections for s and p polarization for different surface densities

This indicates an anisotropy of the photo isomerization. This anisotropy

is due to the absorbance dependent dipole \vec{P} of the fulgimide. In fact an anisotropy of a photochrome is expected when the polarizability is anisotropic which is the case for the studied fulgimide for both C and E isomers [57] (see 3.2). The electric field \vec{E} and the transition dipole \vec{P} are displayed in 3.26 for an surface in \vec{e}_1 - \vec{e}_2 plane. The angle α of the electric field \vec{E} is 90° for s polarized light and 6° (365 nm) or 11° (525 nm) for p polarized light.

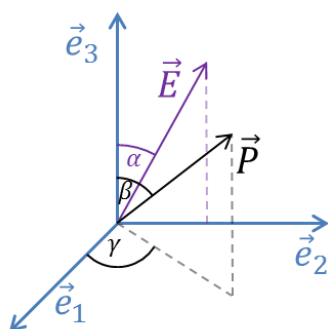


FIGURE 3.26: Local electric field and the transition dipole at the surface

Globally on the whole substrate it can be assumed that the molecules are distributed homogeneously with respect to γ . This simplifies the expression for the cross section as a function of the transition dipole (from 3.2) to

$$\sigma \propto \int_0^{2\pi} (\vec{E} \cdot \vec{P})^2 d\gamma (2\pi)^{-1} = \cos(\alpha)^2 \cos(\beta)^2 + 0.5 \sin(\alpha)^2 \sin(\beta)^2 \quad (3.14)$$

The ratios of the cross sections in 3.26 therefore indicate an transition dipole for the E/Z and C isomers to be 72° and 65° with respect to the surface normal for dense monolayer, respectively. Considering the alignment of the fulgimide on the surface (in 3.23) these angles are in agreement with the rather straight C isomer and the more flat aligned E and Z isomer. Although the changes of the ratios of the normalized cross sections are relatively big, the resulting transition dipole angles E/Z and C isomers on dilute monolayers only changes slightly to 74° and 58° , respectively. The change of the cross sections and resulting transition dipole points in the direction that the isomers are aligned slightly more upwards for dense monolayers and tend to be slightly more flat aligned for diluted monolayers.

3.6 Conclusions

The photo commutation of fulgimide terminated monolayer on silicon has been measured by in situ FTIR. The qualitative and quantitative analysis shows the successful switching of fulgimide from the closed to the open form by visible light and the back isomerization by UV light. The isomeric compositions at the visible and UV photo stationary states are determined. The number of switched isomers on dilute surfaces is higher with respect to the total number of photochromes for the ring opening reaction but not for the ring closing reaction.

The photo commutation kinetic is measured using different light fluxes. The switching progress scales with the intensity of the light flux and is consequently characterized by the number of irradiated photons. The kinetic curves can not be satisfyingly described by single or bi-exponential functions. Isomerization cross sections are calculated and similar kinetics for different surface densities are observed. Independent of the photochrome surface density the cross sections decrease during the photo commutations.

Good reversibility of the photo commutation has been found over many switching cycles. The number of switched isomers and the kinetic parameter are reproducible. A photo-chemical fatigue effect is measured for long UV light exposure.

The photo commutation rate is significantly higher for p polarized light with respect to s polarized light due to the higher electric field intensity. The cross sections for the ring opening reaction for the different polarizations show a proportional behavior with respect to the electric field intensity. Electric field intensity normalized cross sections indicate a transition dipole that qualitatively corresponds to the alignment of the isomers on the surface.

Chapter 4

Influence of Temperature on the Photo Commutation of Fulgimides on Silicon Surfaces

4.1 Introduction

The temperature influences the photo-commutation of fulgides or fulgimides in solution [45, 48, 75–77]. A schematic energy diagram for the ring opening and closing reaction from Draxler et al. is shown in figure 4.1. The C isomer is excited by visible light to a Franck Condon state and then relaxes to a semi stable intermediate state S1. From that S1 state two reaction paths exist: back to the C isomer and to the open form (here called Z, we call it E). Due to the thermal barriers of the individual reaction rates the isomerization depend on the temperature.

In this chapter the ring opening and closing photo isomerization of fulgimide monolayer are measured for different temperatures. The data are discussed in terms of an energy diagram. It will also be shown that results from a Monte Carlo simulation of the photo commutation explain observations of this chapter and chapter 3 above the critical photon dose where the cross section decreases.

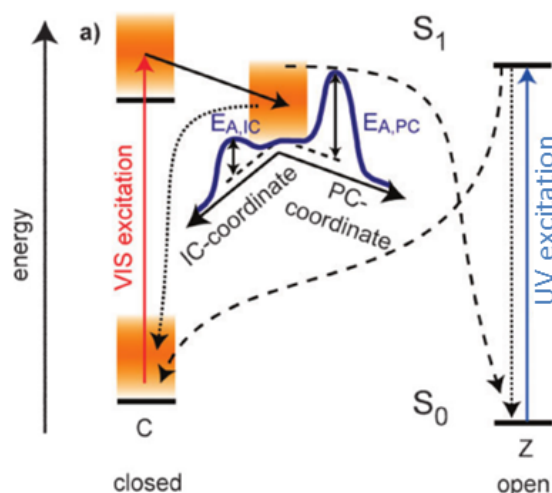


FIGURE 4.1: Reaction scheme for the ring opening reaction including an intermediate state with thermal barriers for different reaction paths. Taken from [46]

4.2 Temperature influence on the switching kinetic

Experimental details including the temperature determination are explained in detail in appendix C.

First the thermal stability of the monolayer was checked. The infrared spectra of the sample were measured before every commutation at every temperature. No thermally induced isomerization or degradation of the fulgimide was measurable for the fulgimide monolayer in the different photo-stationary states on times scales in the order of one hour.

The switching kinetics are shown in figure 4.2 for different temperatures. The cross section is determined using the linear regression as explained in chapter 3.3.2. The left and right panel display the ring opening and closing reaction under green and UV light, respectively. The green curve corresponds to the photo isomerization at room temperature, the red curve to 76°C. The main observation is a temperature dependence for the ring opening reaction (left panel), whereas the ring closure reaction is not sensitive to the temperature changes.

The cross sections are listed in table 4.1 for the different measured temperatures T_{Si} . We checked that the effect is a real temperature effect by

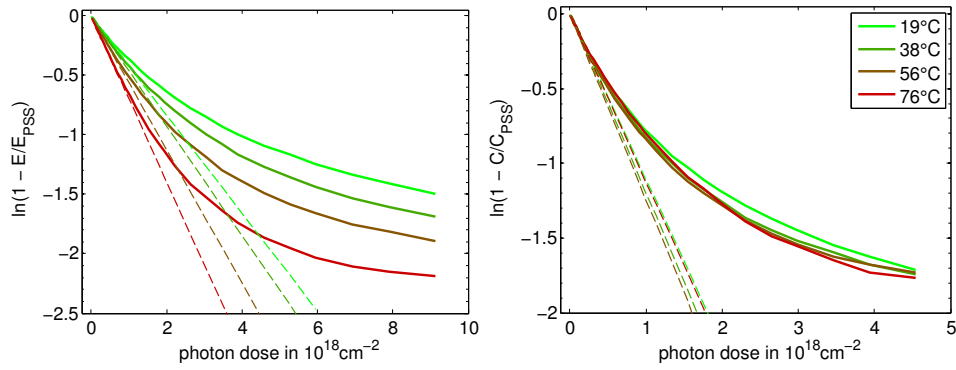


FIGURE 4.2: Thermal influence on the photo switching of fulgimide monolayers

repeating the photo commutation after the isomerizations at higher temperatures again at room temperature. At room temperature same cross sections have been measured as before. Note that T_{Si} is measured in the dark. The sample temperature increases under light illumination by ca. 1°C as explained in C.5

reaction	T_{Si} in $^\circ\text{C}$	σ in 10^{-18} cm^{-2}
1. C \rightarrow E (green)	19	0.41
2. E \rightarrow C (UV)	19	1.11
3. C \rightarrow E (green)	38	0.46
4. E \rightarrow C (UV)	38	1.20
5. C \rightarrow E (green)	56	0.60
6. E \rightarrow C (UV)	56	1.24
7. C \rightarrow E (green)	76	0.70
8. E \rightarrow C (UV)	76	1.12
9. C \rightarrow E (green)	19	0.40
10. E \rightarrow C (UV)	19	1.30

TABLE 4.1: Cross sections and temperatures for the different isomerizations.

In figure 4.3 the cross sections are displayed in an Arrhenius plot for the ring opening reaction (left panel) and the ring closing reaction (right panel). For the ring opening reaction a linear dependence of $\ln(\sigma(T)/\sigma_{T_{room}})$ against the thermal energy is visible. Consequently σ can be expressed by:

$$\sigma_{C \rightarrow E}(T) = \sigma_{C \rightarrow E,0} \cdot \exp\left(-\frac{E_{act}}{k_B T_{Si}}\right) \quad (4.1)$$

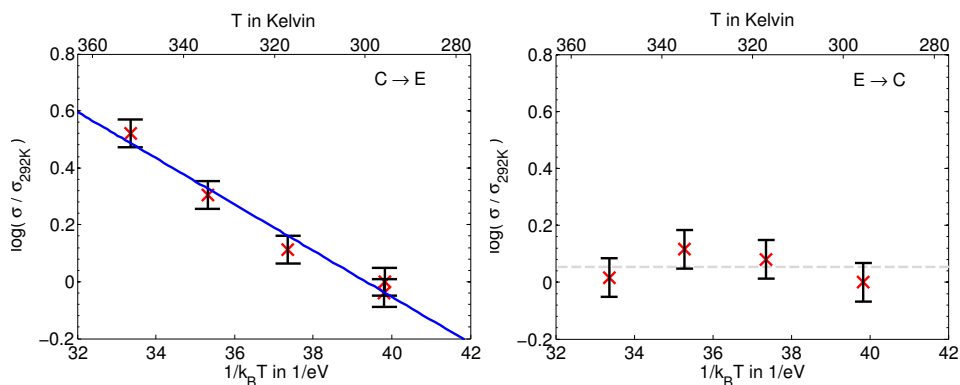


FIGURE 4.3: Arrhenius plot of the initial cross sections for the ring opening and closing reaction. The ring opening reaction is thermally activated with an activation energy of $E_{act} = 81$ meV, for the ring closing reaction under UV light no temperature dependence is observed.

The cross section is thermally activated via the thermal activation of the quantum efficiency [76, 77]. The activation energy $E_{act} = 81$ meV and cross section $\sigma_{C \rightarrow E,0} = 1.0 \cdot 10^{-17}$ cm² are determined from the Arrhenius plot in figure 4.3. The activation energy is thereby within the limits of 0.056 eV to 0.202 eV that has been measured before for different fulgimide [45, 48, 75, 76]. For the ring closing reaction no tendency of the cross sections is observable for the different temperatures.

In figure 4.4 the numerical cross section is plotted for different temperatures as a function of the photon dose. In the left panel (ring opening reaction) the numerical cross sections increase with sample temperature. The numerical cross section of the ring close are independent of temperature.

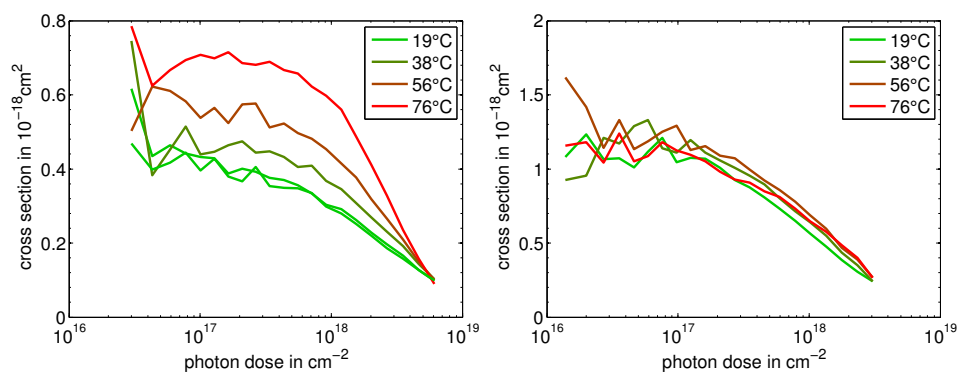


FIGURE 4.4: Numerical cross sections as a function of the photon dose for the ring opening (left) and ring closing (right) reaction at different temperatures.

The fact that these plots do not overlay on a single plot by multiplying

them with a scaling factor suggests that the E_{act} vary along the photo commutation. This is best shown in figure 4.5 where the same data of 4.4 are replotted as a function of switched isomers during the photo commutation. Plotting the $\sigma(E)$ vs. $1/k_B T$ yield $E_{act}(E)$. The variations of $E_{act}(E)$ along the photo commutation are shown against the right y-axis. The activation energy significantly increases from 0.08 eV to over 0.20 eV close to the PSS. The right panel of the figure shows several Arrhenius plots for the determination of the $E_{act}(E)$ after 20%, 40% and 60% of the commutation.

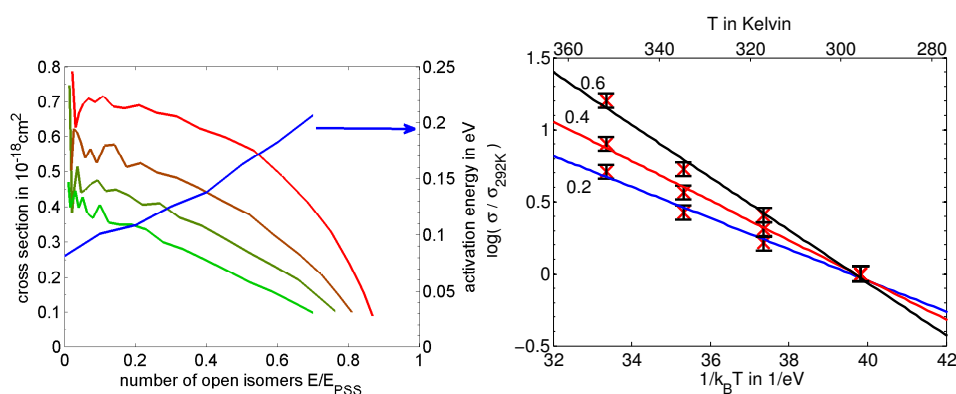


FIGURE 4.5: Numerical cross sections for increasing temperatures (green to red) and the resulting activation energy (blue)

This behavior strongly suggests that the E_{act} depends on the local molecular environment. E_{act} equals 80 meV when C is surrounded by C isomers (initial state) and increases to 200 meV for C surrounded by open E isomers.

The cross section dependence of the temperature must therefore be rewritten as a function of the number of switched isomers E :

$$\sigma_{C \rightarrow E}(T, E) = \sigma_{C \rightarrow E,0} \cdot \exp\left(-\frac{E_{act}(E)}{k_B T}\right) \quad (4.2)$$

The activation energy $E_{act}(E)$ is the effective activation energy of the whole isomerization process and not the activation energy of the single reaction rates shown in 4.1.

The absence of any thermal activation of the ring closing is due to the

absence on a meta-stable intermediate state including thermal barriers during the ring closing reaction (see 4.1).

4.3 Monte Carlo simulations of the photo-switching of fulgimide on surfaces

4.3.1 Reaction mechanism for the ring opening reaction

The ring opening reaction mechanism under visible light has been studied by the Zinth group and is explained in the introduction of the second chapter. The reaction mechanism proposed by Nenov et al. [74] is displayed in figure 4.6 including the different states and their energy potentials and the different reaction paths with their corresponding activation energies like Draxler et al. [46]. For a clearer view the different states and reaction paths are repeated in the right panel.

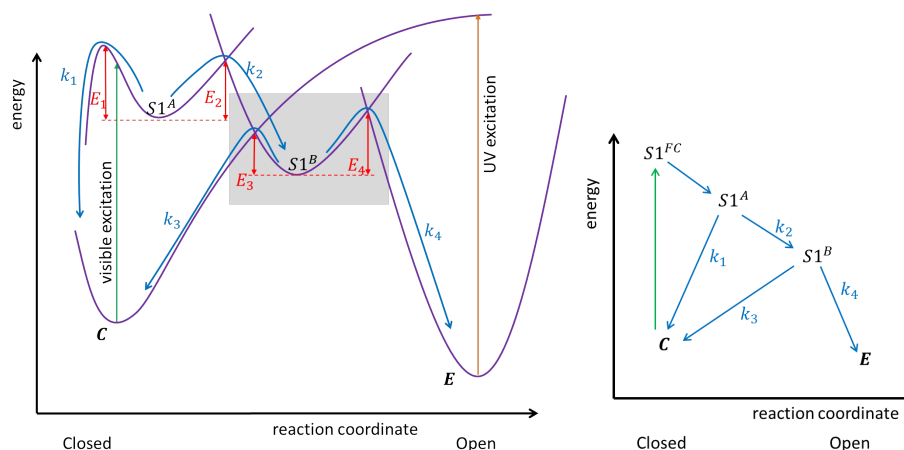


FIGURE 4.6: Reaction mechanism including the different reaction paths for the ring opening reaction.

For a successful isomerization after the excitation with visible light, the isomer in the $S1^A$ state first has to take the k_2 path to reach $S1^B$ and subsequently the k_4 path to reach the open form. After taking the path k_1 or k_3 the molecules relaxes back to the closed form. The reaction rates k_i are thermally activated with the activation energy E_i :

$$k_i = A_i \cdot \exp\left(-\frac{E_i}{k_B T}\right) \quad \text{with } i = \{1, 2, 3, 4\} \quad (4.3)$$

It has been shown in solution that the activation energy and therefore quantum efficiency of the ring opening isomerization strongly depend on

the environment of the isomer [73, 76]. In solution the environment is defined by the solvent resulting in isomer-solvent the van der Waals interaction. On surfaces the environment of the isomer depends on the isomers in vicinity, e.g. via steric effects and in particular van-der-Waals-interactions with neighboring isomers. The van der Waals interactions of polar C isomer and less polar E or Z isomers is expected to be different.

The change of $E_{act}(E)$ on surfaces is consequently interpreted as the change of the local environment during the commutation because polar C isomers are isomerized to less polar E isomers. Figure 4.7 shows a zoom to the intermediate state for two different environments. A change of the energy intermediate state due to interactions with different environments results in different activation energies.

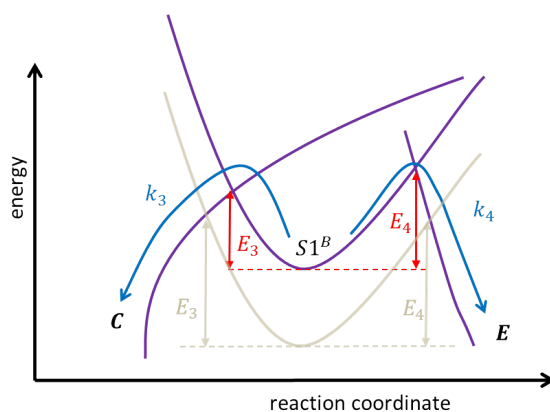


FIGURE 4.7: Different activation energies E_3 and E_4 in different environments.

E and C fulgimide attached on a surface are shown in figure 4.8 [55]. Besides the different polarities the isomers are differently aligned and therefore influence their neighbors in different ways. On silicon surfaces every isomer has 6 nearest neighbors. The isomeric state of the neighbors and therefore the activation energy depends on the advancement of the commutation of the photochromic monolayer.

To keep the model as simple as possible the we assume that only the for the second branching the reaction rates k_3 and k_4 depend on the environment via their activation energies of E_3 and E_4 as shown in 4.7. The activation energies of E_3 and E_4 with m nearest neighbors in the E form

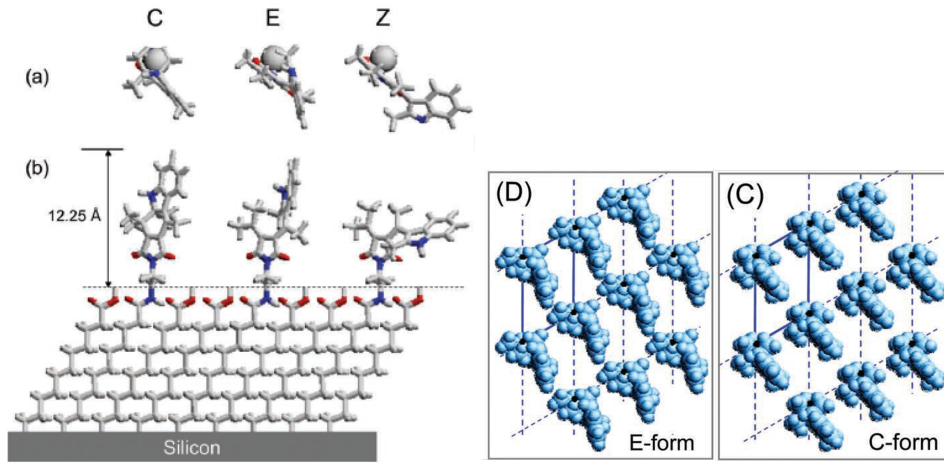


FIGURE 4.8: Top- and sideview of C, E and Z fulgimide coupled via an amino linker to the silicon surface (left panel). Atomic structure of a pure E and C fulgimide monolayer. Image taken from [55].

and l missing neighbors for dilute surfaces can be written as:

$$\begin{aligned}
 E_3 &= E_{3,C} + m\delta_{3,E} + l\delta_{3,free} \\
 E_4 &= E_{4,C} + m\delta_{4,E} + l\delta_{4,free} \quad m, l = 0 \text{ to } 6, m + l \leq 6
 \end{aligned}
 \tag{4.4}$$

where $E_{i,C}$ is the energy barrier if the isomer is surrounded by 6 C isomers, $\delta_{i,E}$ and $\delta_{i,free}$ are the energy corrections if one neighboring site is occupied by an open isomer or empty (case of diluted monolayers), respectively. Due to the hexagonal structure of the substrate it is again assumed that the highest experimental obtained fulgimide density is $1.8 \cdot 10^{14} \text{ cm}^{-2}$ corresponds to a hexagonal packing. For the comparison of simulation and experiment a simulated dense monolayer without missing neighbors therefore corresponds to an experimental density of $1.8 \cdot 10^{14} \text{ cm}^{-2}$.

The probability that the reaction path k_2 and k_4 is taken is η_1 and η_2 , respectively, one can express the quantum efficiency η for the whole

ring opening isomerization by:

$$\eta(T) = \eta_1(T) \cdot \eta_2(T, l, m) \quad (4.5)$$

$$\eta(T) = \eta_1(T) \cdot \frac{k_4}{k_4 + k_3} \quad (4.6)$$

$$\eta(T) = \eta_1(T) \cdot \frac{1}{1 + \frac{A_3}{A_4} \exp\left(\frac{E_4(l, m) - E_3(l, m)}{k_B T}\right)} \quad (4.7)$$

$$\eta(T) = \eta_1(T) \cdot \frac{1}{1 + \frac{A_3}{A_4} \exp\left(\frac{\Delta E + m \cdot \epsilon_E + l \cdot \epsilon_{free}}{k_B T}\right)} \quad (4.8)$$

using the energy barrier difference $\Delta E = E_{4,C} - E_{3,C}$ and the difference of the environmental influence on the barriers $\epsilon_E = \delta_{4,E} - \delta_{3,E}$ and $\epsilon_{free} = \delta_{4,free} - \delta_{3,free}$. Only the difference of the energy barriers is important, therefore our model considering an environment dependence of E_3 and E_4 is equivalent to the assuming that either E_3 or E_4 would not be affected by the environment.

4.3.2 Methodology

The isomerization cross section of a single isomer can thereby be written in terms the absorption cross section σ_{abs} and the quantum efficiency $\eta(T)$:

$$\sigma = \sigma_{abs} \eta(T) \quad (4.9)$$

$$\sigma = \sigma_{abs} \eta_1(T) \cdot \frac{1}{1 + \frac{A_3}{A_4} \exp\left(\frac{\Delta E + m \cdot \epsilon_E + l \cdot \epsilon_{free}}{k_B T}\right)} \quad (4.10)$$

$$\sigma = \sigma_0(T) \cdot \frac{1}{1 + \frac{A_3}{A_4} \exp\left(\frac{\Delta E + m \cdot \epsilon_E + l \cdot \epsilon_{free}}{k_B T}\right)} \quad (4.11)$$

The cross section of a single isomer depends of two parts, a proportionality factor $\sigma_{abs} \eta_1(T)$ and $\eta_2(T, l, m)$ that depends on the local environment. The factor $\eta_2(T, l, m)$ between 0 and 1 represents the evolution of the cross section during the isomerization.

The photo isomerization of a monolayer of $k \times k$ C isomers is simulated (at least $k > 200$). For the calculation of the number of neighbors periodic boundary conditions are used. The Monte Carlo simulation repeats at least $5k^2$ times the following steps:

1. a random choice of an isomer that absorbs a photon
2. if the isomer is in the closed C form the isomer reaches the state $S1^{sb}$, otherwise the first step is repeated
3. the excited C isomer switches to the open form with the probability η_2 of the single fulgimide: $\eta_2 = \frac{1}{1 + \frac{A_3}{A_4} \exp\left(\frac{\Delta E + m \cdot \epsilon_E + l \cdot \epsilon_{free}}{k_B T}\right)}$ that depends on the number of nearest neighbors m in the open form and the number of missing neighbors l

Thereby the nearest neighbor interactions are considered because the efficiency η_2 of every single molecule depends vicinity of the isomer. The Monte Carlo simulation can not consider the probability that a closed C isomer absorbs a photon σ_{abs} nor the probability $\eta_1(T)$ of isomerization to the state $S1^{sb}$. σ_{abs} and $\eta_1(T)$ remain multiplicative factors that do not change during the commutation and therefore can be ignored.

The efficiency of the second branching η_2 depends on three free parameters: $\frac{A_3}{A_4}$, ΔE , ϵ_E and ϵ_{free} . Optimization of these three parameters with the aim of matching the Monte Carlo simulations to the experiments is difficult because of the intrinsic variations of the Monte Carlo simulations. The two parameter sets that are finally used for the Monte Carlo simulation are displayed in table 4.2. The parameters $\frac{A_3}{A_4}$ and ΔE are strongly correlated, a greater $\frac{A_3}{A_4}$ can be compensated by a smaller ΔE . For temperature independent experiments both parameters merge to only one degree of freedom.

$\eta_2 = \frac{1}{1 + \frac{A_3}{A_4} \exp\left(\frac{\Delta E + m \cdot \epsilon_E + l \cdot \epsilon_{free}}{k_B T}\right)}$				
parameter set	A_3/A_4	ΔE	ϵ_E	ϵ_{free}
	in 10^{-16}	in eV	in eV	in eV
1	1.39	0.565	0.096	0.042
2	1.39	0.546	0.077	-

TABLE 4.2: Monte Carlo simulation parameters

The simulated number of switched isomers versus the simulated photon dose is shown in figure 4.9 for a dense pure C monolayer. In the simulations, it is assumed for convenience that each photon is absorbed to speed

up the test ($\sigma_{abs}\eta_1 = 1$). To represent the experiment a scaling factor could be introduced to match with experimental photon dose to commute the layer. As in the experiment the number of switched isomers increases due to the photons.

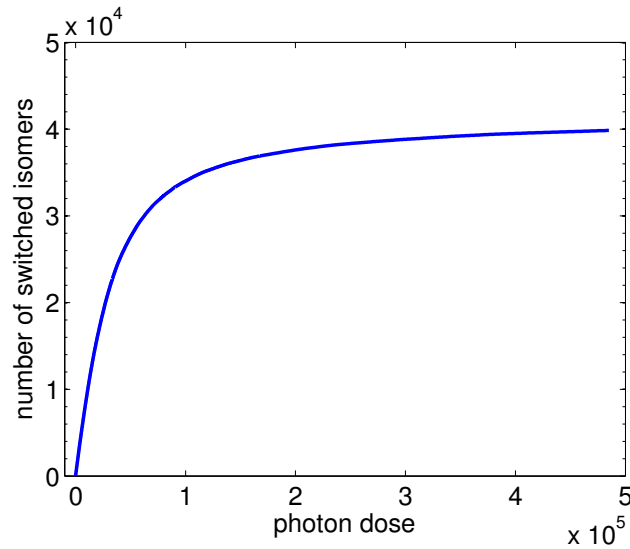


FIGURE 4.9: Simulated number of switched isomers versus the photon dose for a dense monolayer with the first parameter set

In simulations theoretically all isomers are switchable because the nearest neighbor interaction can not decrease the switching probability to zero although 6 nearest neighbors may be in the open form. To remain consistent with experiments where photo-commutation is not completed due to finite time, the PSS are estimated in as in true experiments. After the simulation is stopped the PSS is estimated by the derivative plot in figure 4.10 using a pseudo Voigt function as in the experiments.

As in solution the numerical effective cross section is calculated in the right panel for the corresponding simulation.

Due to the missing proportionality factor $\sigma_{abs}\eta_1$ the only the efficient cross section due to the change of η_2 is considered. The efficient cross section σ_{eff} is calculated numerically as before in the experiments.

$$\text{simulation: } \quad \sigma_{abs}\eta_1(T) \rightarrow 1 \quad \Longrightarrow \quad \sigma_{num} \rightarrow \sigma_{eff} \quad (4.12)$$

The photo commutation is simulated for different surfaces. Dilute

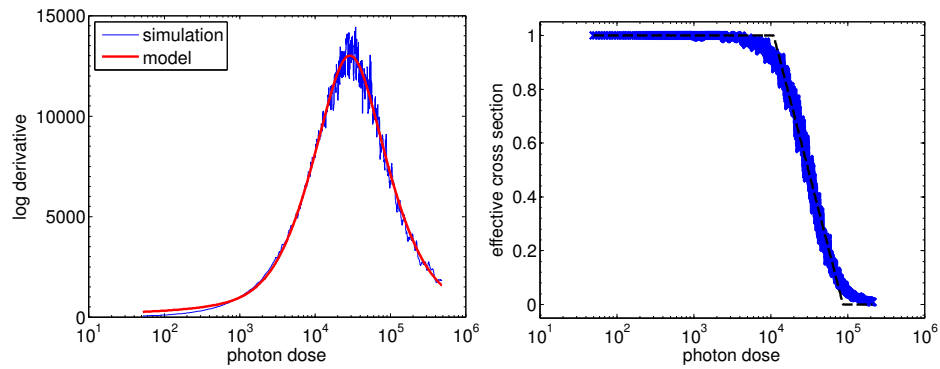


FIGURE 4.10: Estimation of the Photo stationary state for the Monte Carlo simulation. The log derivative of the number of switched isomers is shown against the number of photons that corresponds to the number of iterations of the simulation loop

monolayers are simulated by a mesh of randomly distributed C isomers with empty (free) spots that result in different surface densities. Furthermore random distributions of C and E isomers are used as initial surface to simulate different isomeric compositions at the beginning of the commutation. Non-switchable isomers due to photo degradation are ignored.

4.3.3 Results of the Monte Carlo simulation

In figure 4.11 the effective cross sections of the pure C monolayers for different densities versus the number of switched isomers is shown for the first parameter set. The red curve corresponds to the densest monolayers, the most dilute one is green. For all surface densities the effective cross section is first constant and then decreases along the photo commutation process. All plots overlap up to 30% dilution. More diluted monolayers present a slower decrease of σ . The former observation agrees well with experiment. Unfortunately, the behavior for ML below 30% cannot be checked experimentally due to lack of sensitivity of FTIR.

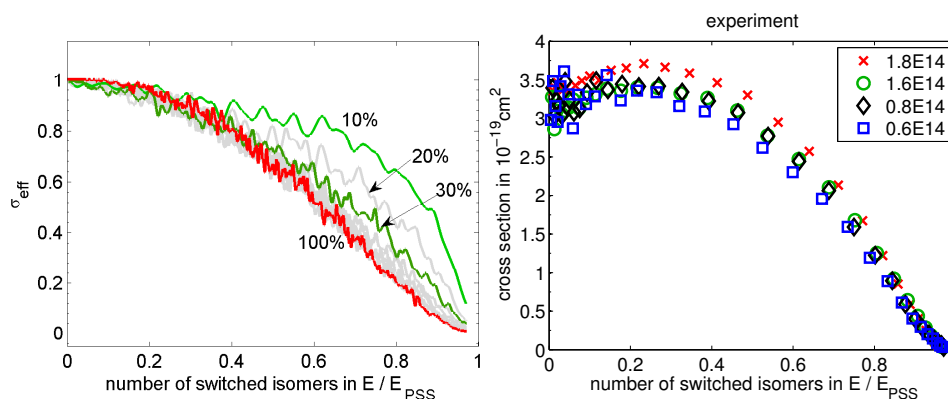


FIGURE 4.11: Simulated (left) and experimental (right) cross sections for the photo commutation of different surface densities.

The isomeric composition at the estimated photo stationary states are illustrated in the histogram 4.12. For dilute monolayer nearly all isomers switch from the closed to the open form. For increasing surface densities the number of non switched isomers that remain in the C form increases.

For the isomeric composition at the photo stationary states the simulation and the experiments show the same tendency of a lower fraction of switched isomers with an increasing photochromic density. Nevertheless, the Monte Carlo simulations using the parameter set 1 overestimates the number of C isomers at the visible PSS.

The switching kinetics and PSS for dilute monolayers strongly depend

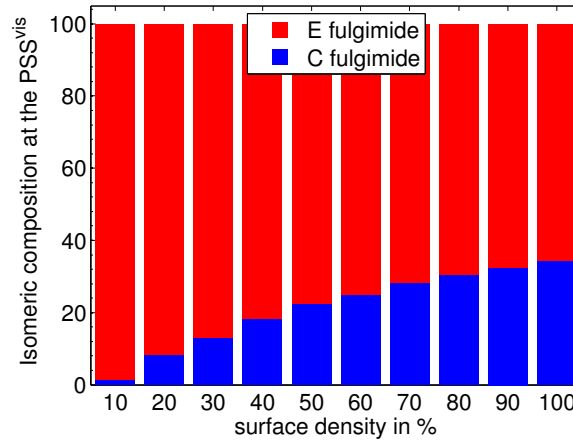


FIGURE 4.12: Isomeric composition at the simulated photo stationary state for different densities

on ϵ_{free} . In the annex C.8 the influence of different values for ϵ_{free} are displayed. The same systems are simulated with a smaller energy barrier difference ΔE and ϵ_E (parameter set 2). The results are shown in the annex C.9. The lower ΔE and ϵ_E shows similar switching kinetics. The number of remaining C isomers in the visible PSS is lower.

For the comparison of the simulation and experiment of the photo commutation at different temperature the cross sections $\sigma(E = 0, T)$ are extrapolated by the evolution of the simulated cross sections to compare simulations to experiments:

$$\sigma(E, T) = \sigma(E = 0, T) \cdot \frac{\sigma_{eff}(E, T)}{\sigma_{eff}(E = 0, T)} \quad (4.13)$$

Thereby the cross sections for different temperatures are shown in figure 4.13. The black squares, diamonds, crosses and circles are the experimentally measured numerical cross section for the increasing temperatures. The simulated effective cross sections at different temperatures are scaled by the experimentally measured σ and therefore the curves do not only contain information of the simulation. The cross sections for all temperature decrease. The non homothetic decrease is well predicted by the simulations. For the cross sections corresponding to the high temperature the decrease is more abrupt than for the low temperatures. Only very small systematical differences are present close to the PSS.

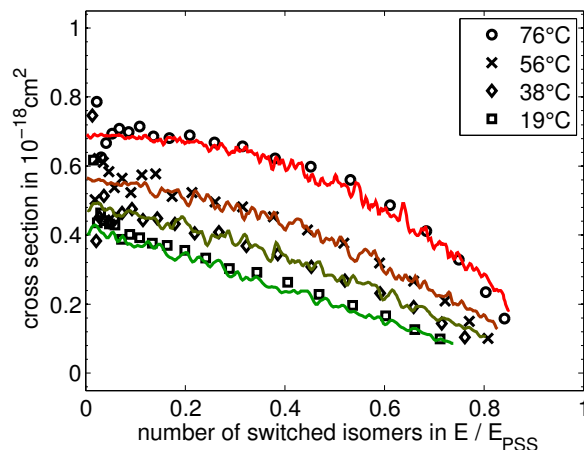


FIGURE 4.13: Cross sections for the ring opening reaction of fulgimide monolayers using the Monte Carlo simulation (dashed line) and experiments at different temperatures

The influence of different isomeric compositions at the beginning of the isomerization of dense monolayers is examined experimentally and by Monte Carlo simulations. The simulated effective and measured numerical cross sections are displayed in the left and right panel of figure 4.14 against the isomeric composition, respectively. The different initial isomeric compositions in the simulation and the experiment result in similar curves that are shifted with respect to each other. Both experiments and simulations show the same behavior. All the curves show the same decreasing tendency and do not crucially depend on the initial isomeric composition. In the simulations a small decrease of σ_{eff} is measured when less molecules are switchable that has not been measured on surfaces.

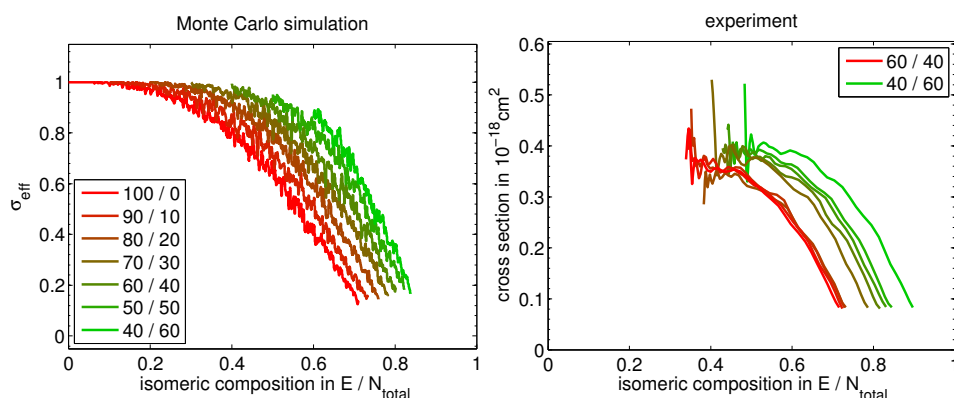


FIGURE 4.14: Simulated cross sections of the switching kinetics for isomerizations starting from different initial isomeric compositions ranging from a pure C (red) until a mixed 60%C/40%E (green) monolayer

The Monte Carlo simulation of the ring opening reactions depending on nearest neighbor interactions enables to qualitatively explain the following experimental observation:

1. similar decreasing cross sections during the commutations for different densities
2. a smaller fraction of switched isomers for dense monolayers than for dilute
3. the temperature dependence of the decreasing cross section
4. different σ despite the same isomeric composition for commutations with different isomeric compositions at the beginning of the switch

4.4 Conclusions

The temperature dependent photo isomerization show an increasing cross sections for the ring opening reaction of fulgimide monolayer for higher temperatures. For the ring closing reaction no temperature dependence is measured. The increase of the cross section can be motivated by an Arrhenius law whose activation energy increases during the commutation of the monolayer.

A theoretical model for the ring opening reaction is extended to account for nearest neighbor interactions on surfaces. Monte Carlo simulations can simulate the photo isomerization of different monolayers.

The effective cross section of the simulations shows that no first order kinetics are present but an decreasing cross section. Surfaces with different photochromic densities show similar kinetic behavior as in the experiment but different photo-stationary states. The cross sections show a different decreasing behavior for different temperatures. Simulations with diverse initial surface compositions show similar cross sections. Despite same global isomeric compositions different cross sections are obtained for commutation with different initial isomeric compositions.

Thereby the experimental observation of these phenomena can be explained by the simulations. This shows the crucial importance of the nearest neighbor interactions on the photo commutation kinetics.

Chapter 5

Influence of Gold Nanoparticles on the Photo Commutation of Fulgimide Monolayer on Silicon Surfaces

5.1 Introduction

The exploration of optical properties of nanoparticles has a long history. Already Roman artisans implemented gold and silver nanoparticles in the Lycurgus cup to benefit from different optical reflection and absorbance properties. Nowadays gold nanoparticles find numerous applications in catalysis, medicine, biotechnology, microelectronics etc. [125–131]. Besides various fabrication methods the preparation following Turkevich is particular famous due to its simplicity [132]. Nevertheless, many other methods are available [133–135].

Electrons in metal nanoparticles can be excited by incident light. When the free electron path is longer than diameter of the nanoparticle no bulk scattering is expected and the main photon-electrons interaction is close to the surface. If the nanoparticle is smaller than the wavelength of the light, resonant oscillation of the free electron gas can be imposed. This resonant oscillation is called surface plasmon resonance (SPR). The frequency of the surface plasmon depends on the size and shape of the nanoparticle and on its dielectric environment. In particular the presence of solid surfaces or

aggregation of other nanoparticles influence the plasmon. The electronic oscillations increase the local electric field [136, 137].

This effect is exploited by surface enhanced Raman spectroscopy (SERS) and surface enhanced infrared absorbance (SEIRA) to increase the measurement sensitivity. The sensitivity enhancement depends on the nanoparticle density. In particular at the percolation threshold the sensitivity is increased and enhancement factors can reach several orders of magnitude [138–140].

The coupling of optical properties of gold or other noble metal nanoparticles with photochromic compounds is an emerging research topic. In the same way as for the absorption of photochromic compounds on substrates, the photochromism may be affected by quenching of the excited states of the photochromes due to electronic interactions [27, 37, 38, 141] with the metallic nanoparticle. As on surfaces the coupling can be decreased by a linker between the photochromic group and the molecule. The quantum yields for photo-isomerization are influenced by the length of the linker because of the distance-dependent quenching with the metal [97, 142]. The direct electronic coupling of the aromatic ring of azobenzene and gold nanoparticles increases the thermal barrier and thereby the lifetime of the cis isomer [27]. However, electronic coupling between nanoparticle and photochromes is desirable for some application and a compromise may be necessary. Coupling of Diarylethene on top of nanoparticles selectively suppressed the ring closure reaction while conserving the ring opening reaction [143]. This quenching can be explained using DFT by electronic interactions of the gold with the Diarylethene that strongly influence the light absorbance [144].

On the other hand, the properties of the nanoparticles can be influenced by electronically coupled photochromes. Electronic transitions of functionalized silver nanoparticles are for example shifted by chemically bonding of an azobenzene [28]. The optical or dielectric properties like the reflective index of the nanoparticles can be coupled to the photochromes and thereby be influenced by the isomerization of the latter [31, 145]. The surface plasmonic resonance of the nanoparticles is in the visible region. The isomeric

composition of monolayers on gold nanorods influences surface plasmonic resonance [146]. Furthermore, the aggregation of nanoparticle can be controlled by the diverse attractive or repulsive interaction of two isomers that are attached different nanoparticles [147].

The influence of the nanoparticle on the switching kinetics on the photochromes has been studied before in the literature. In most systems colloidal suspensions of nanoparticle are functionalized by photochromes via ligand exchange and therefore electronic interactions of photochromes and nanoparticles are present. Diverse results pointing in different directions have been obtained since many different systems including different electronic couplings are investigated. For example the ring closing reaction of DAE attached to nanoparticles does not follow first order kinetics as in solution but a slower non exponential behavior is observed [148]. Other studies of azobenzene monolayer on top of gold nanoparticles could not observe any difference of the first order reaction kinetics between the free and coupled azobenzene [149]. On the other hand, other studies determined an increased photochromism when the excited light couples with the visible plasmon [26, 28]. The amplification of the switching kinetics is wavelength dependent [150]. The faster kinetics does not account for all isomers and is therefore non homogeneous. This is attributed to the non homogeneous electric field effects of the gold nanoparticles [151].

In the mentioned studies photochromes are absorbed on nanoparticles or attached via ligand exchange. Thereby not only the dielectric environment of the photochrome is changed but furthermore energy and electron transfer between the nanoparticle and the photochromes is present. Consequently comparative studies of the kinetics are not able to distinguish both effects.

In this work the environmental influence of the gold nanoparticle on the switching kinetics of fulgimide is investigated. To do so the photochromes are not directly bonded or absorbed by the nanoparticles to minimize electron or energy transfer. Fulgimide monolayers are prepared as explained before and a submonolayer of gold is added on top of the surface.

In submonolayers of ligand-terminated gold nanoparticles on top of photochromes the average distance of photochromes to the gold nanoparticle is several nanometers. Thereby the plasmonic effect on the switching kinetics dominates possible energetic and electronic transfers between the nanoparticles and photochromes. The purpose of this chapter is the investigation of photo switching properties of fulgimide monolayer in the presence of gold nanoparticles and comparison to blank fulgimide monolayer without nanoparticles.

5.2 Preparation and characterization of gold nanoparticles monolayers

5.2.1 Gold nanoparticles synthesis and characterization

The gold nanoparticles (AuNP) have been prepared following the protocol of Schulz et al. [152]. The protocol is based on the Turkevich method while additionally controlling the pH using a citrate buffer. The citrate buffer to stabilize the pH consists of 75/25 Trisodium citrate and citric acid in a concentration of 2.75 mM. For the preparation of the AuNP, 160 ml of the citrate buffer is heated to 100°C while being stirred using a magnetic stirrer. At the same time 40 ml of precursor solution ($\text{HAuCl}_4 \cdot 3\text{H}_2\text{O}$) in MilliQ water is heated to its boiling point. Then the precursor solution is added to the boiling citrate buffer and the resulting solution is kept at 100°C for at least 20 minutes while being continuously stirred. The average size of the AuNP should be around 12 nm which yields a concentration of approximately 1.5 nM of AuNP.

The UV visible spectrum of the AuNP is shown in figure 5.1. The characteristic visible absorption peak is located at 520 nm.

The size distribution is measured by dynamic light scattering¹. Thereby the size distribution can be determined to be (12 ± 3) nm. For the determination of the mean value and variance the particles with a diameter of

¹Zetasizer Nano ZS, Malvern Instruments

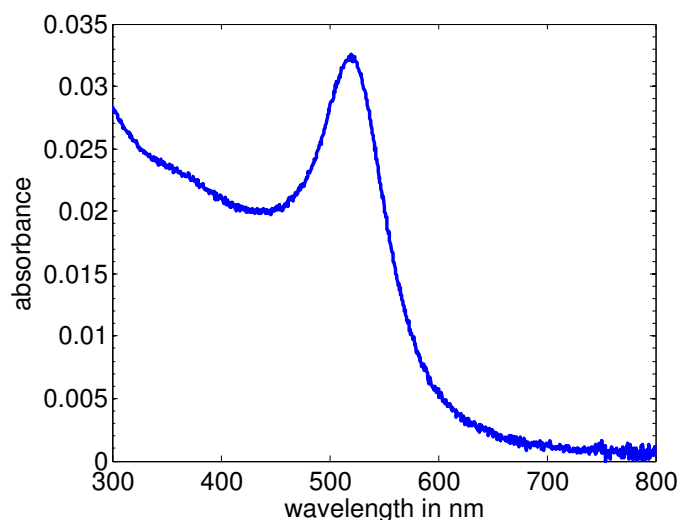


FIGURE 5.1: UV visible spectrum of the AuNP prepared by the protocol of Schulz [152].

more than 200 nm have not been considered. These probably correspond to aggregates of particles, impurities or artifacts.

Furthermore, the size distribution of the AuNP can be estimated by scanning electron microscopy (SEM). Therefore, the solution of the AuNP is first dried on a surface that then imaged by scanning electron microscopy. The size distribution has been determined using ImageJ². To do so the SEM-images are converted to binary files and the particles are measured automatically at different spots. The resulting size distribution is shown in the panel of figure 5.2. The mean particle size is determined to be (12.7 ± 0.9) nm for the size distribution shown in the figure. Different data treatment in ImageJ influences the result and thereby there is an additional systematical error on the particle size of about 1 nm. The diameter of the used nanoparticles is therefore about (13 ± 2) nm. A dense monolayer of nanoparticles with a diameter of 13 nm corresponds to a surface density of $6.8 \cdot 10^{11} \text{ cm}^{-2}$.

5.2.2 Surface preparation and characterization

Several approaches have been used to prepare AuNP monolayer on top of the fulgimide substrate. Homogeneous (sub-) monolayers of gold nanoparticles can for example be prepared by deposition of a thin gold layer and

²ImageJ version 1.48v

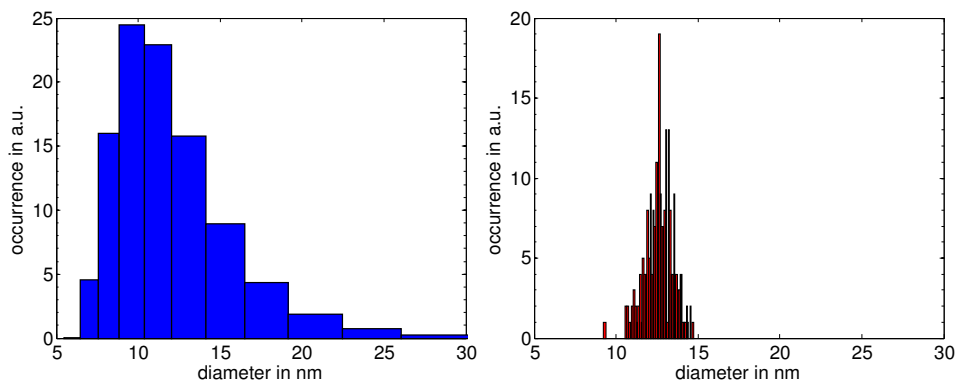


FIGURE 5.2: Size distribution of AuNP measured by dynamic light scattering and by scanning electron microscopy.

subsequent post annealing to at least 300°C [153]. But the organic monolayer is thermally only stable up to 250°C [154, 155], not to mention the organic photochromes. Spin coating failed because of the hydrophobicity of the fulgimide monolayer (contact angle of 65°). Repeated spotting³ of 10 μl of the AuNP solution failed due to segregation and its low concentration. Langmuir–Blodgett deposition of Janus AuNP trapped with hydrophilic and hydrophobic ligands at a toluene and water interface only showed in-homogeneous coverage [156–158].

The most satisfying results have been obtained by solvent evaporation of an AuNP droplet that covered the whole surface. To do so 400 μl of the solution containing AuNP has been dried on the surface. Assuming a AuNP concentration of 1.5 nM this should correspond to around 1.7 monolayer. However, scanning electron microscopy (SEM) images show that the surface is completely covered by Trisodium citrate and/or citric acid and not only AuNP. Therefore after the drying of a AuNP droplet the surface has been rinsed in Milli Q water for around 30 seconds to remove organic material. Several SEM images are taken to control the gold monolayer at the center and border of the sample.

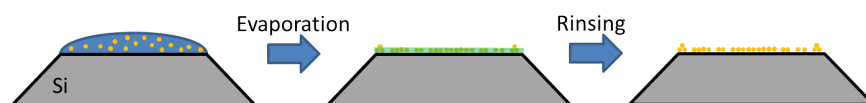


FIGURE 5.3: Preparation cycle for gold nanoparticle monolayer

³Biorobotics, Microgrip II compact

The obtained surface is shown in the panel of figure 5.4. The additional Trisodium citrate and citric acid disappeared and only the nanoparticles remain. Nonetheless, no dense monolayer is obtained which indicates that some nanoparticles have been washed away, too. The surface density is $1.1 \cdot 10^{11} \text{ cm}^{-2}$. Therefore, the droplet drying and rinsing have been repeated four times to increase the surface density. The right panel shows the same surface after four times repeating the drop casting procedure. The surface density increased to $3.0 \cdot 10^{11} \text{ cm}^{-2}$.

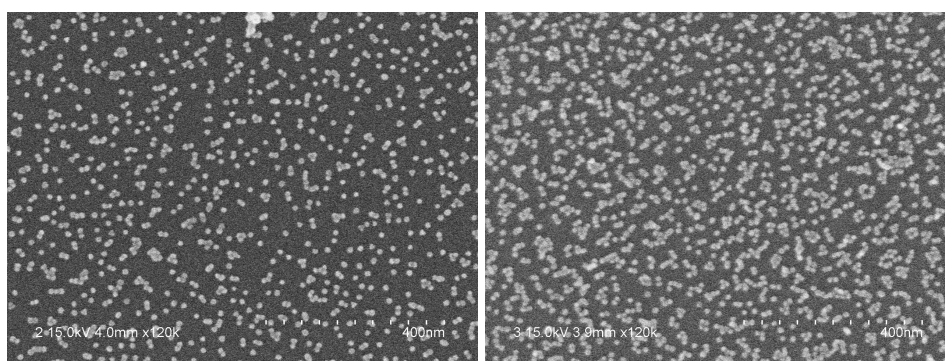


FIGURE 5.4: Submonolayer of gold nanoparticles on an organic monolayer after one (left) and four (right) cycles of drying a AuNP solution and subsequent rinsing

In figure 5.5 the surface is displayed whose photochromic properties are studied in the following. The surface density of nanoparticles is $3.1 \cdot 10^{11} \text{ cm}^{-2}$ which corresponds to the half density of a perfectly dense monolayer. Higher densities have not been achieved using this technique. However, even sub-monolayer of AuNPs may show enhancement of the electromagnetic field, if the characteristic particle distance is locally much smaller than the illumination wavelength [159].

The deposition of AuNP on surfaces by repetitive drop casting does not reveal (sub) monolayer of AuNP without defects. In the solution some AuNP may form aggregates and/or island growth on the surface leads to aggregates of nanoparticles on the monolayer (left panel in figure 5.6, blue arrows). The central white aggregates corresponds to around four layers of AuNP (left blue arrow). The white circle in the center corresponds to a locally increased coverage with a density of $4.5 \cdot 10^{11} \text{ cm}^{-2}$ (red arrow).

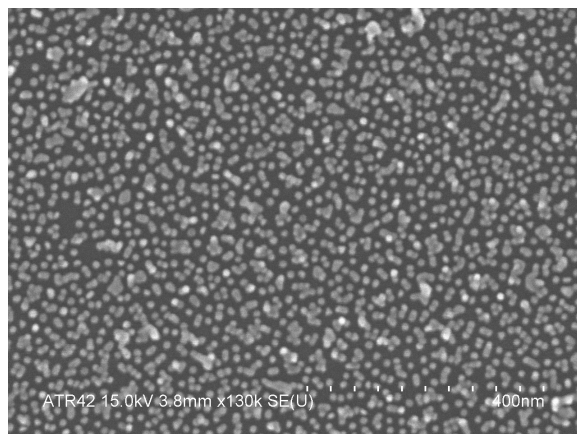


FIGURE 5.5: SEM: fulgimide monolayer covered by AuNP

The right panel in 5.6 shows the boundary of the droplet at the border of the substrate (red rectangle is image position on the silicon prism substrate). Big aggregates are formed at the border of the droplet that have a height of several AuNP. Nevertheless, this boundary of the droplet has a width of around 50 ± 10 nm which is negligible with respect to the sample width of 1.4 cm (<1%).

The large majority (>90%) of the surface is covered by a (sub) monolayer. The photo commutation is measured globally and therefore the photo switching characteristics of most molecules are determined by the sub-monolayer. The gold nanoparticle density is clearly under the percolation threshold and therefore no significant increase of the infrared sensitivity is expected [138].

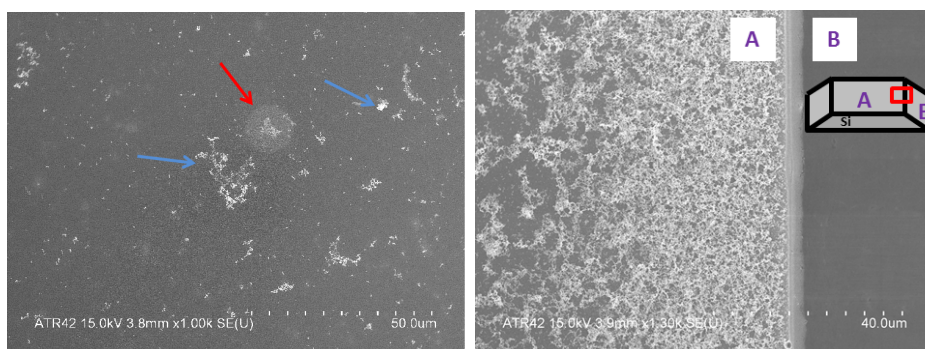


FIGURE 5.6: Left: aggregates of gold nanoparticles on the fulgimide monolayer. Right: border of the droplet at the edge of the sample

The surface plasmon characteristics are measured by UV visible absorbance spectroscopy. A layer of AuNP is added on top of a silicon dioxide surface. The absorbance of the nanoparticles is displayed in the left panel of figure 5.7. The absorbance spectrum significantly changed with respect to the single particle absorbance in 5.1. The broad absorbance peak until the infrared absorbance indicates optical coupling between the AuNPs [159].

The photo commutation is measured on silicon and therefore the AuNP plasmon on silicon is measured by UV visible reflectance spectroscopy⁴ instead of absorption spectroscopy. The reflectivity for s polarized light is shown in figure 5.7 for a bare silicon sample (red) and a silicon sample with AuNP monolayer (blue) for an incidence angle of 45°. One can clearly see the change of the reflectivity due to the surface plasmon. The plasmon on silicon measured by UV-vis reflectivity has the same shape as in the absorbance measurement on glass. The increased reflectivity can be motivated by the higher reflectivity of gold with respect to silicon. Nevertheless, meaningful simulations of the reflectivity are difficult due to the complex system of sub monolayer of nanoparticles with aggregates. There is an overlap between the visible absorption peak of the fulgimide (figure 2.3) and the surface plasmon. The fulgimide absorption peak and the plasmon resonance are shifted with respect to each other.

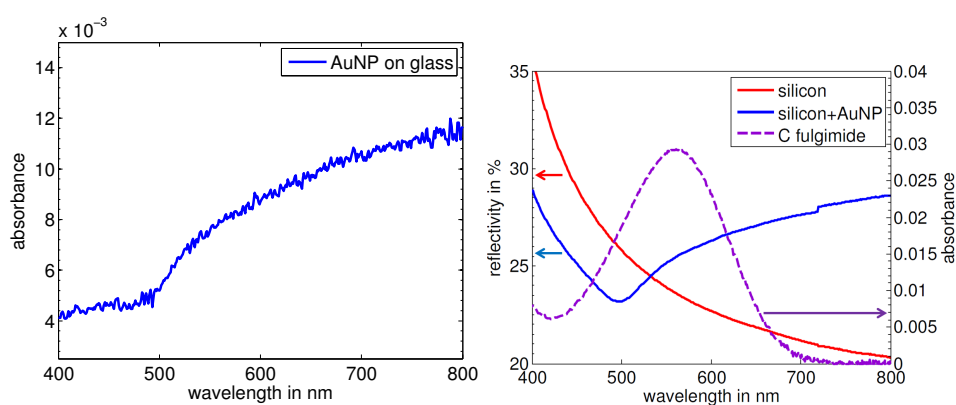


FIGURE 5.7: Surface plasmon on glass (left) and silicon (right) compared to the absorbance spectrum of C fulgimide (purple line in right panel)

⁴Agilent technologies, Carry 7000 series UV-vis spectrometer

5.3 Results

5.3.1 Infrared sensitivity

In Surface Enhanced Infra Red Absorbance (SEIRA) nanoparticles are used to increase of the infrared absorption of the molecule and thereby amplify the infrared sensitivity. In the following section the enhanced sensitivity is estimated.

In figure 5.8 different infrared spectra in p polarization are shown that enable an estimation of the gain in infrared sensitivity. The red curve shows the infrared absorbance of fulgimide and AuNP with respect to the fulgimide without AuNP. Half of the infrared beam is absorbed by the AuNP and therefore the baseline had to be corrected significantly. The infrared bands of the citrate ligands in the carbonyl region (symmetrical and anti-symmetrical COO^- stretching at 1700 cm^{-1} and 1400 cm^{-1}) and the CH_2 bands (2800 to 3000 cm^{-1}) are clearly present [160]. But in particular the characteristic peaks of the fulgimide in the carbonyl region are increased. The blue curve is the initial fulgimide absorbance using a hydrogenated silicon reference after etching. The green curve is the infrared spectrum of AuNP on freshly hydrogenated silicon using the deposition technique that is described before. The green curve shows a strong rise of the SiO_x peaks between 1000 cm^{-1} and 1250 cm^{-1} and a disappearing SiH peak that indicates strong oxidation during the aqueous treatment to obtain the AuNP monolayer. The gain in the infrared intensity can therefore be estimated by a comparison of the three infrared absorbances. More precisely the increased Fulgimide spectrum (red) should be a linear composition of the fulgimide spectrum (blue) times the increased sensitivity plus an AuNP characteristic infrared spectrum (green). Thereby the gain infrared sensitivity in the carbonyl region can be estimated to be around 1.6 ± 0.1 . The enhancement of the sensitivity has been expected to be higher since more significant amplifications are reported in the literature for comparable systems [138].

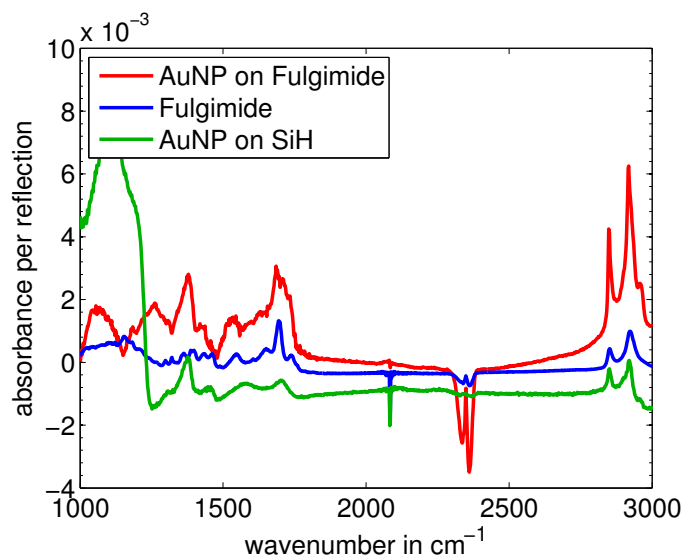


FIGURE 5.8: Increase of the infrared absorbance of fulgimide due to AuNP (red), and the infrared absorbance of fulgimide (blue) and AuNP (red) with hydrogenated silicon reference.

Until now the proportionality between the absorbance and the number of isomers has been used (Beer–Lambert law). However, this may not be valid any more because the AuNP distribution has islands of closely packed AuNP induces an inhomogeneous electric field enhancement and thus infrared absorbance. Therefore, the local enhancement factor is most probably larger than 1.6. Nevertheless, for the moment, we will assume a constant enhancement factor for all isomers.

In the following the focus will lay on the isomerization properties of the fulgimide monolayer. As seen before in 3.3.1, proportional factors like the infrared sensitivity are canceled out for the determination of the photo commutation kinetics.

5.3.2 Qualitative kinetics

The sample for the study of photocommutation by infrared spectroscopy is a silicon prism with with two principal surfaces covered by a fulgimide monolayer. To measure the influence of the AuNP on the photocommutation properties the submonolayer of AuNP has only been applied to one surface of the sample. Thereby the photo commutation with and

without AuNP can be measured on the same sample by selective irradiation of the desired surface. Both systems with and without AuNP have the same surface density, number of remaining NHS, etc. Furthermore, by applying AuNP on only one side of the sample, the absorbance of the infrared beam by the AuNP is less reduced and a better signal to noise ratio is obtained than if the AuNP would be present on both sides.

Before AuNP have been added to the surface the fulgimide have been switched several times to stabilize the photo-commutation kinetics (3.18). The change of the infrared spectrum due to the visible irradiation is shown in the panel of figure 5.9. As expected the same switching characteristics are obtained that have been measured before (e.g. 3.5). The right panel shows differential spectra of the photo commutation in the presence of the AuNP due to visible light. Similar characteristic infrared bands are observed. However, the relative intensities of the differential peak are slightly changed. This may be explained by the non proportional enhancement of the asymmetric $\nu_a\text{C=O}$ maleimide group band that results in a shoulder to higher wavenumbers. Nevertheless, the photochromism of the fulgimide monolayer is conserved in the presence of gold nanoparticles. The slight changes of the relative peak intensities of the differential absorbances cancel out in the kinetic determination and would only result in a higher uncertainty of the number of switched isomers.

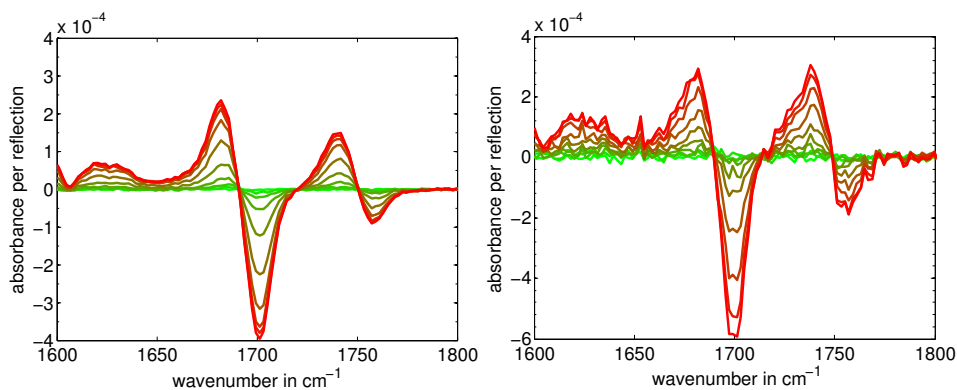


FIGURE 5.9: Differential infrared absorbance due to the photo commutation of a fulgimide monolayer without (left) and with (right) AuNP for different visible irradiation times.

The differential spectra have a higher amplitude due to the augmented

infrared sensitivity. The noise significantly increased due to the AuNP. This is the case because only one side of the sample has been switched and the infrared signal decreased by 50% due to the infrared absorption of the AuNP.

5.3.3 Kinetic parameters of the ring closing reaction

For samples without nanoparticles the isomeric composition is known due to the measured initial isomeric composition and the number of switches isomers. Furthermore the isomeric composition may be estimated by the position of the main carbonyl band. But if gold nanoparticles are added to the fulgimide monolayer the isomeric composition is unknown because the monolayer will have partly have switched due to preparation of the AuNP monolayer (ambient light, electron radiation in SEM). Estimating the isomeric composition by the carbonyl peak is not possible due to the additional AuNP infrared contributions. Accordingly the isomeric composition can not be discussed. The focus will only lay on the switching kinetics.

Although the absolute isomeric composition of the photochromes is not known, the number of switched isomers can be determined because the differential infrared spectra still have the same switching characteristics and the gain in sensitivity due to the AuNP is determined. It is ensured that for each commutation shown in the following the number of switched isomers is higher than $0.6 \cdot 10^{14} \text{ cm}^{-2}$ that correspond to 38% of the total isomers of the surface ($1.6 \cdot 10^{14} \text{ cm}^{-2}$).

The influence of the gold nanoparticles on the ring closing isomerization under UV light is examined. The kinetic curves of a fulgimide monolayer with and without an additional monolayer of AuNP are shown in the left panel of figure of 5.10 for non-polarized light. For easier comparison the kinetic is represented by the number of switched isomers with respect to the total number of switched isomers at the PSS^{UV} : C / C_{PSS} . The reference measurement of the ring closing commutation of the same sample without AuNP is represented in blue, the switch with AuNP in red. The kinetic curve of the two measurements overlap for the first half of the commutation until about $6 \cdot 10^{17}$ photons per cm^2 . For long illumination times the photo

commutation of the fulgimide with the AuNP shows a slower commutation with respect to the reference without any AuNP.

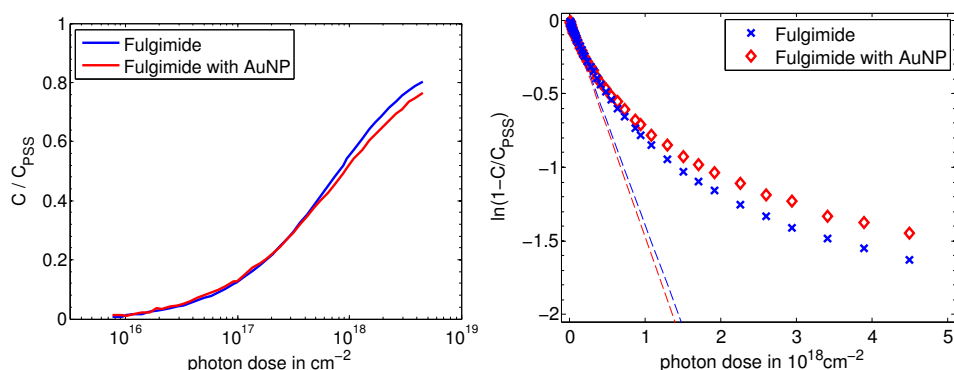


FIGURE 5.10: Ring closing reaction due to UV light for a fulgimide monolayer without (blue) and with AuNP (red). The corresponding cross sections are represented by dashed lines.

In the right panel the kinetics curve of a fulgimide monolayer with gold nanoparticles is shown by the red diamonds to determine the cross section. As a reference again another ring closing switch is shown of the same sample without any nanoparticles (blue crosses). The cross sections are determined at the beginning of the kinetic curve and are represented by dashed lines with slope $\sigma_{E \rightarrow C}$ as in chapter 3. The determined cross section of the ring closing isomerization under UV light with and without AuNP are $\sigma_{E \rightarrow C} = 1.38 \cdot 10^{18} \text{ cm}^2$ and $\sigma_{E \rightarrow C, AuNP} = 1.46 \cdot 10^{18} \text{ cm}^2$, respectively. This non-significant variation of the cross section is within the uncertainty of about 10% that has been observed before. All cross sections are listed in table 5.1 in the end of this section.

5.3.4 Kinetic parameters of the ring opening reaction

The ring opening kinetics under visible light is studied in the same way as the ring closing reaction has been examined. To do so different wavelengths in the visible spectrum are used to excite the photochromes. The results are ordered for increasing wavelengths starting from 525 nm to 655 nm.

The ring opening reaction due to non-polarized green light of 525 nm is shown in figure 5.11. The kinetic curve of the fulgimide with the

AuNP is shown as red diamonds, the reference without the nanoparticles as blue crosses. Similar as for the ring closing reaction, at the beginning of the ring opening commutation the kinetic curves are very similar. But for long time irradiation the switching kinetics with nanoparticles are slightly slower. The determined cross sections for the ring opening isomerization with and without AuNP are $\sigma_{C \rightarrow E, AuNP} = 2.74 \cdot 10^{-19} \text{ cm}^2$ and $\sigma_{C \rightarrow E} = 2.57 \cdot 10^{-19} \text{ cm}^2$, respectively.

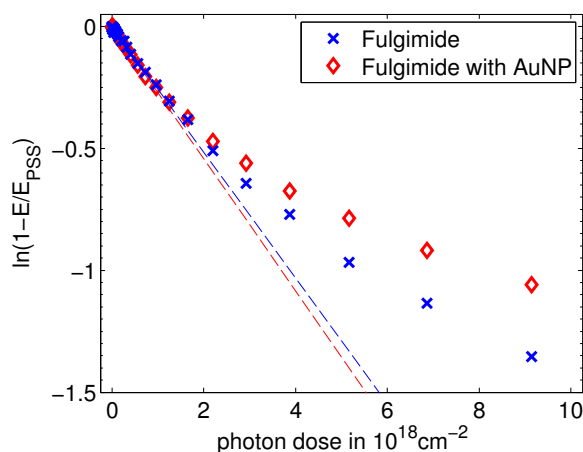


FIGURE 5.11: Influence of the gold nanoparticles on the ring opening reaction kinetics for the illumination of visible light (525 nm).

Additionally, the photo commutation due to s and p polarized light of 590 nm has been studied. The results are shown in figure 5.12. The two top panels show the kinetic curves for p polarized light, in the two bottom panels the kinetic curves for s polarized light are displayed. First the normalized number of switched isomers is displayed (left) and then the kinetic curves used to determine the cross sections are shown (right). The photo commutation of the reference fulgimide monolayer without nanoparticles is displayed in blue, the photo commutation of the fulgimide with nanoparticles in red.

The first significant influence of the AuNP monolayer on the photo commutation kinetics is measured when p polarized light of 590 nm induces the photo isomerization. At the beginning the photo commutation of the fulgimide under the AuNP monolayer is quicker than for the reference commutation. But the two kinetic curves cross at a photon dose of

$6 \cdot 10^{18} \text{ cm}^{-2}$. As seen before for long time illumination the fulgimide without nanoparticles isomerize quicker. Since the cross section is determined at the beginning of the isomerization a higher value is calculated for the fulgimide with AuNP: $3.15 \cdot 10^{-19} \text{ cm}^2$ compared to $1.73 \cdot 10^{-19} \text{ cm}^2$ without nanoparticles.

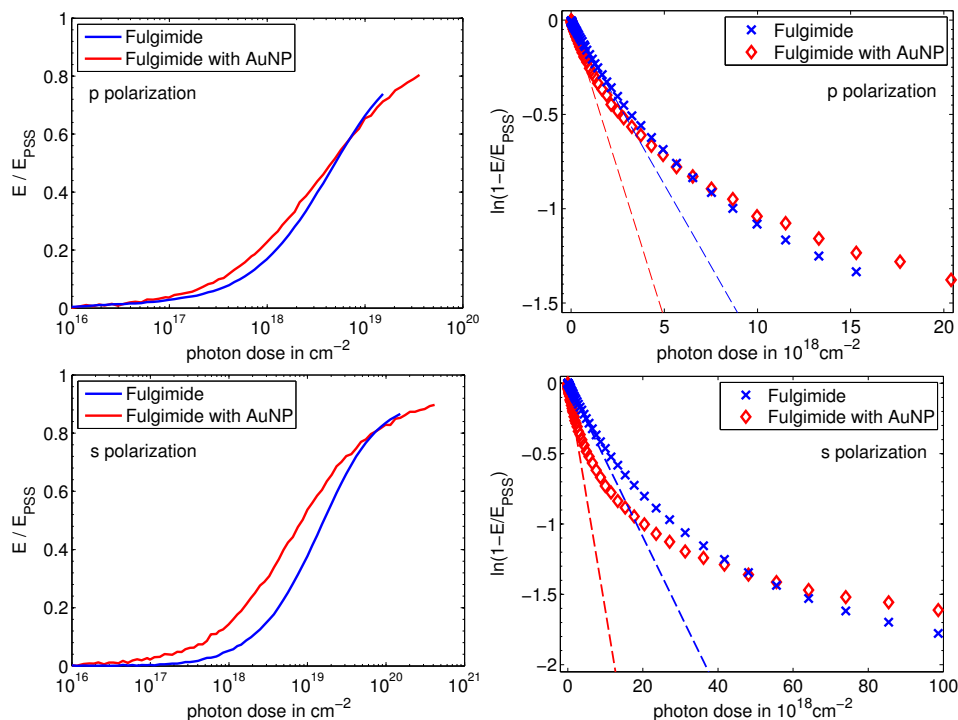


FIGURE 5.12: Photo commutation of fulgimide monolayer with (red) and without (blue) AuNP monolayer. In the top two figures fulgimides are irradiated by p polarized light, in the two lower figures by s polarized light.

The difference between the fulgimide monolayer with and without nanoparticles is even more significant under s polarized light of the same wavelength. Due to the gold nanoparticles, at 10^{17} photons per cm^2 the photo isomerization is already measurable due to the AuNP (red). However, the linear regime for the linear regression to determine the cross sections for the isomerization with and without AuNP is taken until $1 \cdot 10^{18} \text{ cm}^{-2}$ and $4 \cdot 10^{18} \text{ cm}^{-2}$, respectively. This corresponds to only 14% to 20% of the switched isomers which is much lower than the linear regimes of the photo commutations of pure C monolayers of up to 40%. The determined cross sections for the photo commutation with and without nanoparticles are $1.61 \cdot 10^{-18} \text{ cm}^2$ and $0.55 \cdot 10^{-18} \text{ cm}^2$, respectively.

Finally the ring opening reaction is estimated for a red laser of 655 nm. The surface is illuminated with an angle of around 80° with respect to the sample surface, so mainly s polarized light is present. As seen in solution the isomerization cross section at the border of the visible absorption peak of the fulgimide is smaller than for lower wavelengths. The number of switched isomers is relatively low compared to the experiments before with $0.3 \cdot 10^{14} \text{ cm}^{-2}$ to $0.4 \cdot 10^{14} \text{ cm}^{-2}$ at the PSS^{vis} . Since a laser with coherent light is used the surface is not illuminated homogeneously due to a speckle pattern of the laser including interferences of the order of less than 1 mm. The kinetic curves are shown in figure 5.13. The cross section can be roughly estimated to be $0.5 \pm 0.1 \cdot 10^{-19} \text{ cm}^2$ to $0.2 \pm 0.1 \cdot 10^{-19} \text{ cm}^2$ for the ring opening isomerization with and without nanoparticles, respectively.

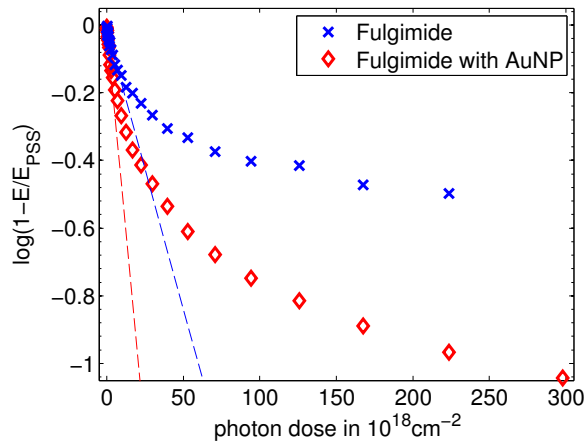


FIGURE 5.13: Photo switching kinetics of a fulgimide monolayer with and without AuNP that are excited by a red laser of 655 nm

wavelength in nm	polarization	σ in 10^{-19} cm^2	σ_{AuNP} in 10^{-19} cm^2	enhancement factor
365	-	13.8	14.6	1.06
525	-	2.57	2.74	1.08
590	p	1.73	3.15	1.8
590	s	0.55	1.61	2.9
655	s	0.2 ± 0.1	0.5 ± 0.1	2.5

TABLE 5.1: Cross sections for the ring closing and opening reaction for the different wavelength and polarization for fulgimide monolayer with and without gold nanoparticles.

The cross sections without gold nanoparticles decrease for an increasing wavelength. This can be motivated as in solution by an decreasing absorption of the light by the C fulgimide at higher wavelengths and optical excess energy [76]. A more detailed study is difficult because the absorption of the fulgimide is not know but will change in a monolayer due to band widening within a molecular crystal and a different environment with respect to solution.

5.4 Discussion

5.4.1 Influence of the AuNP on the photo commutation

The temperature during the illumination of the fulgimide monolayer without AuNP is around 1°C higher than for the blank surface (see D.3 in the annex). Better thermal activation of the ring opening reaction as a result of higher energy absorption due to AuNP can therefore not explain the higher cross sections for the ring opening reaction in the presence of AuNP.

The cross section for the ring closing reaction remains unchanged due to the presence of AuNP as depicted in 5.10. The cross section of the ring opening reaction due to irradiation of 525 nm is not amplified by the presence of AuNP. This is due to the weak interaction of the visible plasmon with UV and green light.

The ring opening and closing reaction are not affected by a separated excitation of the surface plasmon (see annex D). If the reactions are excited due to irradiation of several wavelength at the same time, the cross sections are just added and thus no influence on the quantum efficiency due to the plasmon has been observed.

On the other hand, the cross section for the ring opening reaction using yellow light of 590 nm is significantly increased due to the enhancement of the electric field by the surface plasmon for s and p polarizations.

The higher increase of the cross section for s polarized light with respect to the gain of the cross section in p polarization can be motivated by the higher photon-plasmon interaction when the electric field of the photon is aligned in plane along the AuNP [161].

5.4.2 Dielectric environment of AuNP on Silicon

The photo isomerization kinetic depends on the electric field intensity. The electric field is expected to be enhanced due to the presence of the gold nanoparticles. The electric field $\vec{E}(\vec{r})$ at \vec{r} can be calculated by solving the

electrostatic Poisson's equation:

$$\Delta\Phi(\vec{r}) = \frac{-\rho(\vec{r})}{\epsilon} \quad (5.1)$$

$$-\nabla\Phi(\vec{r}) = \vec{E}(\vec{r}) \quad (5.2)$$

using the charge density $\rho(\vec{x})$, the permittivity ϵ and the electrostatic potential Φ for different systems.

Our system consists of gold nanoparticles on silicon. The permittivity ϵ of free space, gold and silicon is described by the dielectric function of the material at 690 nm. For free space the charge density is zero and Laplace's equation is obtained.

Light, that is irradiated on the surface, consists of electric fields that are parallel E_{\parallel} or perpendicular at the surface E_{\perp} . Perpendicular and parallel electric fields of the incident light corresponds to a different electric potential. These two cases can be considered by solving the electrostatic problem using Dirichlet boundary condition:

$$E_{\parallel} : \quad \Phi(x = -w/2) = 0, \quad \Phi(x = +w/2) = +V_1 \quad (5.3)$$

$$E_{\perp} : \quad \Phi(y = -h/2) = 0, \quad \Phi(y = +h/2) = +V_2 \quad (5.4)$$

with the width w and the height h of a system whose origin is in the center; V_1 and V_2 are the potential differences that excite the electric field.

In this work the simulated systems are two dimensional, the nanoparticles are therefore cylinders. These electrostatic problems have been solved numerically using the program Freefem++⁵ [162].

One exemplary system and the solution of the electrostatic potentials Φ are displayed in figure 5.14. The system consists of a silicon surface and five AuNP. For the simulation of E_{\parallel} a potential difference between the left border and the right border of the system is applied via the boundary condition. This corresponds to the response of the system when irradiated by s polarized light. The solution is displayed by the equipotential lines of

⁵Freefem++ Third Edition, Version 3.17

Φ . The electric field is perpendicular to the equipotential lines, a high density of equipotential lines corresponds to a high electric field perpendicular ($\vec{E} = -\vec{\nabla}\Phi$).

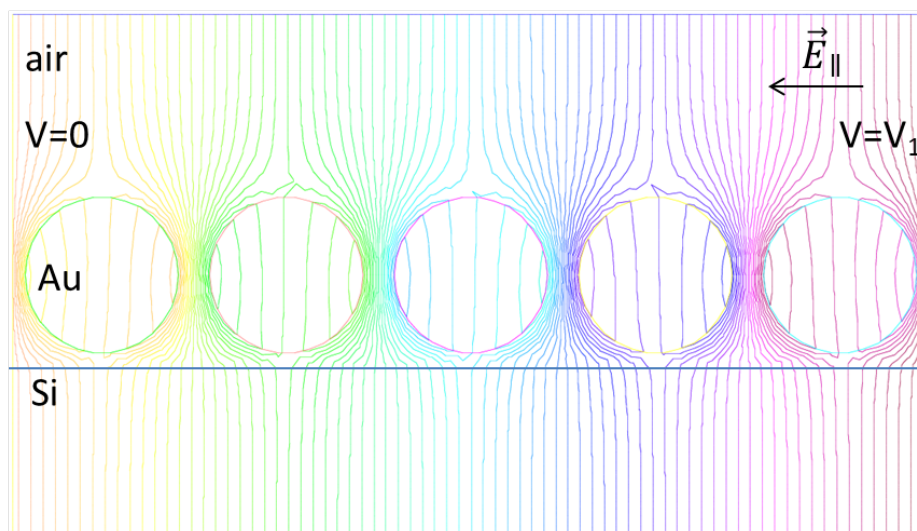


FIGURE 5.14: Calculation of the electrostatic potential Φ of gold nanoparticles at the silicon surface under a parallel electric field E_{\parallel} . Equipotential lines of Φ are displayed in different colors.

For an electric field that is parallel to the surface as in figure 5.14 the electric field between the nanoparticles is extremely high. On the other hand, directly under and above the nanoparticles the electric field is much weaker.

For the same system the electrostatic potential is calculated for an applied perpendicular voltage. The solution is again displayed by equipotential lines of Φ . In difference to the results shown above, for a perpendicular electric field the resulting electric field between the nanoparticles is relatively weak but above and under the AuNP the electric field is large.

The electric field in diverse configurations is calculated by varying the distance between the nanoparticles and the number of nanoparticles. The same calculations have been repeated for an infrared beam to gain insight in the infrared enhancement by using the dielectric function for the infrared light in the carbonyl region (5880 nm). For the calculation of the electric field enhancement the different configurations are taken into account. The same systematic electric field enhancements have been found and an averaging

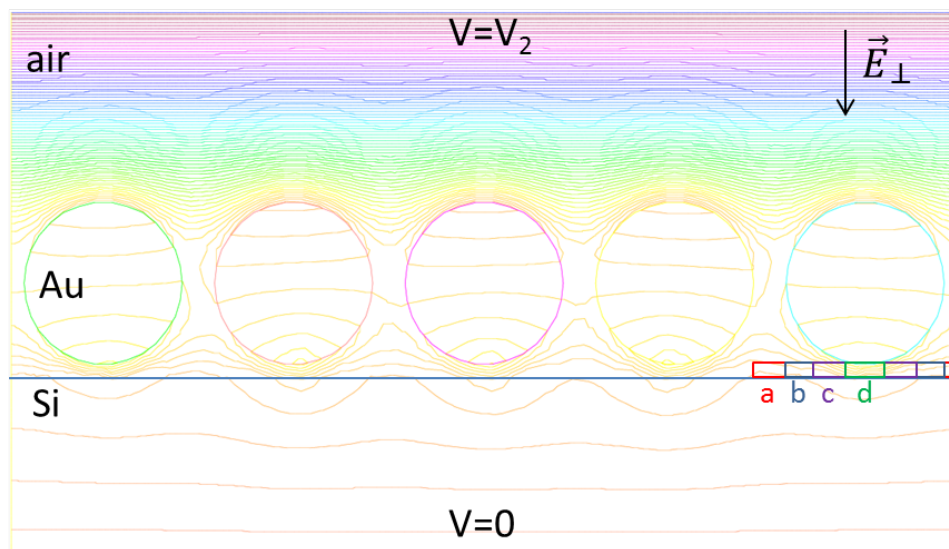


FIGURE 5.15: Electrostatic potential at the silicon surface with AuNP for an external perpendicular electric field

over the different configurations is meaningful to approach our experimental submonolayer of AuNP.

The photo commutation of the fulgimide monolayer with AuNP is measured by a p polarized infrared beam. The p polarized infrared beam has a parallel and perpendicular electric field component and its infrared enhancement can therefore be calculated by both electric field enhancements.

The fulgimide are in the zone between the AuNPs and the silicon. This zone is divided in four different zones **a** to **d**, from the uncovered zone **a** to the zone **d** where the AuNP is in contact with the fulgimide layer (see zones in figure 5.15). The enhancement of the electric field of the irradiated light is calculated for the two electric field directions for the different zones. The enhancement of the electric field of s polarized light is given by the enhancement of the parallel electric field. P polarized light of 590 nm has basically a perpendicular electric field: $E_{\parallel} \approx 0.2E_{\perp}$ (analog to 3.2 using $\theta = 45^{\circ}$ and $\lambda = 590$ nm). Accordingly its enhancement factor for the electric field can be calculated. The enhancement factors are displayed in figure 5.16 for a perpendicular and parallel electric field. The enhancement of the infrared beam in p polarization used to measure the infrared absorbance is displayed, too.

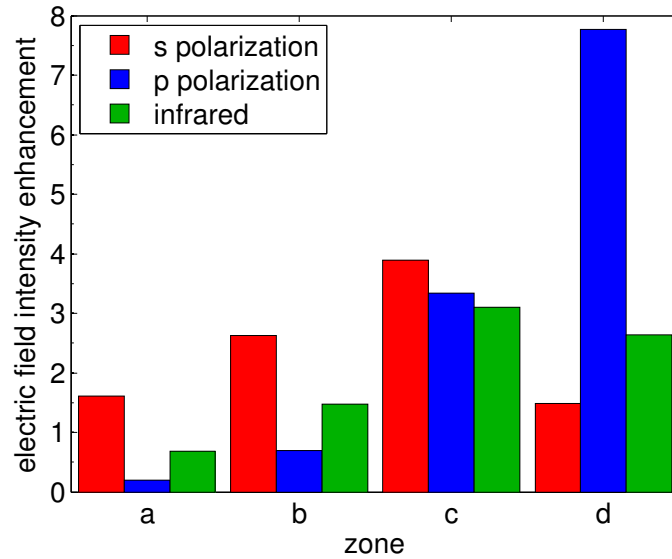


FIGURE 5.16: Electric field enhancement for the infrared beam and illuminated light of 590 nm in s and p polarization for the different zones.

Using a surface density for the AuNP of $3.1 \cdot 10^{11} \text{ cm}^{-2}$ the number of isomers in the different zones can be calculated considering the spherical symmetry of the AuNP (see table 5.2). In the experiment the infrared absorbance is measured. The different zones contribute differently to the total measured infrared absorbance due to the different infrared sensitivity in the different zones. Therefore the 'IR absorbance' in the table accounts for the different contributions of the zones due to their different infrared electric field enhancement.

zone	a	b	c	d
isomers	58.7%	26.5%	13.2%	1.7%
IR absorbance	32.3%	31.3%	32.9%	3.5%

TABLE 5.2: Number of isomers in the different zones and their contribution to the measured infrared absorbance

This approach only concentrates on the electric field intensities. The orientation of the electric field and the change of its orientation due to the AuNP are neglected.

The absolute value of the non polarized electric field for the irradiation of visible light (525 nm and 590 nm) in the vacuum is about 600 V/m. Therefore, even if the electric field is enhanced by the AuNP it remains too weak to influence the energy barriers of the molecule. Therefore one can assume that the quantum efficiency is unchanged due to the electric field. The absorbance cross section on the other hand is expected to increase with the higher electric field.

5.4.3 Influence electric field enhancement on the photo commutation

Different electric field enhancements for the different zones on the monolayer are expected. In the experiments the global change of the infrared absorbance on the whole sample is measured. But the molecules in the different zones contribute differently to the measured infrared signal. If we want to compare the average increase of the calculated electric field intensity with the experiment, the different IR sensitivities for the different zones must be taken into account. The average measured electric field intensity is the mean of the electric field enhancement of figure 5.16 weighted with the contribution of the isomers in the different zones to the global infrared absorbance (table 5.2). For s polarized light, an average increase of the weighted electric field intensity by a factor of 2.7 is calculated. This quantitatively explains very well the higher isomerization cross section measured due to s polarized light that increases by a factor of 2.9.

For p polarized light, the enhancement of the electric field intensity under the nanoparticles is very strong, but the weighted electric field enhancement over the whole sample increases by only 9%. This seems to be a contradiction to the experimentally observed cross section enhancement by 82% in p polarization. But the stated enhancements of the cross sections are only calculated at the beginning of the isomerization. Consequently, rather than comparing the average electric field intensity enhancement to the cross section amplification at the beginning, it is more meaningful to compare the evolution of the cross section during the photo commutation

to the electric field enhancement in the different zones. In figure 5.17 the isomerization cross section is numerically determined during the commutation for illumination of p polarized light of 590 nm. The x-axis shows the measured relative number of fulgimide that switch with respect to the switchable number of fulgimide (neglecting the different sensitivities). The cross sections with and without nanoparticles are shown in blue and red, respectively.

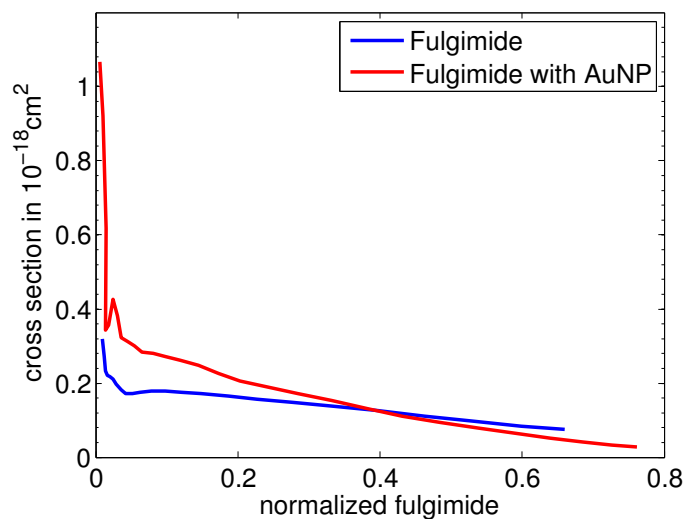


FIGURE 5.17: Evolution of the ring opening cross section of blank (blue) and AuNP covered (red) fulgimide monolayer. The monolayer is illuminated by p polarized light of 590 nm.

At the very beginning of the numerical cross section $\propto \frac{dE}{dn}$ is very sensitive to noise and systematical uncertainties due to the small amount of switched isomers dE and the small photon dose dn (as seen before in 3.18). However, the numerical initial cross section indicate a strong enhancement at the very beginning of the commutation that may correspond to the strongly enhanced isomers in zone **d**. Then one can clearly see that the fulgimide covered by AuNP the cross section is higher for the first 40% and then decreases. This quantitatively matches the theoretical results that for p polarization the zones **c** and **d** under the nanoparticle isomerize quicker. The lower cross section for the second 60% may be explained by the isomers in zone **a** or **b** whose electric field is expected to decrease due to the

nanoparticles. Possibly some isomers of the zone **a** without AuNP are considered as not switchable due to their significantly decreased electric field intensity/cross sections.

In figure 5.18 the numerical cross section for s polarization is displayed in the same way as for p polarized light before. The cross section with AuNP is significantly higher (around $\sigma = 0.16 \cdot 10^{-18} \text{ cm}^2$) as shown in table 5.1. As for p polarized light two intervals are observable: until 60% of the commutation the switching kinetics is amplified by the AuNP, then it is quasi similar.

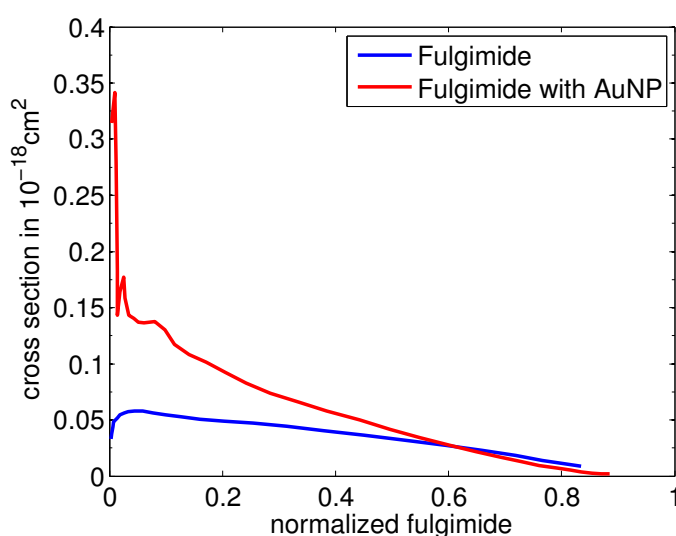


FIGURE 5.18: Numerical ring opening cross section due to s polarized light of 590 nm

The electric field calculations predict that more isomers switch with a higher cross section for s polarized light than for p polarized light which is in agreement with the experiment. But for a parallel electric field even in the **a** zone no decrease of the electric field is expected. In this experiment s polarized light is obtained by an incident angle of 45° and a polarizer. However, due to the usage of a polarizer instead of perpendicular irradiation there will always be a fraction of unwanted p polarized besides the desired s polarized light because the polarizer is not perfect and its polarization angle does not perfectly match the optical beam angle. Therefore, the s polarized light will always include some perpendicular electric field. The slight decrease for the last 40% can consequently be motivated by a

mix of both polarizations. Again this low cross section may then be due to isomers in the zone **a** that are not covered by AuNP. But other explanations, like steric effects of the AuNP or a different chemical environment due to the citrate, could motivate the decrease, too. Fatigue effects may be increased due to the AuNP and at high photon doses, but it would be difficult to distinguish fatigue effects from a influence of a heterogeneous electric field.

At the very beginning of the commutation a significantly larger cross section is measured for s and p polarized light. In figure 5.19 a zoom at the beginning of the kinetic curve for the photo-switching under s polarization is displayed. The kinetic curve of the photo switching due to s polarized light of 590 nm without AuNP is shown in blue. The shown kinetic curve until -0.05 (first 5%) is linear and are well described by the upper linear black curve through the origin. The slope and therefore cross section of this curve is $0.55 \cdot 10^{-19} \text{ cm}^2$.

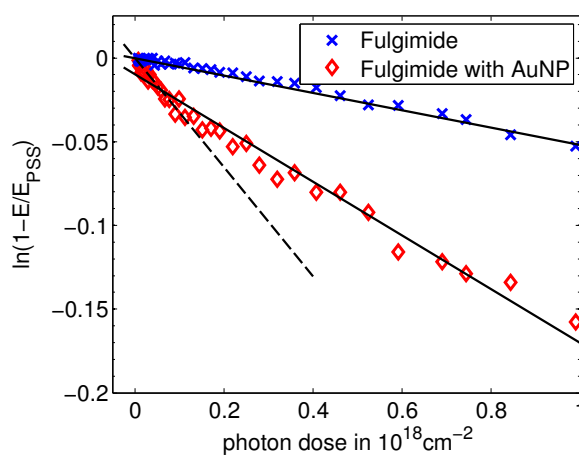


FIGURE 5.19: Zoom on the kinetic curve for the s polarized ring opening reactions due to 590 nm. The blue crosses and red diamonds show the kinetic curve without and with nanoparticles. Without AuNP the kinetic curve shows a linear regime (solid line), with AuNP at the beginning of the switch the kinetic does not follow the linear regime (dashed and lower solid line)

The red diamonds show the kinetic curve under s polarized yellow light of 590 nm in the presence of AuNP. The cross section of $1.61 \cdot 10^{-19} \text{ cm}^2$ is determined by the lower solid black curve. However, in difference to

all other kinetic curves of the ring opening and closing reaction, the measurement points are not linear at the beginning of the photo commutation. The solid black line does not cross the origin, at the very beginning the photo commutation is even faster. The dashed line is fitted to the kinetic curve until $0.1 \cdot 10^{18}$ photons per cm^2 and corresponds to a cross section of $3.26 \cdot 10^{-19} \text{ cm}^2$. However, only around 2% of the measured isomers isomerize with this higher cross section. The origin of the disappearance of the linear regime and the very high cross section at the very beginning of photo commutation is due to the non homogeneous electric field enhancement due to the AuNP [136]. For s and p polarization the very high cross sections for a minority of the isomer indicate hot spots of the electric field enhancements directly under the nanoparticle in zone *d*. In p polarization the increase at the beginning is more pronounced because only the perpendicular electric field creates the hot spot. In s polarized light less perpendicular light is present and therefore the increase is relatively and absolutely weaker. Again, the 2% of the measured isomers are overestimated due to the higher infrared sensitivity at the hot spots.

The strong enhancement directly under the nanoparticles could motivate to increase the nanoparticle density. The IR sensitivity should increase due to the plasmon enhancement. But in fact the signal to noise ratio decreases due to the absorbance of the infrared beam by the gold nanoparticles. Therefore studies of fulgimide monolayers with a dense layer of gold nanoparticles would lower the high precision that is necessary for the analysis of the switching kinetics and are not performed here.

5.5 Conclusions

Submonolayer of gold nanoparticles have been attached on top of fulgimide monolayer. The sensitivity of the infrared spectroscopy thereby increases.

Although a submonolayer of AuNP is added the photochromism of the fulgimide monolayer is conserved. The characteristic differential infrared spectrum corresponding to the isomerization is not affected by the AuNP. The photo switching properties of the fulgimide monolayer with nanoparticles are compared to the photo-switching properties without nanoparticles on the same sample.

The cross section of the ring closing photo-isomerization due to UV light is not affected by the presence of the AuNP.

For the ring opening reaction the influence of the nanoparticles on the photo commutation properties strongly depends on the excitation wavelength and the polarization. For green light of 525 nm no significant effect on the cross section is observed because the visible plasmon just starts at this wavelength. Separate plasmon excitation does not affect the cross section of the ring closing or ring opening reaction (525 nm) demonstrating the exclusive influence of the surface plasmon on the absorbance process and not on the quantum efficiency.

For photo commutation using 590 nm, the cross section is significantly increased depending on the polarization. The gain of the cross section in s polarization is higher due to the better alignment of the electric field with respect to the AuNP. The higher cross sections can be explained by the higher electric field intensities due to the AuNP. The enhancement of the electric field intensity is not homogeneous but strongly depends on the position relative to the nanoparticles. A minority of the isomers are switched with a very high cross section that can be explained by hot-spots of the electric field between the AuNP and the silicon.

General Conclusion

The aim of this work is the study of the photo-switching properties of amino substituted indolyl fulgimide in different environments and to determine the main factors that influence the isomerization.

The photochromism of fulgimide occurs between closed C and the open E and Z form by the electrocyclic ring opening $C \rightarrow E$ isomerization and the reverse ring closure reaction $E \rightarrow C$ that are induced by visible and UV light, respectively. The isomeric compositions at the photo stationary states and switching kinetics of the fulgimide is discussed in acetonitrile and on surfaces.

As a reference, the photo switching behavior is examined in solution by in-situ UV-visible spectroscopy. C fulgimide isomerize to the open form under visible light of different wavelengths, the ring closing reaction is observed under UV light. Reversible photochromism of the fulgimide is observed despite a long time photo degradation. The visible photo stationary state consists of 100% open isomers. The UV photo stationary state prior to fatigue effects consists of 23% open and 77% closed isomers because UV light induces the ring opening reaction, too. The switching cross section and quantum efficiencies are determined for the ring opening and closing reaction. The numerical cross section for the ring closing reaction decreases during the isomerization, no first order kinetics are observed. The cross sections and quantum efficiencies of the ring opening reaction is constant during the isomerization but decrease with increasing wavelength.

The amino substituted fulgimide are anchored on functionalized silicon surfaces. Photochromic monolayers with different surface densities between $0.6 \cdot 10^{14}$ and $1.8 \cdot 10^{14}$ isomers per cm^2 are prepared.

The photo switching properties of fulgimide monolayers of silicon surfaces have been studied in situ by FTIR spectroscopy in ATR geometry. Reversible photo switching of the fulgimide monolayers is observed. The isomeric composition at the visible photo stationary state depends on the surface density: for diluted monolayers all isomers are isomerized as in solution, on dense monolayer the relative number of switched isomers decreases. The UV photo stationary states for the different densities are similar independent of the number of photochromes on the surface.

The switching kinetic of fulgimide monolayer on surfaces does not obey mono or bi exponential behavior. Cross sections are determined at the beginning of the isomerization and show no dependence of the photochrome density. Furthermore, different cross sections have been measured for the same isomeric composition of fulgimide monolayer due to different isomeric compositions at the beginning of the isomerization. The quantum efficiency of the ring opening reaction is thermally activated.

The experimentally higher cross section for p polarized light with respect to s polarized light for both isomerization directions demonstrates the quadratic dependence of the isomerization kinetic on the local electric field. Most of the gap between the high cross section in acetonitrile and the lower cross sections on surfaces can be motivated by the local electric field. Deviations of the electric field intensity dependence of the cross section indicate a transition dipole dependence parallel to the surface for the ring closing reaction.

The ring opening reaction on surfaces is thermally activated. The apparent activation energy increases during the commutation of the monolayer which indicates the environment dependence of the isomerization. The ring closing reaction shows no temperature dependence.

Monte Carlo simulations of the ring opening reaction of different monolayers are performed. The developed model accounts for the local environment by nearest neighbor interactions that influence the quantum efficiency. The Monte Carlo simulations qualitatively explain the decreasing

cross sections and their thermal activation that have been measured. Simulations with different densities show different photo stationary states but similar kinetic behaviors for monolayers of different densities as observed in the experiments. Furthermore, the experimental observation of different cross sections at the same isomeric compositions is reproduced by the simulations.

The influence of a gold nanoparticle submonolayer and the corresponding surface plasmon on the switching kinetics is investigated. The photochromism is conserved in the presence of the nanoparticles. The influence of the nanoparticle on the switching kinetics strongly depends on the surface plasmon. No enhanced isomerization kinetics are observed for the ring closing reaction under UV light. For the ring opening reaction under visible light the enhancement strongly depends on the wavelength. No significant enhancement is measured for green light at 525 nm whereas for higher wavelengths the isomerization kinetics is enhanced. Moreover the amplification of the switching kinetics strongly depends on the polarization of the exciting light. Calculations of the electric field enhancement for s and p polarization can quantitatively explain the increased cross sections. The enhancement of the isomerization kinetics depends on the local position of the isomer with respect to the nanoparticles.

To conclude, by experiments and simulations, the influence of the environment on the photochromism of fulgimide monolayer is investigated. Nearest neighbor interactions within the monolayer can account for the decreasing cross section during the isomerization that result in a slow saturation. The local and global electromagnetic environments crucially influence the photo switching kinetics of the photochromic monolayer.

Appendix A

Supplementary Information for Chapter 1

A.1 Basic principle

Infrared light excites vibrational and rotational modes of molecules on surfaces and in solution. In Fourier transformed infrared spectroscopy this effect is exploited by irradiation of a polychromatic infrared beam on the molecules that is created by an interferogram. The absorption of the infrared beam by the molecules is measured. Thereby a detector measures the intensity of the infrared beam with respect a interferogram specific parameter that represents the path difference. After a Fourier transformation the intensity of the intensity of the infrared beam for different wavelength is obtained.

Since a monolayer does not contain many absorbers the infrared beam a simple absorption experiment where the infrared beam passes the sample results in a significant amount of noise. Therefore, instead of simply transferring the sample by an infrared beam, in attenuated total reflection (ATR) geometry the infrared beam is kept inside the substrate and performs several total internal reflections at the substrate-medium interface. This requires a medium of low refractive index to meet the angle criteria for total reflection $\theta_C = \sin^{-1} \left(\frac{n_{med}}{n_{sub}} \right)$. The electromagnetic field in the medium exponentially decays with a characteristic decay length of $d = \frac{\lambda}{2\pi\sqrt{(n_{Si} \sin^2(\theta) - n_{med})}}$ where λ and θ represent the wavelength and incident angle of the infrared beam. ATR geometry requires a substrate that does not strongly absorb the infrared beam and therefore conducting materials like gold are not adapted.

In this work the functionalized infrared spectra are recorded in the mid infrared region between 4000 cm^{-1} to 400 cm^{-1} (or 0.5 eV to 0.05 eV) using a Bruker (Equinox55) that only enables single channel measurements. A mercury cadmium telluride detector is cooled by liquid nitrogen. The

high precision measurements of the photo commutation are time consuming and therefore to optimize the signal measured per time the infrared beam is continuously recorded during the interferogram movement. The infrared spectra are recorded for 5 minutes for the sample characterization using a s and p polarized beam with a resolution of 4 cm^{-1} . For the kinetic measurements only p and s polarized measurements reveal the same results to save time only the p polarized light is used with 100 to 150 scans. The spectrometer infrared chamber are continuously flushed by nitrogen.

A.2 Quantitative analysis

Principle

A method to extract quantitative information about density of molecules on the surface from the measured infrared absorbance has been developed in the laboratory[63]. The idea is to compare the absorbance of the molecules on the surface with a calibration measurement in solution while respecting their different dielectric environment and different geometries.

Following Chabal [121] the absorbance per reflection of a layer of thickness δ in s and p polarization at a given wavelength λ can be expressed as:

$$A_s = \frac{2\pi}{\lambda} \frac{1}{n_{Si} \cos(\theta)} I_y \epsilon'' \delta \quad (\text{A.1})$$

$$A_p = \frac{2\pi}{\lambda} \frac{1}{n_{Si} \cos(\theta)} \left(I_x \epsilon'' \delta + I_z \frac{n_{med}^4}{\epsilon'^2 + \epsilon''^2} \epsilon'' \delta \right) \quad (\text{A.2})$$

with the incident angle $\theta=45^\circ$. I_x , I_y and I_z are numerical coefficient that represent the intensity of the electric field that are given by

$$I_x = \frac{4n_{Si}^2 \cos^2(\theta) (n_{Si}^2 \sin^2(\theta) - n_{med}^2)}{n_{med}^4 \cos^2(\theta) + 4n_{Si} \sin^2(\theta) - n_{Si}^2 n_{med}^2} \quad (\text{A.3})$$

$$I_y = \frac{4n_{Si}^2 \cos^2(\theta)}{n_{Si}^2 - n_{med}^2} \quad (\text{A.4})$$

$$I_z = \frac{4n_{Si}^2 \cos^2(\theta) \sin^2(\theta)}{n_{med}^4 \cos^2(\theta) + 4n_{Si} \sin^2(\theta) - n_{Si}^2 n_{med}^2} \quad (\text{A.5})$$

One can split the number of vibration dipoles in N_\perp and N_\parallel that are aligned perpendicular and parallel to the surface. Then N_\perp and N_\parallel represent $\sum_i \cos^2(\theta_i)$ and $\sum_i \sin^2(\theta_i)$, respectively, summing up the individual vibrations with an angle θ_i with respect to the surface normal.

In the calibration measurements in solution the absorbance of the vibrators is measured in ATR geometry, too. Taking the depth d of the evanescent

field in a liquid of refractive index $n_{med} = n_l + ik$ the absorbance per reflection is given by

$$A'_s = \frac{2\pi}{\lambda} \frac{1}{n_{Si} \cos(\theta)} I_y 2n_l k \frac{d}{2} \quad (\text{A.6})$$

$$A'_p = \frac{2\pi}{\lambda} \frac{1}{n_{Si} \cos(\theta)} (I_z + I_x) 2n_l k \frac{d}{2} \quad (\text{A.7})$$

$$(\text{A.8})$$

The factors I_i depend on the medium and are in particular different for air and an organic liquid.

In order to conclude the number of vibrators on the surface by the number of vibrators in the solution we have to assume that the absorption coefficient on surfaces is proportional to the vibrator concentration in solution with the same proportionality factor.

Using the concentration of vibrations C one gets:

$$\frac{N_{\perp}/\delta}{C/3} = \frac{\epsilon''}{2kn_l} \quad (\text{A.9})$$

where the factor 1/3 accounts for the isotropic orientations of the vibrators in solution. In a similar way one obtains

$$\frac{N_{\parallel}/\delta}{C/3} = \frac{\epsilon''}{2kn_l} \quad (\text{A.10})$$

Thereby one can easily determine the number of vibrators to be

$$N_{\parallel} = \frac{A_s I'_y C d}{A'_s I_y 3} \quad (\text{A.11})$$

and a similar expression for the number of perpendicular vibrators N_{\perp} is obtained by neglecting ϵ'' (small for semiconductors that do not strongly absorb the wavelength λ)

$$N_{\perp} = \frac{I_y A_p - I_x A_s I'_y C d}{I_z A'_s / n_l^4 I_y 6} \quad (\text{A.12})$$

The expression for N_{\parallel} per area can be interpreted by the ration of the absorbance on surfaces and in solution $\left(\frac{A_s}{A'_s}\right)$ normalized with their electric field intensity $\left(\frac{I'_y}{I_y}\right)$ and the vibrator concentration Cd per area.

For N_{\perp} one has additionally to subtract the contribution of N_{\parallel} that is present in p polarized light that is not perpendicular.

Fitting Procedures

To determine the integral of the absorbance peaks the infrared spectra need to be fitted. A program based on matlab has been designed to stabilize particular fitting procedures including several peaks. Voigt profiles, or their special cases of Gaussian or Lorentzian functions, have been implemented using the complex error function following Schreier et al. [163]. The diverse Voigt profiles and baselines can be fitted at the experimental data simultaneously using least mean squares. Parameters can be fixed and weights can be included. The idea of the program is to decrease the degrees of freedoms of complicated fits by linearly correlating fitting parameter in intelligent ways. In ordinary fitting routines the function $f(a_i, x)$ is fitted to the data d by minimizing $\sum_j (f(a_i, x_j) - d(x_j))^2$ for different parameter sets a_i for all data points j . The new program now can be used to correlate the parameter a_i of a set of n parameters. Therefore the parameter a_i are replaced by:

$$a_i \rightarrow \sum_l^n b_{l,i} \hat{e}_i a_i \quad (\text{A.13})$$

using the quadratic matrix $b_{l,i}$ and the unity vector \hat{e}_i . Fitting parameter can now be correlated by increasing number zero-eigenvalues of the matrix $b_{l,i}$. In fact the rank of the matrix $b_{l,i}$ represents the degrees of freedom of the fit. For the special case $b_{l,i} = \mathbb{1}$ the ordinary case of uncorrelated fitting parameter is obtained.

Quantification of succinimidyl ester

The surface density can be calculated by the absorbance in p and s polarization using a calibration measurement in solution using equations A.11 and A.12. This is shown representatively by the calibration of succinimidyl ester surfaces whose procedure has been improved.

The infrared absorbance of succinimidyl ester is done in Tetrahydrofuran (THF). The absorbance for different concentrations in shown in the right panel of figure A.1. Three peaks are visible at 1745 cm^{-1} , 1787 cm^{-1} and 1817 cm^{-1} as described in 1.3.2. Taking a forth peak at around 1720 cm^{-1} into account, the absorbance spectrum can be fitted by Voigt functions without problems. In the right panel the integrated absorbance for the three carbonyl peaks at different concentrations in shown. The integrated absorbance linearly increases with the concentration and therefore slope $\frac{A'_p}{C}$ can be determined for the desired peak and wavelength. Due to physisorption on the silicon surface there could be a non linear relation. In this case a linear regime at higher concentrations needs to be considered.

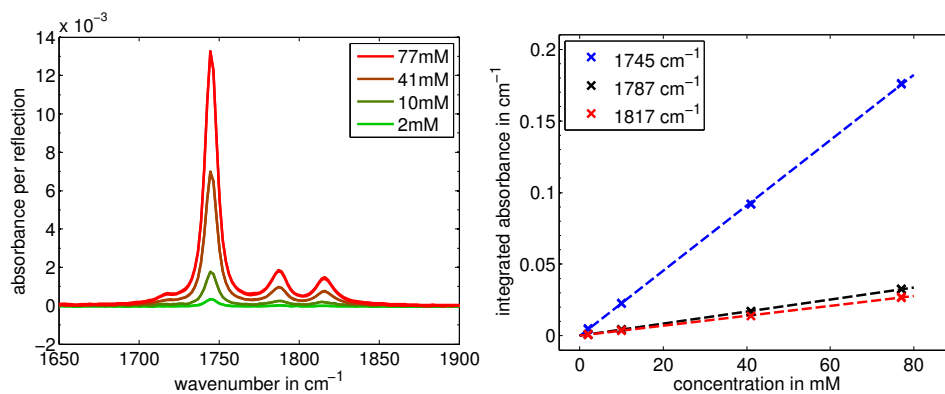


FIGURE A.1: Calibration of the absorbance of succinimidyl ester. Left: absorbances for different ester concentrations. Right: integrated absorbance for the three carbonyl peaks at different concentrations

In molecular crystals like organic monolayer there is a widening of the absorption bands that creates a significant overlap between the three carbonyl bands. Therefore the fitting of the three carbonyl bands is more difficult and the new method of correlated parameter is developed and exemplary shown for the NHS surface. For the linear correlation of the fitting parameter the ratio of the integrated absorbance of the different peaks needs to be calculated. In figure A.2 the integrated absorbance of the two minor peaks at 1787 cm^{-1} and 1817 cm^{-1} is shown in units of the main carbonyl peak at 1745 cm^{-1} . Thereby for the peaks at 1787 cm^{-1} and 1815 cm^{-1} the ratios of integrated absorbances of 0.1862 and 0.1521 are calculated, respectively.

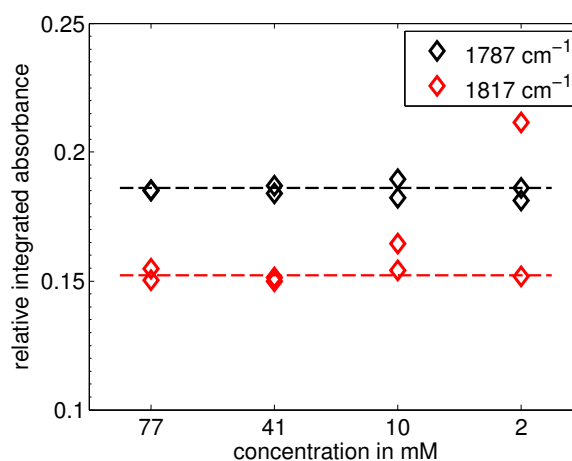


FIGURE A.2: Integrated absorbance of the peak at 1787 cm^{-1} and 1817 cm^{-1} divided by the integrated absorbance of the 1745 cm^{-1} in THF. The mean ratio is shown by a dashed line

Given a Voigt profile to be $V(A_i, w_{G_i}, w_{L_i}, p)$ using the peak integral A_i , the position p and the width of the convoluted Gaussian and Lorentzian function to be w_{G_i} and w_{L_i} . In figure 1.5 three correlated Voigt peaks have

been fitted to the absorbance whose integrals are correlated. To do so a matrix $b_{l,i}$ can be chosen so that instead of fitting the three independent Voigt peaks one fits $V(A_1, w_{G1}, w_{L1}, 1745) + V(0.1862A_1, w_{G2}, w_{L2}, 1787) + V(0.1521A_1, w_{G3}, w_{L3}, 1817)$. Now only a single parameter A_1 represents the integrals for all three peaks. The reduction of the degrees of freedom by correlating central parameter of the fit greatly increases its robustness of the fit and density determination.

The number of succinimidyl ester on the surface is finally calculated by the peaks at 1787 cm^{-1} and 1815 cm^{-1} . For an incident angle of 45° one obtains the following densities as functions of the s and p absorbance A_s, p, ν at the concerned wavenumber ν :

$$N_{\parallel} = 1.10 \cdot (A_{s,1787} + A_{s,1817}) \cdot 10^{16} \text{ cm}^{-1} \quad (\text{A.14})$$

$$N_{\perp} = (1.99(A_{p,1787} + A_{p,1817}) - 1.80(A_{s,1787} + A_{s,1817})) \cdot 10^{16} \text{ cm}^{-1} \quad (\text{A.15})$$

Quantification of carboxylic acid monolayer

For the calibration of carboxylic acid monolayers a Voigt function is fitted to the infrared absorbance as shown in 1.4. The main peak has a mainly Lorentzian shape and its position is at 1714 cm^{-1} . A Gaussian peak is considered for impurities at 1740 cm^{-1} . Using a calibration measurement performed by Moraillon[59], the surface density of carboxylic acid monolayers can be calculated using the integrated absorbances in s and p polarization:

$$N_{\parallel} = 5.75 \cdot A_s \cdot 10^{16} \text{ cm}^{-1} \quad (\text{A.16})$$

$$N_{\perp} = (1.04A_p - 0.94A_s) \cdot 10^{16} \text{ cm}^{-1} \quad (\text{A.17})$$

Appendix B

Supplementary Information for Chapter 3

B.1 Disappearance of impurities during successive commutations

For the received C fulgimide in solution a broad visible absorbance band has been measured at 400 nm that disappears due to UV irradiation. The same C fulgimide are immobilized on the surface and therefore the unknown conformation or species may be present on the surface, too, that may disappear during the first UV irradiation. Therefore as in solution an as received initial C fulgimide monolayer is prepared and subsequently illuminated by visible and UV light for several commutations. To study the disappearance of the species or conformation the differential infrared spectrum of the first UV commutation is compared to the differential infrared spectra of subsequent UV commutations.

In figure B.1 the differential spectra of the first, second and third UV commutations are shown. The differential spectra are normalized to one to account for the different amounts of switched isomers. All spectra have exactly the same shape and no major difference is visible. However, the differences of the normalized differential spectra (shown in blue) indicate a loss under the first UV irradiation by small negative peaks corresponding to fulgimide or benzene (e.g. 1600 cm^{-1}). This difference is no scaling feature since no difference is visible in the carbonyl region. This loss is only present due to the first UV irradiation (spectra 2 and 3 are very similar). Photo degradation should be equally present in all UV commutations and can therefore not account for the difference. This indicates that some precursors of the synthesis or benzene may be attached to the closed fulgimide that disappear during the UV irradiation. As in solution no negative influence of the impurities on the cross section that is superior to the measurement precision is observed.

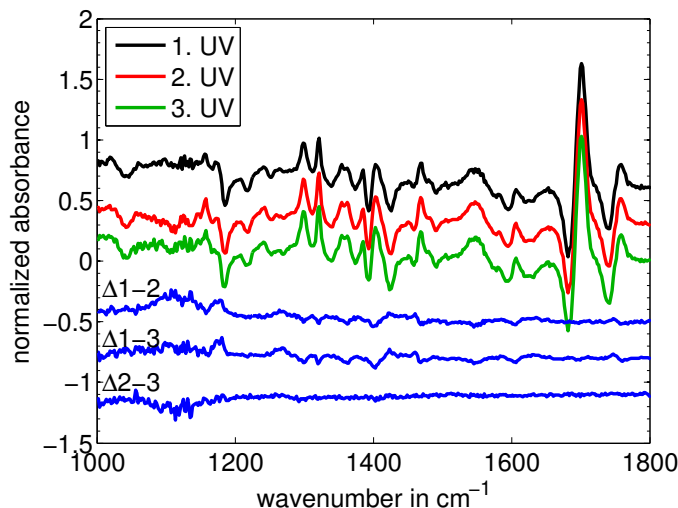


FIGURE B.1: Differential infrared absorbance spectra of the first three UV induced switches of a as prepared C monolayer. The difference between the differential curves show negative peaks that indicate the loss of some species due to the first UV irradiation.

B.2 Inert atmosphere FTIR-cell

For the study of the photo commutation of fulgimides on silicon surfaces the experimental setup of chapter 1.5.1 has been used, if not stated otherwise.

The cell displayed in B.2 enables to control the local atmosphere at the sample inside the FTIR spectrometer.

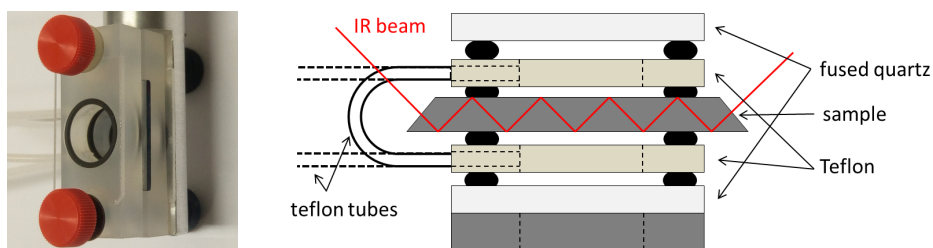


FIGURE B.2: Inert atmosphere FTIR-cell

The cell consists of two volumes defined by the sample, fused quartz glasses and the Teflon support. The cell can be filled by gases or liquids using the Teflon tubes at the side. The cell is only adapted for perpendicular illumination of the sample. Although the total number of reflections remains the same because they are defined by the sample's geometry, for the photo isomerization of fulgimide inside the cell the effective sample size is only the illuminated area and thereby the effective amount of reflections is reduced. For the determination of the amidation kinetics only the surface fraction that is in touch with the amidation solution has been considered for the calculation of lost ester groups.

B.3 Analytical models for the switching kinetics

Analytical models are examined to describe the switching kinetics. From the differential equations one would expect first order behavior for the ring opening reaction. Different models are fitted to the switching kinetics using least mean squares using weights of $1/E$ to homogeneously weight all data points.

The photo commutation kinetics for the ring opening reaction of a dense monolayer are fitted by a single and bi exponential functions in the left figure of B.3. The single exponential function does not give satisfying results, neither does a stretched exponential $E(n) = A_1 - A_1 \exp(-(\sigma_{A1}n)^\alpha)$. A bi exponential model $E(n) = A_1 + A_2 - A_1 \exp(-\sigma_{A1}n) - A_2 \exp(-\sigma_{A2}n)$ that a priori has no clear physical motivation can much better describe the data. Furthermore the relative residuals E/E_{model} now a systematical deviations for every model.

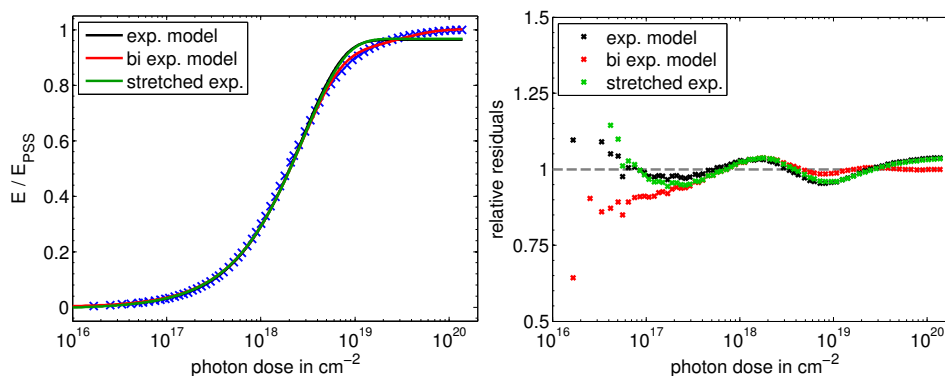


FIGURE B.3: Different exponential models fitted to the ring opening reaction kinetics and relative residuals

Poumellec and Lancry developed an analytical approach for thermally activated kinetics using diverse distributions of activation energies. Thereby different kinetic models are predicted. If the activation energy follows Gaussian, Poisson or sigmoid differentiation distribution the kinetic follows an error function, a power law ($E(n) = A_0 \cdot (1 - (\sigma n)^{-\frac{T}{T_0}})$) or a quotient based model ($E(n) = A_0 \cdot \frac{(\sigma n)^{\frac{T}{T_0}} \exp(\frac{-E_0}{k_B T_0})}{1 + (\sigma n)^{\frac{T}{T_0}} \exp(\frac{-E_0}{k_B T_0})}$), respectively.

In figure B.4 kinetic curves following the different models are shown. The power law does not give satisfying results although diverse initial parameter are used. The errorfunction that corresponds to a normal distribution of the activation energies does not give satisfying results, neither. Better results are obtained for the quotient model that corresponds to sigmoid differentiation distribution of the activation energy. However, again the residuals show a systematical deviations. Additionally the thermal dependence is not predicted correctly. The physical motivation why monolayer

as a more or less disordered media, should lead to sigmoid differentiation distribution of the activation energy is not clear.

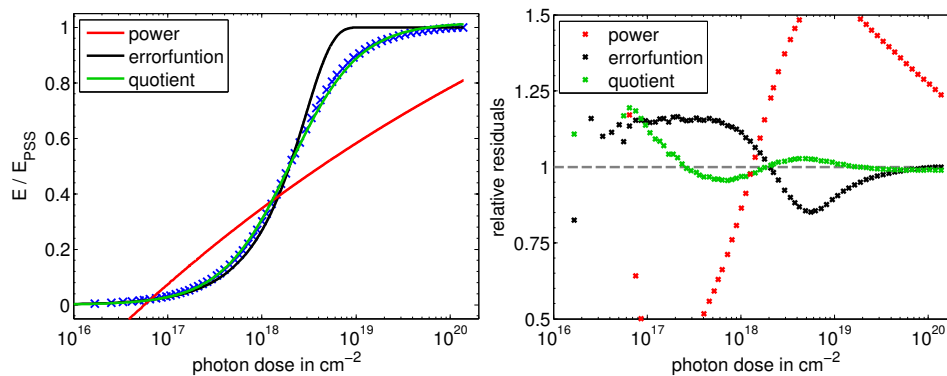


FIGURE B.4: Different analytical models based on different activation energy distributions fitted to the ring opening reaction kinetics and corresponding residuals

B.4 Polarized switching

In figure B.5 the different kinetics curves are shown to determine the cross sections for the ring opening and closing reaction under s and p polarized light.

The ring opening reaction under p-polarized green light shows a similar kinetics for all surface densities (top left). The cross sections are about $0.40 \cdot 10^{-18} \text{ cm}^{-2}$ for the different densities. On the other hand for the ring opening reaction under s-polarized the cross sections are significantly lower compared to p polarization (top right). Furthermore, the cross sections dependent on the photochrome concentration: the lower the photochrome concentration the higher the cross section. The cross section range from $0.12 \cdot 10^{-18} \text{ cm}^{-2}$ for the most diluted until $0.060 \cdot 10^{-18} \text{ cm}^{-2}$ for the densest surface.

The ring closing reaction under p-polarized UV light (bottom left) shows comparable kinetics for all surface densities as it has been observed for the ring opening reaction. The cross sections are about $1.41 \cdot 10^{-18} \text{ cm}^{-2}$ to $1.69 \cdot 10^{-18} \text{ cm}^{-2}$. On the other hand for the ring closing reaction under s-polarized the cross sections show minor differences, too. The cross section vary from $0.40 \cdot 10^{-18} \text{ cm}^{-2}$ to $0.29 \cdot 10^{-18} \text{ cm}^{-2}$. Again the cross section is significantly smaller for s polarization than for p polarization.

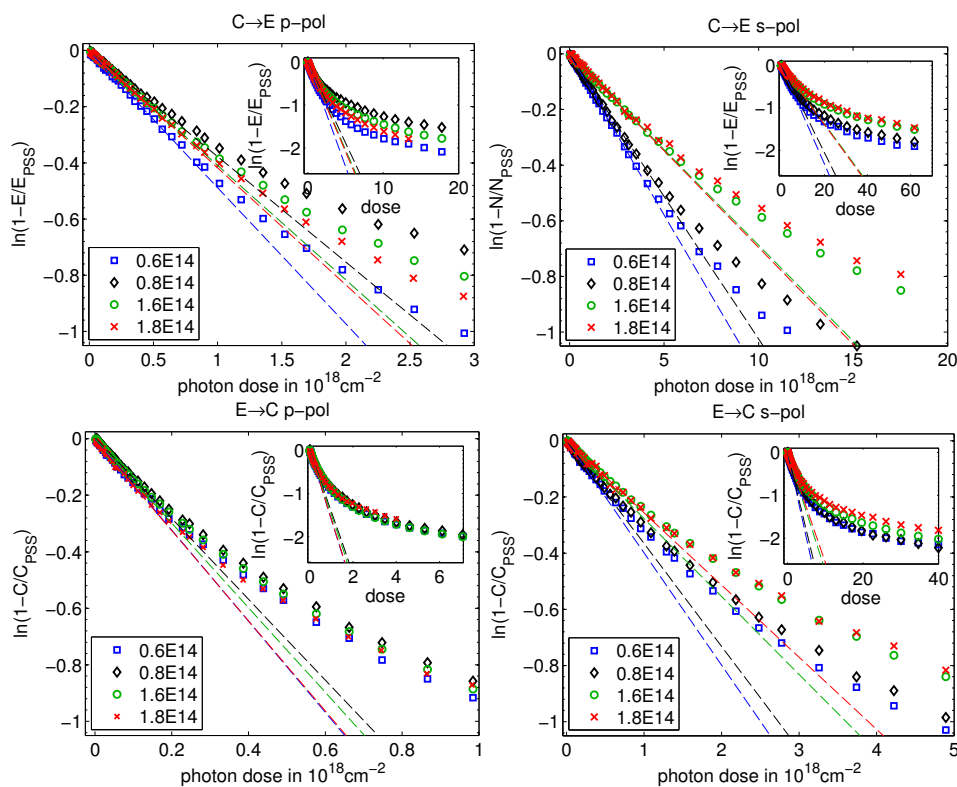


FIGURE B.5: Ring opening C→E (top) and ring closing E→C (bottom) isomerizations kinetics induced by p and s polarized light for different fulgimide densities

B.5 Perpendicular illumination with and without polarizer

The switching kinetics of the ring opening and closing reaction have been studied using perpendicular irradiation ($\theta = 90^\circ$). In perpendicular irradiation the electric field of the incident light has only a parallel component to the surface. A polarizer has been placed inside the beam path to obtain s polarized light. Thereby with polarizer the electric fields are aligned whereas without polarizer the electric fields have an isotropic orientation (figure B.6). Despite the once isotropic and non isotropic orientation of the electric field in both cases the cross sections decrease during the isomerization for the ring opening and closing reaction.

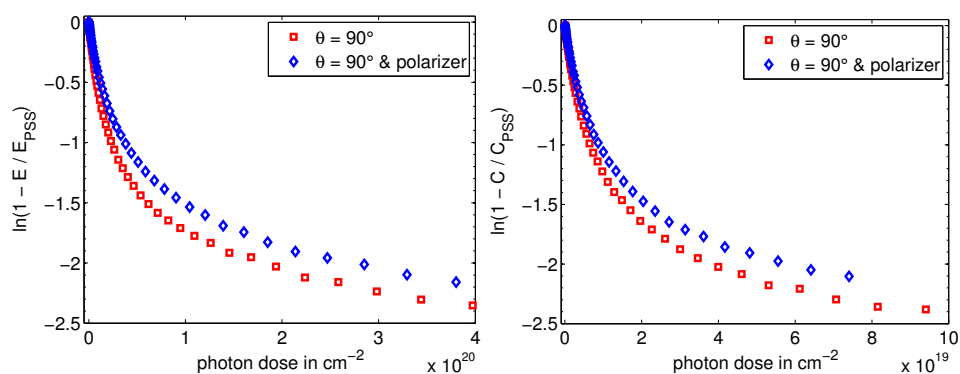


FIGURE B.6: Switching kinetics using perpendicular irradiation with and without polarizer

Appendix C

Supplementary Information for Chapter 4

C.1 Temperature dependent setup

For the investigation of temperature dependent photo isomerizations on surfaces a heatable environment for the sample is necessary. Therefore a specific cell is used that enables temperature dependent in situ measurements of monolayers by infrared spectroscopy[164]. The cell including a mounted sample can be seen in figure C.1. The sample is fixed against a copper block. The temperature of the copper block is measured using a thermocouple. In the direct vicinity of the sample there is a heating resistance that is used to increase the temperature by passing a current. The thermal conditions are improved using two thermal screens around the sample and the heating resistance. The border of the cell is defined by metal block that ensures a homogeneous temperature inside the cell. The infrared beam passes the metal frame using two windows of BaF₂. The cell has initially be constructed to be used until 450 °C, but during the performed experiments the temperature of the cell does not exceed 90 °C.

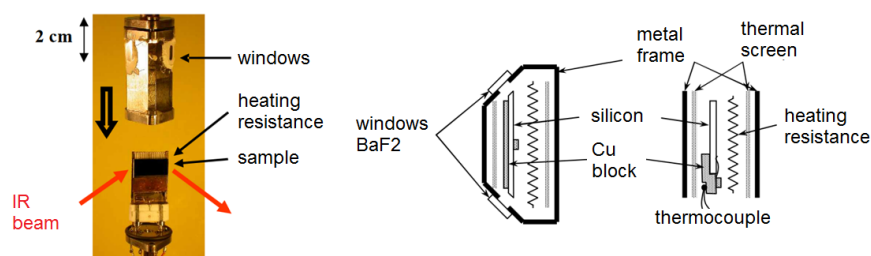


FIGURE C.1: Thermal cell for the temperature dependent photo commutation

C.2 Temperature calibration

The temperature inside the cell can be measured during the experiments using the thermocouple. But for the study of the photo switching properties on surfaces at different temperatures it is essential to be able to illuminate the surface. Consequently the metal frame cannot be used during temperature dependent photo switching. The copper block is slightly enlarged by an aluminum clip so that the sample exceeds the heating resistance and thus facilitates the illumination from the side. The assumption of identical temperatures of the copper block and the sample is not necessarily valid if the metal frame is removed.

An alternative temperature determination of the sample that can be applied to the open cell is therefore necessary.

The substrate of all experiments is silicon, which starts absorb the infrared light for wavenumbers smaller than 1450 cm^{-1} . The infrared absorbance of silicon is temperature dependent. Consequently the temperature dependent infrared absorption of silicon can be used to determine the temperature of the sample.

The temperature dependence of the silicon absorbance needs to be calibrated. To do so a silicon substrate with an acid monolayer is placed inside the sample holder including the thermal windows and the metal frame (as in C.1). The sample is heated by the heating resistance using a current I_{heat} in a range between $I_{heat} = 0 \text{ mA}$ to 300 mA . The temperature measured by the thermocouple inside the cell increases due to the heating and saturates for $I_{heat} = 300 \text{ mA}$ to $T = 83^\circ\text{C}$. For the closed cell the measured temperature at the copper block and the actual temperature of the sample are quasi identical. The infrared absorbance of the heated sample can be determined for different temperatures.

The difference of the infrared absorbance of the silicon substrate for different temperatures is shown in figure C.2. The difference of the infrared absorbance is measured at numerous temperatures T with respect to the same infrared absorbance at $T_{initial}$. The characteristic infrared absorbance of silicon increases with increasing temperature of the sample. The upper red curve corresponds to the highest temperature of $T = 83^\circ\text{C}$. The change of infrared absorbance $\Delta abs_{IR,Si}(T)$ is a function of the temperature as expected.

The change of the infrared absorbance has the same shape for every temperature in the interval between 1000 cm^{-1} and 1450 cm^{-1} . The different curves are homothetic to each other. Therefore one can express the differential infrared absorbance by:

$$\Delta abs_{IR,Si}(T) = \alpha(T) \cdot \Delta abs_{IR,Si}(T = 83^\circ\text{C}) \quad (\text{C.1})$$

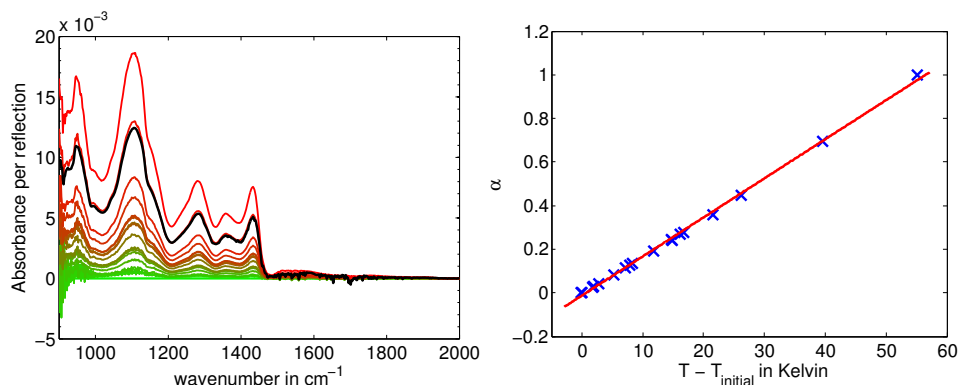


FIGURE C.2: Increase of the infrared absorbance of silicon due to increasing temperature (left). The infrared absorbance can be characterized by the scaling factor α , shown as a function of temperature (right)

The function $\alpha(T)$ is thought a scaling factor between 0 and 1 that includes the temperature difference $T - T_{initial}$. The panel of C.2 shows $\alpha(T)$ for different temperatures using the measurements of the left figure. α is a linear function that is determined by a linear regression to be

$$\alpha(T) = 0.018 \cdot (T - T_{initial}) \quad (C.2)$$

The linearity is important because thereby the difference of the infrared absorption is independent of the initial temperature but only depends on the temperature variation.

C.3 Determination of the temperature before illumination

The photo switching kinetics of fulgimide monolayer is examined as a function of the temperature.

The dense fulgimide surface is switched several times to stabilize the commutation as done for polarization dependent kinetic studies. Then the surface is heated by a forward current until the thermocouple reached the temperature T_{TC} . The maximal variations of T_{TC} has been 0.4°C . Since the cell is not closed for the kinetic studies the forward (heating) current is significantly higher than in the calibration. The temperature of the sample T_{Si} before the different isomerizations has been determined using the temperature dependent infrared absorbance of silicon.

For the temperature dependent measurements the sample is heated by the heating resistance. The change of the infrared absorbance is displayed in figure C.3. The silicon absorbance is increased for a higher heating resistance.

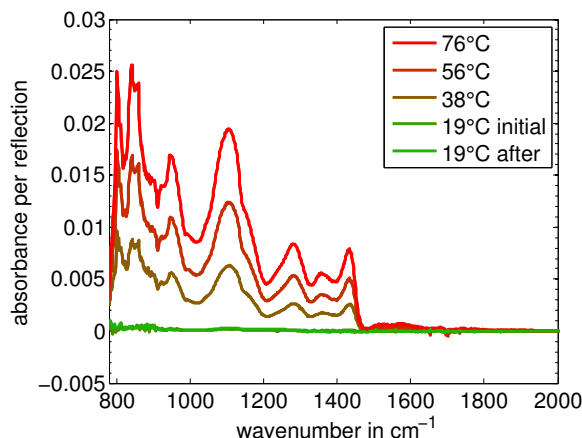


FIGURE C.3: The infrared absorbance for the fulgimide monolayer at different temperatures. The temperatures are determined by the infrared bands of silicon between 1000 cm^{-1} to 1450 cm^{-1} .

The infrared absorbance is used to determine the scaling factor α by equation C.1 using least mean squares in the interval from 1000 cm^{-1} to 1450 cm^{-1} . Subsequently the temperature difference can be calculated for α using equation C.2. The determined temperatures are listed in the legend of the figure.

C.4 Temperature during the irradiation

The temperature before irradiation can be determined by the procedure described above. But during the illumination the temperature of the sample increases by the absorption of the light by the silicon and the organic film. This effect can be estimated in a similar way by measuring the infrared spectrum of the sample during the illumination.

Since temperature dependency of the isomerization is only expected for the ring opening reaction the temperature change is investigated for the illumination of green light. Initially the fulgimide surface is therefore in the PSS^{UV}. The fulgimide monolayer and silicon sample is continuously irradiated by one long light pulse of green light with a photon flux of $1.4 \cdot 10^{17}\text{ cm}^{-2}\text{ s}^{-1}$. The change of the infrared spectra due to the illumination is measured. The scan time is dramatically reduced to obtain information just after the light is turned on.

The differential infrared spectrum due to the illumination is displayed in the panel of figure of C.4 for an illumination duration of 103 s. The infrared absorbance is dominated by free carriers in the n doped silicon that are created by the absorbed light. For the temperature determination this non linear 'baseline' contribution must be corrected. Therefore the free electron and free hole absorbance are subtracted from the initial spectrum

by fitting free electrons and holes using the Drude model (absorbance \propto wavenumber⁻²) and a broad Gaussian peak taking into account the interband transitions [165] (red curve in the left panel of figure C.4). This model has been applied to regions where no other peaks are present. The non linear 'baseline' follows the predicted behavior of the free electron and hole absorbance.

In the right panel of figure C.4 the differential spectrum is displayed after the free carriers correction. The resultant spectrum shows the characteristic temperature features between 1000 cm⁻¹ and 1500 cm⁻¹. The absorbance spectrum is fitted by equation C.1 to determine α . The scaled curve used for the α determination is shown in red and thereby the temperature increase can be determined by equation C.2 in the same way as without radiation.

The peaks between 1600 cm⁻¹ and 1800 cm⁻¹ corresponds to the photo switching of the photochromes and are therefore not respected by the fit.

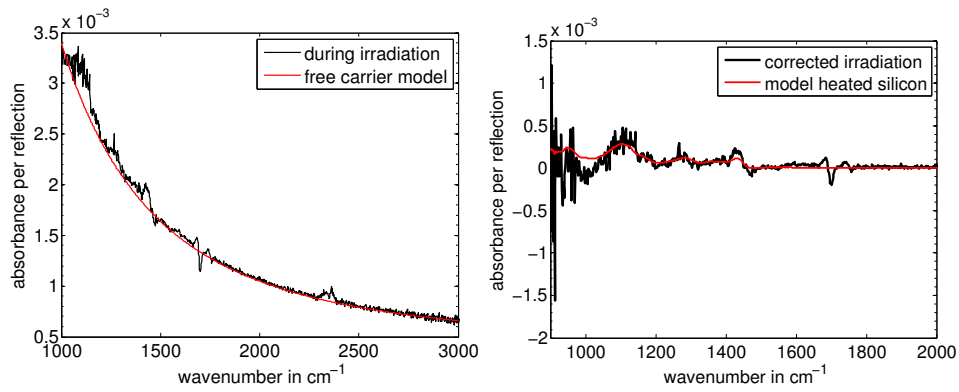


FIGURE C.4: Left: differential infrared spectrum during illumination by visible light (black) and model based of free carrier and interband transitions (red). Right: same infrared spectrum as on the left corrected by the free carrier contributions (black). Model of the differential infrared spectrum due thermally increased silicon absorbance (red).

The temperature of the sample is analyzed while the surface is illuminated by green light with the maximal light flux of $1.4 \cdot 10^{17}$ cm⁻²s⁻¹ in 45°. The corresponding sample temperatures are shown in figure C.5 against the illumination time. The temperature directly increases by 1°C due to illumination. For very long pulse widths the sample temperature increases by around 2.3°C. After the light is turned off the temperature decreases to its initial value within a few seconds.

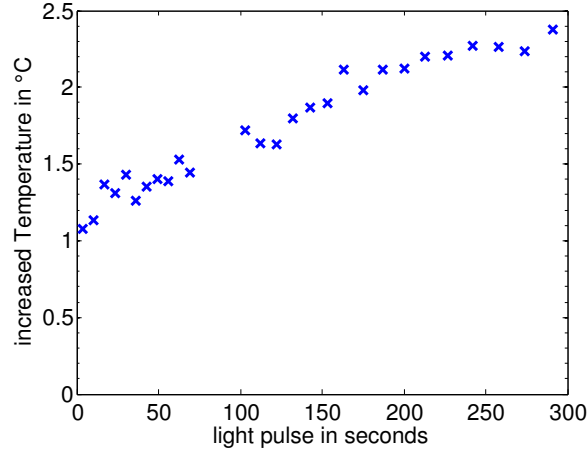


FIGURE C.5: Temperature calibration: during illumination
(2)

C.5 Experimental procedure for temperature dependent measurements

The sample is heated using a heating resistance and a forward current. The temperature dependent infrared absorption of the silicon substrate is used to determine the temperature of the sample. The silicon infrared absorption is calibrated using a thermal cell whose temperature can be measured by a thermocouple.

The measurement cycles and the experimental parameter are shown in table C.1.

reaction	I_{heat} in mA	T_{TC} in °C	T_{Si} in °C	σ in 10^{-18} cm^{-2}
1. C → E (green)	0	19	19	0.41
2. E → C (UV)	0	19	19	1.11
3. C → E (green)	203	40	38	0.46
4. E → C (UV)	202	40	38	1.20
5. C → E (green)	302	60	56	0.60
6. E → C (UV)	302	60	56	1.24
7. C → E (green)	395	80	76	0.70
8. E → C (UV)	392	80	76	1.12
9. C → E (green)	0	19	19	0.40
10. E → C (UV)	0	19	19	1.30

TABLE C.1: Cross sections and temperature T_{Si} for the switching cycles at different temperatures (T_{TC} is the temperature of the sample holder and I_{heat} is the heating current).

C.6 Differential equation for the ring opening reaction

In solution the quantum efficiency η and therefore $\sigma = \eta\sigma_{abs}$ depends on the polarity and viscosity of the solvent but remains constant during the switching because the environment does not change. Therefore solving the definition of the cross section (first order differential equation) $\sigma = -\frac{1}{C\phi} \frac{dC}{dt}$ results in first order kinetics for the ring opening reaction in solution.

On surfaces on the other hand the quantum efficiency $\eta(T)$ of the ring opening reaction is a function of the number of open and closed isomers and therefore changes during the switching of the monolayer. Using the definition of the isomerization cross section and $\sigma = \eta(T)\sigma_{abs}$ a differential equation for the ring opening reaction of fulgimide on surfaces is obtained:

$$\sigma = \sigma_{abs}\eta_1(T)\eta_2(T, l, m) = -\frac{1}{C\phi} \frac{dC}{dt} \quad (C.3)$$

Normalizing the number of isomers $C + E = 1$ and taking the number of irradiated photons per unit surface $n = \phi t$, the differential equation can be rewritten to

$$\frac{dE}{dn} = \sigma_{abs}\eta_1(T)\eta_2(T, l, m)(1 - E) \quad (C.4)$$

The η_1 can be simplified in a first approach to reduce degrees of freedom by $\eta_1(T, E) = A_0 \exp(-E_{act}/k_B T)$ as done before. Thereby the global environmental influence is suppressed in η_1 and only the local environmental influence remains in η_2 . This approximation is justifiable because similar switching kinetics are observed for very different densities of isomers on the surface. We assume a dense surface $l=0$.

The efficiency of the second branching η_2 of the single fulgimide depends on the number of nearest open neighbors m that is only locally defined. In the differential equation describing the whole surface the efficiency η_2 of the single isomer needs to be globalized by replacing the local number of nearest neighbors in the open form m by the average number of nearest neighbors $6E$.

Thereby the differential equation simplifies to

$$\frac{dE}{dn} = \sigma_{abs}A_0 \exp\left(-\frac{E_{act}}{k_B T}\right) \frac{1}{1 + \frac{A_3}{A_4} \exp\left(\frac{\Delta E + 6E \cdot \epsilon_E}{k_B T}\right)} (1 - E) \quad (C.5)$$

C.7 Numerical solution of the differential equation

Even this simplified differential equation has no analytical solution $E(n)$ that could be fitted to the experimental data.

Consequently another strategy to solve the non-linear differential equation is necessary to gain insight whether this model could explain the experimental switching kinetic. Instead of considering the number of switched isomers $E(n)$, the evolution of the cross section σ during the commutation can be addressed to solve the differential equation. Therefore in figure C.6 the cross section

$$\sigma = \sigma_{abs} A_0 \exp\left(-\frac{E_{act}}{k_B T}\right) \frac{1}{1 + \frac{A_3}{A_4} \exp\left(\frac{\Delta E + 6E \cdot \epsilon_E}{k_B T}\right)} \quad (\text{C.6})$$

is fitted to diverse kinetic curves at different temperatures (19°C (green) to 76°C (red)). All fitting parameter for the experiments at different temperatures are optimized in only one least squared optimization of all four experiments at the same time. The optimized parameters are $\sigma_{abs} A_0 = 1.6 \cdot 10^{-17} \text{ cm}^2$, $E_{act} = 95 \text{ meV}$, $\frac{A_3}{A_4} = 2.7 \cdot 10^{-3}$, $\Delta E = -0.0122 \text{ meV}$ and $\epsilon_E = 0.040 \text{ meV}$. The $E_{act} = 95 \text{ meV}$ is the the same order as the determined activation energy in 4.3 of the cross section that are determined at the beginning of each isomerization. The decreasing and thermally activated experimental cross sections are fairly described using this approach. Systematical deviations between the model and the curvature are present.

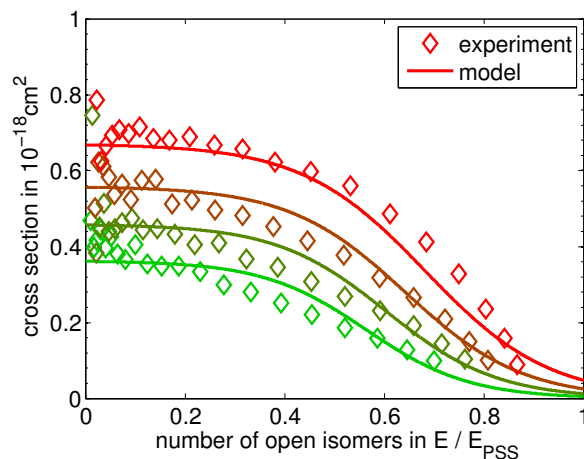


FIGURE C.6: Cross sections of the ring opening reaction at diverse temperatures. The experimental temperatures from green to red are 19, 38, 56 and 76°C, respectively. The analytical model for the cross section is represented by a line.

Using the optimized parameters for the isomerization cross section the differential equation C.5 are numerically solved by the Runge-Kutta method. The obtained kinetic curves for the lowest and highest temperatures are shown in figure C.7. Although systematical errors are present

overall a good agreement is obtained.

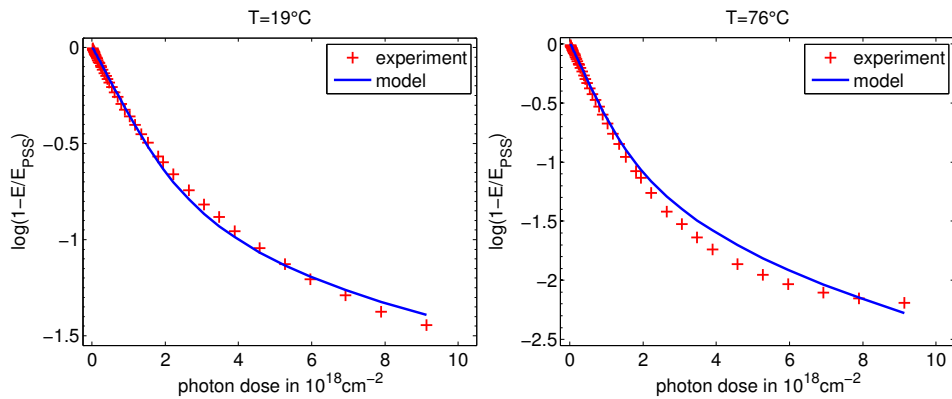


FIGURE C.7: Experimental kinetic curves (red) and solution of the differential equation (blue) for the lowest (left) and highest (right) temperature.

However the differential solution fails to explain the experimental results because of its global nature. Experimentally for the same isomeric composition different cross sections have been measured. The differential equation can not explain this behavior since it only depends on the isomeric composition and is not sensitive to the distribution of the isomers.

C.8 Monte Carlo simulations with different parameter

Using parameter set 1 the influence of different ϵ_{free} is examined in figure C.8. For dense monolayers ϵ_{free} has of course no influence. If ϵ_{free} is 0.1eV the photo commutation is strongly suppressed for dilute monolayers. If ϵ_{free} is smaller than 0.042eV or even negative the switching is strongly enhanced. The cross sections of monolayers with only 10% isomers then show nearly no decreasing cross section but a constant one as in solution (first order kinetics).

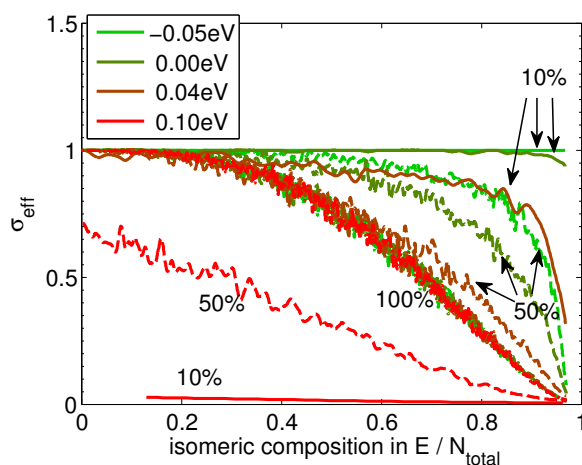


FIGURE C.8: Influence of the ϵ_{free} on the switching kinetics for monolayers with 100%, 50% and 10% photochromes

The same systems that are described 4.3.3 are simulated with the other parameter set. The results for the dilute monolayers are shown in figure C.9, for the different initial surface compositions in C.10.

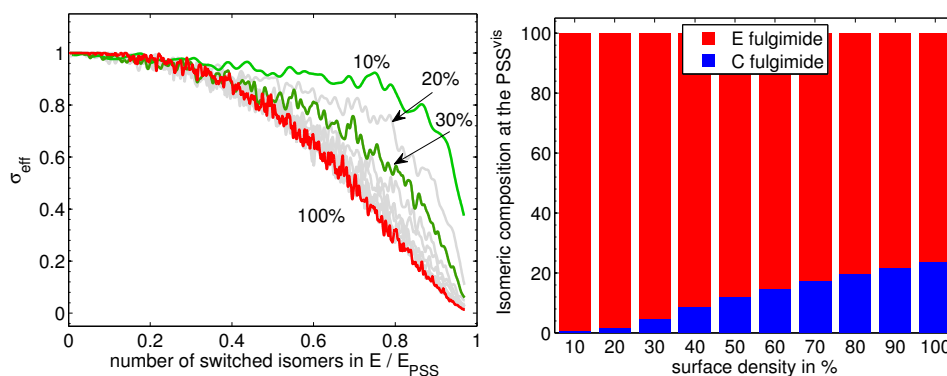


FIGURE C.9: Left: photo switching kinetic for the ring opening reaction of a simulated monolayer with different surface densities using the second parameter set. Right: different PSS for the different monolayers.

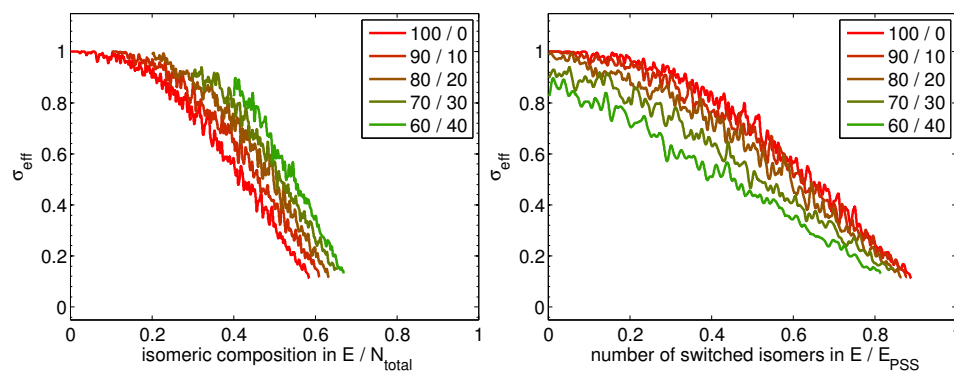


FIGURE C.10: Effective cross sections of the ring opening reaction of a simulated monolayer for different initial isomeric compositions.

Appendix D

Supplementary Information for Chapter 5

D.1 Influence of separate plasmon excitation on the photo commutation

The isomerization of fulgimide, in particular the ring opening reaction, depends on the environment of the photochromes. The potential energy surface of the excited isomers may be influenced by the surface plasmon because the plasmon and the open isomer can interact. A different potential energy surface may influence the quantum efficiency and thereby the cross section. Therefore the influence of a separately excited plasmon on the photo commutation is examined.

The presence of the gold nanoparticles had no influence on the ring closing reaction due to UV light. To study the influence of the visible plasmon on the ring closing reaction anyway the gold nanoparticles are separately excited by the red laser during the intense UV irradiation. To limit the unwanted ring opening reaction excited by the red laser the light flux of the red laser has been decreased by 85% using a neutral filter. Finally the UV photon flux is higher by a factor of about 8.8 compared to the laser photon flux.

The kinetic curve of the ring closing reaction is shown in figure D.1. The 'Fulgimide on AuNP' of figure 5.10 serves as reference of the photo commutation in presence of AuNP that are not separately excited. This reference is displayed by blue crosses. The kinetic curve is displayed against the number of UV photons for both curves. Both kinetic curves are relatively similar. If the surface is only illuminated by UV light the PSS^{UV} is approached quicker than if the red laser excites the back isomerization. However, at the beginning the surface is close to the visible photo-stationary state only few isomers are able to be switched by the red laser. Additionally the red

laser has a lower light flux (factor 8.8) and lower isomerization cross section (factor 28) and therefore its influence can be neglected.

At the beginning both photo commutations are very similar, the cross section for the ring closing reaction with separate plasmon excitation is $1.35 \cdot 10^{-18} \text{ cm}^2$ and therefore very close to the observed $\sigma_{C \rightarrow E}$ before.

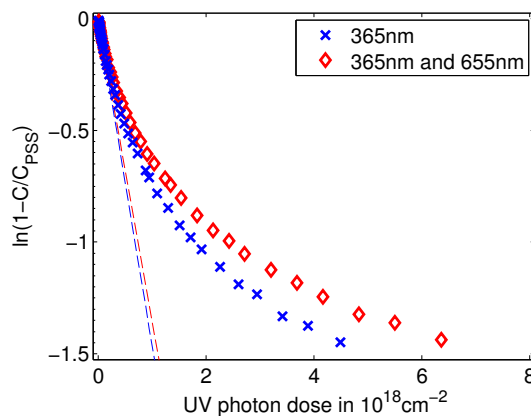


FIGURE D.1: Ring closing reaction of fulgimide with AuNP in the absence (blue) and presence (red) of a separated plasmon excitation by a red laser.

The gold nanoparticles only had a minor influence on the ring opening reaction using light of 525 nm and no positive effect has been observed. Similar to the ring closing reaction during the ring opening reaction with 525 nm the gold plasmon has therefore been separately excited with the red laser. The photon flux of the red laser has been inferior by a factor of 0.45. The kinetic curve of the photo-isomerization using the separate plasmon excitation is shown in red in figure D.2. The kinetic curve is shown against the number of 525 nm photons. The ring opening reaction of the fulgimide monolayer in the presence of gold nanoparticle that has been shown before (5.11) is represented in blue. There is no major influence due to the additional plasmon excitation on the photo commutation.

The cross section using 525 nm with additional plasmon excitation is $2.97 \cdot 10^{-19} \text{ cm}^2$ and therefore increased with respect to the reference without additional plasmon excitation ($2.71 \cdot 10^{-19} \text{ cm}^2$).

The cross section for the ring closing commutation remains unchanged due to the presence of AuNP as depicted in 5.10. The marginal difference of the cross sections of 6% is within the uncertainty of repeated measurements. The presence of the surface plasmon that is separately excited by the red laser had no influence on the photo commutation kinetics of the fulgimide monolayer.

The photo commutation kinetics for the ring opening reaction due to irradiation of green light of 525 nm shows no significant enhancement of the photo commutation cross section (5.11). When the plasmon is excited separately by the red laser the cross section increases slightly. However, this rise

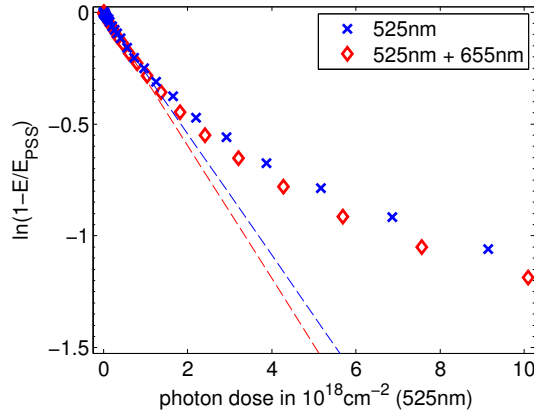


FIGURE D.2: The kinetic curve of photo commutation of fulgimide in the presence of AuNP using green light ($\lambda = 525 \text{ nm}$) with (red) and without (blue) separate plasmon excitation using a red laser (655 nm)

of the cross section corresponds to the independent additional contribution of the red laser on the photo isomerization:

$$\sigma_{Au,525+655nm} \approx \sigma_{Au,525nm} + 0.45 \cdot \sigma_{Au,655nm} \quad (\text{D.1})$$

The factor 0.45 accounts for the lower photon flux of the red laser compared to the green LED.

The unaffected cross section of the ring closing reaction under UV light and non significant increase of the cross section of the ring opening reaction using 525 nm can be explained by the fact that the corresponding photon do not (UV) or only weakly (green) interact with the visible plasmon.

The absence of any influence of the separately induced surface plasmon shows that the amplification of the isomerization cross section is due to the higher absorbance of the photochromes and not by a change in the quantum efficiency. If the surface plasmon would influence the quantum efficiency, the resulting cross section due to both wavelengths $\sigma_{Au,525+655nm}$ would not simply be the addition of $\sigma_{Au,525nm}$ and $\sigma_{Au,655nm}$ because the red laser would change the quantum efficiency in $\sigma_{Au,525nm}$.

D.2 Temperature influence during the photo commutation

The temperature of the sample increases due to the illumination of the sample by light. The increased temperature can be determined by the temperature dependent silicon absorbance. The characteristic silicon absorption spectra after an illumination of the sample with light of 590 nm with and without AuNP are shown in figure D.3.

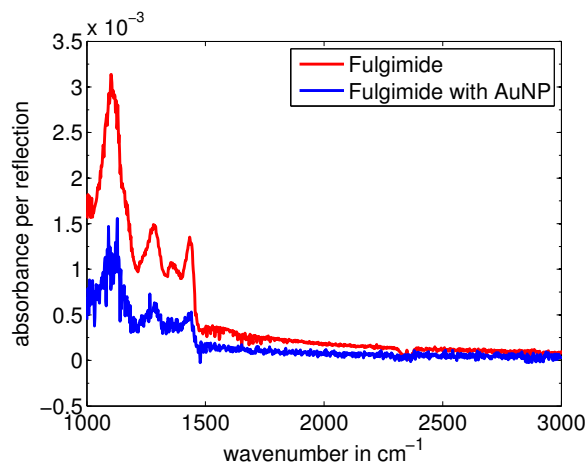


FIGURE D.3: Temperature determination during the irradiation of 590nm light for the fulgimide monolayer with and without AuNP

The increased silicon absorbance band indicate a higher temperature. The temperature increase due to the illumination without AuNP is higher than with AuNP. This is due to the different energy fluxes due to the illumination: without AuNP the sample is illuminated by both sides, with AuNP the only one side is illuminated. Therefore the increase of the cross section due to the nanoparticles can clearly not be explained by temperature effects that would decrease the cross section, but remain however non significant due to the only small temperature change.

Bibliography

- [1] H. Kandori, Y. Shichida, and T. Yoshizawa. "Photoisomerization in rhodopsin". In: *Biochemistry (Moscow)* 66.11 (2001), pp. 1197–1209. ISSN: 00062979. DOI: [10.1023/A:1013123016803](https://doi.org/10.1023/A:1013123016803).
- [2] T. Ebrey and Y. Koutalos. "Vertebrate Photoreceptors". In: *Progress in Retinal and Eye Research* 20.1 (2001), pp. 49–90. DOI: [10.1007/978-4-431-54880-5](https://doi.org/10.1007/978-4-431-54880-5). URL: <http://link.springer.com/10.1007/978-4-431-54880-5>.
- [3] Devens Gust et al. "Data and signal processing using photochromic molecules". In: *ChemComm* (2012), pp. 1947–1957. DOI: [10.1039/c1cc15329c](https://doi.org/10.1039/c1cc15329c).
- [4] Stephan Malkmus et al. "All-optical operation cycle on molecular bits with 250-GHz clock-rate based on photochromic fulgides". In: *Advanced Functional Materials* 17.17 (2007), pp. 3657–3662. ISSN: 1616301X. DOI: [10.1002/adfm.200700553](https://doi.org/10.1002/adfm.200700553).
- [5] Emanuele Orgiu and Paolo Samorì. "25th anniversary article: Organic electronics marries photochromism: Generation of multifunctional interfaces, materials, and devices". In: *Advanced Materials* 26.12 (2014), pp. 1827–1844. ISSN: 15214095. DOI: [10.1002/adma.201304695](https://doi.org/10.1002/adma.201304695).
- [6] Yoshiumi Kohno, Yuuki Tamura, and Ryoka Matsushima. "Simple full-color rewritable film with photochromic fulgide derivatives". In: *Journal of Photochemistry and Photobiology A: Chemistry* 201.2-3 (2009), pp. 98–101. ISSN: 10106030. DOI: [10.1016/j.jphotochem.2008.10.006](https://doi.org/10.1016/j.jphotochem.2008.10.006).
- [7] Pengbo Wan et al. "Host – guest chemistry at interface for photo-switchable bioelectrocatalysis". In: *ChemComm* 47 (2011), pp. 5994–5996. DOI: [10.1039/c1cc11289a](https://doi.org/10.1039/c1cc11289a).
- [8] Jörg Auernheimer et al. "Photoswitched cell adhesion on surfaces with RGD peptides". In: *Journal of the American Chemical Society* 127.46 (2005), pp. 16107–16110. ISSN: 00027863. DOI: [10.1021/ja053648q](https://doi.org/10.1021/ja053648q).
- [9] Yi Chen et al. "Dual-wavelength photochromic fulgides for parallel recording memory". In: *Optical Materials* 28.8-9 (2006), pp. 1068–1071. ISSN: 09253467. DOI: [10.1016/j.optmat.2005.06.006](https://doi.org/10.1016/j.optmat.2005.06.006).
- [10] Xiaowei Pei et al. "Correlation between the structure and wettability of photoswitchable hydrophilic azobenzene monolayers on silicon". In: *Langmuir* 27.15 (2011), pp. 9403–9412. ISSN: 07437463. DOI: [10.1021/la201526u](https://doi.org/10.1021/la201526u).

- [11] By Maria-melanie Russew and Stefan Hecht. "Photoswitches : From Molecules to Materials". In: *Advanced Materials* 22 (2010), pp. 3348–3360. DOI: [10.1002/adma.200904102](https://doi.org/10.1002/adma.200904102).
- [12] T. Nägele et al. "Femtosecond photoisomerization of cis-azobenzene". In: *Chemical Physics Letters* 272.5-6 (1997), pp. 489–495. ISSN: 00092614. DOI: [10.1016/S0009-2614\(97\)00531-9](https://doi.org/10.1016/S0009-2614(97)00531-9). URL: <http://linkinghub.elsevier.com/retrieve/pii/S0009261497005319>.
- [13] I. K. Lednev et al. "Femtosecond Time-Resolved UV- Visible Absorption Spectroscopy of trans-Azobenzene in Solution". In: *J. Phys. Chem* 100.32 (1996), pp. 13338–13341.
- [14] Yasushi Hirose, Hiroharu Yui, and Tsuguo Sawada. "Effect of potential energy gap between the n- π^* and the π - π^* state on ultrafast photoisomerization dynamics of an azobenzene derivative". In: *Journal of Physical Chemistry A* 106.13 (2002), pp. 3067–3071. ISSN: 10895639. DOI: [10.1021/jp0138375](https://doi.org/10.1021/jp0138375).
- [15] Sandra Monti, Giorgio Orlandi, and Paolo Palmieri. "Features of the photochemically active state surfaces of azobenzene". In: *Chemical Physics* 71.1 (1982), pp. 87–99. ISSN: 03010104. DOI: [10.1016/0301-0104\(82\)87008-0](https://doi.org/10.1016/0301-0104(82)87008-0).
- [16] Hermann Rau. "Further evidence for rotation in the π , π^* and inversion in the n, π^* photoisomerization of azobenzenes". In: *Journal of Photochemistry* 26.1964 (1964), pp. 221–225. ISSN: 00472670. DOI: [10.1016/0047-2670\(84\)80041-6](https://doi.org/10.1016/0047-2670(84)80041-6). URL: http://ac.els-cdn.com/0047267084800416/1-s2.0-0047267084800416-main.pdf?{_}tid=bb2db064-0b4f-11e7-824c-00000aacb35e{\&}acdnat=1489782452{_}6eb72790c726182ee338b21643eb6dc4.
- [17] Mason A Wolak et al. "Thermolysis of a Fluorinated Indolylfulgide Features a Novel 1,5-Indolyl Shift". In: *Journal of Organic Chemistry* 66 (2001), pp. 4739–4741.
- [18] Yasushi Yokoyama and Kazuyuki Takahashi. "Trifluoromethyl-substituted Photochromic Indolylfulgide. A Remarkably Durable Fulgide towards Photochemical and Thermal Treatments". In: *Chemistry Letters* (1996), p. 1037.
- [19] Nadezhda I. Islamova et al. "Improving the stability of photochromic fluorinated indolylfulgides". In: *Journal of Photochemistry and Photobiology A: Chemistry* 195.2-3 (2008), pp. 228–234. ISSN: 10106030. DOI: [10.1016/j.jphotochem.2007.10.006](https://doi.org/10.1016/j.jphotochem.2007.10.006).
- [20] K Uchida et al. "Synthesis of Tetrathiafluvalene Derivatives with Photochromic Diarylethene Moieties". In: *Chem. Lett.* 28.10 (1999), pp. 1071–1072. ISSN: 0366-7022.
- [21] Aurélie Perrier, François Maurel, and Denis Jacquemin. "Interplay between electronic and steric effects in multiphotochromic diarylethenes". In: *Journal of Physical Chemistry C* 115.18 (2011), pp. 9193–9203. ISSN: 19327447. DOI: [10.1021/jp201229q](https://doi.org/10.1021/jp201229q).

- [22] Arnaud Fihey et al. "Multiphotochromic molecular systems". In: *Chem. Soc. Rev.* 44.11 (2015), pp. 3719–3759. ISSN: 0306-0012. DOI: [10.1039/C5CS00137D](https://doi.org/10.1039/C5CS00137D). URL: <http://xlink.rsc.org/?DOI=C5CS00137D>.
- [23] Emma C. Harvey et al. "Transition metal functionalized photo- and redox-switchable diarylethene based molecular switches". In: *Coordination Chemistry Reviews* 282-283 (2015), pp. 77–86. ISSN: 00108545. DOI: [10.1016/j.ccr.2014.06.008](https://doi.org/10.1016/j.ccr.2014.06.008). URL: <http://dx.doi.org/10.1016/j.ccr.2014.06.008>.
- [24] Bice He and Oliver S. Wenger. "Ruthenium-phenothiazine electron transfer dyad with a photoswitchable dithienylethene bridge: Flash-quench studies with methylviologen". In: *Inorganic Chemistry* 51.7 (2012), pp. 4335–4342. ISSN: 00201669. DOI: [10.1021/ic300048r](https://doi.org/10.1021/ic300048r).
- [25] Ron T F Jukes et al. "Photochromic Dithienylethene Derivatives Containing Ru(II) or Os(II) Metal Units. Sensitized Photocyclization from a Triplet State". In: *Inorganic Chemistry* 43.9 (2004), pp. 2779–2792. ISSN: 00201669. DOI: [10.1021/ic035334e](https://doi.org/10.1021/ic035334e).
- [26] Arnaud Spangenberg et al. "Photoswitchable interactions between photochromic organic diarylethene and surface plasmon resonance of gold nanoparticles in hybrid thin films". In: *Physical Chemistry Chemical Physics* 15.24 (2013), p. 9670. ISSN: 1463-9076. DOI: [10.1039/c3cp50770j](https://doi.org/10.1039/c3cp50770j). URL: <http://www.ncbi.nlm.nih.gov/pubmed/23665812> <http://xlink.rsc.org/?DOI=c3cp50770j>.
- [27] Evgenii Titov et al. "Thermal Cis-to-Trans Isomerization of Azobenzene-Containing Molecules Enhanced by Gold Nanoparticles: An Experimental and Theoretical Study". In: *Journal of Physical Chemistry C* 119.30 (2015), pp. 17369–17377. ISSN: 19327455. DOI: [10.1021/acs.jpcc.5b02473](https://doi.org/10.1021/acs.jpcc.5b02473).
- [28] Nosrat O. Mahmoodi et al. "Photochromism of azobenzene-thiol-1,3-diazabicyclo-[3.1.0]hex-3-ene on silver nanoparticles". In: *Dyes and Pigments* 118 (2015), pp. 110–117. ISSN: 18733743. DOI: [10.1016/j.dyepig.2015.03.014](https://doi.org/10.1016/j.dyepig.2015.03.014). URL: <http://dx.doi.org/10.1016/j.dyepig.2015.03.014>.
- [29] Sd Evans, Sr Johnson, and H Ringsdorf. "Photoswitching of azobenzene derivatives formed on planar and colloidal gold surfaces". In: *Langmuir* 14.12 (1998), pp. 6436–6440. ISSN: 0743-7463. DOI: [10.1021/la980450t](https://doi.org/10.1021/la980450t). URL: <http://pubs.acs.org/doi/abs/10.1021/la980450t>.
- [30] Atefeh Ghavidast and Nosrat O Mahmoodi. "A comparative study of the photochromic compounds incorporated on the surface of nanoparticles". In: *Journal of Molecular Liquids* 216 (2016), pp. 552–564. ISSN: 0167-7322. DOI: [10.1016/j.molliq.2015.12.014](https://doi.org/10.1016/j.molliq.2015.12.014). URL: <http://dx.doi.org/10.1016/j.molliq.2015.12.014>.

- [31] S. Snegir et al. "Optically controlled properties of nanoparticles stabilised by photochromic difurylene-thene-base diarylethenes". In: *Materialwissenschaft und Werkstofftechnik* 47.2-3 (2016), pp. 229–236. ISSN: 09335137. DOI: [10.1002/mawe.201600472](https://doi.org/10.1002/mawe.201600472). URL: <http://doi.wiley.com/10.1002/mawe.201600472>.
- [32] Jia Su et al. "Giant Amplification of Photoswitching by a Few Photons in Fluorescent Photochromic Organic Nanoparticles". In: *Angewandte Chemie - International Edition* 55.11 (2016), pp. 3662–3666. ISSN: 15213773. DOI: [10.1002/anie.201510600](https://doi.org/10.1002/anie.201510600).
- [33] Zhiyuan Tian, Wuwei Wu, and Alexander D. Q. Li. "Photoswitchable Fluorescent Nanoparticles: Preparation, Properties and Applications". In: *ChemPhysChem* 10.15 (2009), pp. 2577–2591. ISSN: 14394235. DOI: [10.1002/cphc.200900492](https://doi.org/10.1002/cphc.200900492). URL: <http://doi.wiley.com/10.1002/cphc.200900492>.
- [34] Osvaldo N. Oliveira et al. "Optical storage and surface-relief gratings in azobenzene-containing nanostructured films". In: *Advances in Colloid and Interface Science* 116.1-3 (2005), pp. 179–192. ISSN: 00018686. DOI: [10.1016/j.cis.2005.05.008](https://doi.org/10.1016/j.cis.2005.05.008).
- [35] Takahiro Seki et al. "Modulated photoregulation of liquid crystal alignment by azobenzene Langmuir-Blodgett layers: reversible alignment changes of liquid crystals induced by photochromic molecular films, Part 11*". In: *Thin Solid Films* 211 (1992), pp. 836–838.
- [36] Sebastian Hagen et al. "Kinetic analysis of the photochemically and thermally induced isomerization of an azobenzene derivative on Au(111) probed by two-photon photoemission". In: *Applied Physics A: Materials Science and Processing* 93.2 (2008), pp. 253–260. ISSN: 09478396. DOI: [10.1007/s00339-008-4831-5](https://doi.org/10.1007/s00339-008-4831-5).
- [37] E Dulkeith et al. "Fluorescence quenching of dye molecules near gold nanoparticles: radiative and nonradiative effects." In: *Physical review letters* 89.20 (2002), p. 203002. ISSN: 0031-9007. DOI: [10.1103/PhysRevLett.89.203002](https://doi.org/10.1103/PhysRevLett.89.203002).
- [38] Saïd Barazzouk, Prashant V Kamat, and Surat Hotchandani. "Photoinduced electron transfer between chlorophyll a and gold nanoparticles." In: *The journal of physical chemistry. B* 109.2 (2005), pp. 716–723. ISSN: 1520-6106. DOI: [10.1021/jp046474s](https://doi.org/10.1021/jp046474s).
- [39] Matthew J. Comstock et al. "Reversible photomechanical switching of individual engineered molecules at a metallic surface". In: *Physical Review Letters* 99.3 (2007), pp. 1–4. ISSN: 00319007. DOI: [10.1103/PhysRevLett.99.038301](https://doi.org/10.1103/PhysRevLett.99.038301). arXiv: [0612201 \[cond-mat\]](https://arxiv.org/abs/0612201).
- [40] Christopher Bronner and Beate Priewisch. "Photoisomerization of an Azobenzene on the Bi (111) Surface". In: *The journal of physical chemistry C* 117 (2013), pp. 27031–27038. URL: <http://pubs.acs.org/doi/abs/10.1021/jp4106663>.
- [41] Sergii V. Snegir et al. "Switching at the nanoscale: Light- and STM-tip-induced switch of a thiolated diarylethene self-assembly on Au(111)". In: *Langmuir* 30.45 (2014), pp. 13556–13563. ISSN: 15205827. DOI: [10.1021/la5029806](https://doi.org/10.1021/la5029806).

- [42] Yongqiang Wen et al. "Photochemical-controlled switching based on azobenzene monolayer modified silicon (111) surface". In: *Journal of Physical Chemistry B* 109.30 (2005), pp. 14465–14468. ISSN: 15206106. DOI: [10.1021/jp044256t](https://doi.org/10.1021/jp044256t).
- [43] Y Yokoyama and Y Kurita. "Synthesis and Photoreaction of Photochromic Fulgides". In: *Journal of Synthetic Organic Chemistry Japan* 49.5 (1991), pp. 364–372. ISSN: 0037-9980. DOI: [10.5059/yukigoseikyokaishi.49.364](https://doi.org/10.5059/yukigoseikyokaishi.49.364).
- [44] Yasushi Yokoyama. "Fulgides for Memories and Switches". In: *Chemical Reviews* 100.5 (2000), pp. 1717–1740. ISSN: 0009-2665. DOI: [10.1021/cr980070c](https://doi.org/10.1021/cr980070c). URL: <http://pubs.acs.org/doi/abs/10.1021/cr980070c>.
- [45] Thomas Brust et al. "Increasing the efficiency of the ring-opening reaction of photochromic indolylfulgides by optical pre-excitation". In: *Chemical Physics Letters* 489.4-6 (2010), pp. 175–180. ISSN: 00092614. DOI: [10.1016/j.cplett.2010.02.071](https://doi.org/10.1016/j.cplett.2010.02.071). arXiv: [NIHMS150003](https://arxiv.org/abs/NIHMS150003). URL: <http://dx.doi.org/10.1016/j.cplett.2010.02.071>.
- [46] Simone Draxler et al. "Ring-opening reaction of a trifluorinated indolylfulgide : mode-specific photochemistry after pre-excitation". In: *Physical Chemistry Chemical Physics* 11 (2009), pp. 5019–5027. DOI: [10.1039/b819585d](https://doi.org/10.1039/b819585d).
- [47] S. Malkmus et al. "Ultrafast ring opening reaction of a photochromic indolyl-fulgimide". In: *Chemical Physics Letters* 417.1-3 (2006), pp. 266–271. ISSN: 00092614. DOI: [10.1016/j.cplett.2005.10.024](https://doi.org/10.1016/j.cplett.2005.10.024).
- [48] C Slavov et al. "The ultrafast reactions in the photochromic cycle of water-soluble fulgimide photoswitches". In: *Physical Chemistry Chemical Physics* 18 (2016), pp. 10289–10296. ISSN: 1463-9076. DOI: [10.1039/C5CP06866E](https://doi.org/10.1039/C5CP06866E). URL: <http://dx.doi.org/10.1039/C5CP06866E>.
- [49] Florian O. Koller et al. "Ultrafast ring-closure reaction of photochromic indolylfulgimides studied with UV-pump-IR-probe spectroscopy". In: *Journal of Physical Chemistry A* 112.2 (2008), pp. 210–214. ISSN: 10895639. DOI: [10.1021/jp073545p](https://doi.org/10.1021/jp073545p).
- [50] J. Andréasson et al. "Molecular All-Photonic Encoder - Decoder". In: *Journal of the American Chemical Society* (2008), pp. 11122–11128.
- [51] Patricia Remón et al. "An all-photonic molecule-based D flip-flop". In: *Journal of the American Chemical Society* 133.51 (2011), pp. 20742–20745. ISSN: 00027863. DOI: [10.1021/ja2100388](https://doi.org/10.1021/ja2100388).
- [52] A. S. Dvornikov et al. "Spectroscopy and kinetics of a molecular memory with nondestructive readout for use in 2D and 3D storage systems". In: *Journal of Physical Chemistry B* 108.25 (2004), pp. 8652–8658. ISSN: 15206106. DOI: [10.1021/jp031074a](https://doi.org/10.1021/jp031074a).

- [53] E. N. Rodlovskaya et al. "Photochromic fulgimide-containing silicones immobilized on the surface of polyarylate". In: *Polymer Science Series B* 53.5-6 (2011), pp. 352–357. ISSN: 1560-0904. DOI: [10.1134/S156009041105006X](https://doi.org/10.1134/S156009041105006X). URL: <http://link.springer.com/10.1134/S156009041105006X>.
- [54] Sivasankaran Nithyanandan and Palaninathan Kannan. "Photo switchable pendant furyl and thienyl fulgimides containing polypyrroles". In: *Polymer Degradation and Stability* 98.11 (2013), pp. 2224–2231. ISSN: 01413910. DOI: [10.1016/j.polyimdegradstab.2013.08.020](https://doi.org/10.1016/j.polyimdegradstab.2013.08.020). URL: <http://dx.doi.org/10.1016/j.polyimdegradstab.2013.08.020>.
- [55] Catherine Henry De Villeneuve et al. "Quantitative IR readout of fulgimide monolayer switching on Si(111) surfaces". In: *Advanced Materials* 25.3 (2013), pp. 416–421. ISSN: 09359648. DOI: [10.1002/adma.201201546](https://doi.org/10.1002/adma.201201546).
- [56] Karola Rück-Braun et al. "Formation of Carboxy- and Amide-Terminated Alkyl Monolayers on Silicon(111) Investigated by ATR-FTIR, XPS, and X-ray Scattering: Construction of Photoswitchable Surfaces". In: *Langmuir* 111 (2013).
- [57] Michael Schulze et al. "Reversible photoswitching of the interfacial nonlinear optical response". In: *Journal of Physical Chemistry Letters* 6.3 (2015), pp. 505–509. ISSN: 19487185. DOI: [10.1021/jz502477m](https://doi.org/10.1021/jz502477m).
- [58] Long Thang Le Nguyen. "Organization within molecular layers grafted on Si surface and in uence of photo-switching properties of fulgimides groups on surface." PhD thesis. 2014.
- [59] A. Moraillon et al. "Amidation of monolayers on silicon in physiological buffers: A quantitative IR study". In: *Journal of Physical Chemistry C* 112.18 (2008), pp. 7158–7167. ISSN: 19327447. DOI: [10.1021/jp7119922](https://doi.org/10.1021/jp7119922).
- [60] G. S. Higashi et al. "Ideal hydrogen termination of the Si (111) surface". In: *Applied Physics Letters* 56.7 (1990), pp. 656–658. ISSN: 00036951. DOI: [10.1063/1.102728](https://doi.org/10.1063/1.102728). arXiv: [arXiv: 1011.1669v3](https://arxiv.org/abs/1011.1669v3).
- [61] Simone Ciampi, Jason B. Harper, and J. Justin Gooding. "Wet chemical routes to the assembly of organic monolayers on silicon surfaces via the formation of Si–C bonds: surface preparation, passivation and functionalization". In: *Chemical Society Reviews* 39.6 (2010), p. 2158. ISSN: 0306-0012. DOI: [10.1039/b923890p](https://doi.org/10.1039/b923890p). URL: <http://xlink.rsc.org/?DOI=b923890p>.
- [62] P Allongue, C H de Villeneuve, and J Pinson. "Structural characterization of organic monolayers on Si(111) from capacitance measurements". In: *Electrochimica Acta* 45 (2000), pp. 3241–3248.
- [63] Anne Faucheux et al. "Well-defined carboxyl-terminated alkyl monolayers grafted onto H-Si(111): Packing density from a combined AFM and quantitative IR study". In: *Langmuir* 22.1 (2006), pp. 153–162. ISSN: 07437463. DOI: [10.1021/la052145v](https://doi.org/10.1021/la052145v).

- [64] Hidehiko Asanuma, Gregory P. Lopinski, and Hua Zhong Yu. "Kinetic control of the photochemical reactivity of hydrogen-terminated silicon with bifunctional molecules". In: *Langmuir* 21.11 (2005), pp. 5013–5018. ISSN: 07437463. DOI: [10.1021/la0474969](https://doi.org/10.1021/la0474969).
- [65] S. Sam et al. "Semiquantitative study of the EDC/NHS activation of acid terminal groups at modified porous silicon surfaces". In: *Langmuir* 26.2 (2010), pp. 809–814. ISSN: 07437463. DOI: [10.1021/la902220a](https://doi.org/10.1021/la902220a).
- [66] Florian O. Koller et al. "Ultrafast structural dynamics of photochromic indolylfulgimides studied by vibrational spectroscopy and DFT calculations". In: *Journal of Physical Chemistry A* 110.47 (2006), pp. 12769–12776. ISSN: 10895639. DOI: [10.1021/jp0657787](https://doi.org/10.1021/jp0657787).
- [67] Ryoka Matsushima and Hiroshi Sakaguchi. "Comparison of the Photochromic Properties of Fulgides and Fulgimides". In: *Journal of Photochemistry and Photobiology A: Chemistry* 108.2-3 (1997), pp. 239–245. ISSN: 10106030. DOI: [10.1016/S1010-6030\(97\)00095-6](https://doi.org/10.1016/S1010-6030(97)00095-6).
- [68] Nadezhda I. Islamova et al. "Thermal stability and photochromic properties of a fluorinated indolylfulgimide in a protic and aprotic solvent". In: *Journal of Photochemistry and Photobiology A: Chemistry* 199.1 (2008), pp. 85–91. ISSN: 10106030. DOI: [10.1016/j.jphotochem.2008.05.007](https://doi.org/10.1016/j.jphotochem.2008.05.007).
- [69] Bernhard Otto and Karola Rück-Braun. "Syntheses and UV/Vis Properties of Amino-Functionalized Fulgimides". In: *European Journal of Organic Chemistry* 2003.13 (2003), pp. 2409–2417. ISSN: 1434193X. DOI: [10.1002/ejoc.200200680](https://doi.org/10.1002/ejoc.200200680). URL: <http://doi.wiley.com/10.1002/ejoc.200200680>.
- [70] Xi Chen et al. "Synthesis and optical properties of aqueous soluble indolylfulgimides". In: *Journal of Organic Chemistry* 74.17 (2009), pp. 6777–6783. ISSN: 00223263. DOI: [10.1021/jo900909d](https://doi.org/10.1021/jo900909d).
- [71] Yongchao Liang, A. S. Dvornikov, and P. M. Rentzepis. "Synthesis and properties of photochromic fluorescing 2-indolyl fulgide and fulgimide copolymers". In: *Macromolecules* 35.25 (2002), pp. 9377–9382. ISSN: 00249297. DOI: [10.1021/ma020750o](https://doi.org/10.1021/ma020750o).
- [72] Mason A. Wolak et al. "Optical and thermal properties of photochromic fluorinated indolylfulgides". In: *Journal of Photochemistry and Photobiology A: Chemistry* 147.1 (2002), pp. 39–44. ISSN: 10106030. DOI: [10.1016/S1010-6030\(01\)00625-6](https://doi.org/10.1016/S1010-6030(01)00625-6).
- [73] C Slavov et al. "Ultrafast coherent oscillations reveal a reactive mode in the ring-opening reaction of fulgides". In: *Phys. Chem. Chem. Phys* 17 (2015), pp. 14045–14053. DOI: [10.1039/C5CP01878A](https://doi.org/10.1039/C5CP01878A).
- [74] Artur Nenov et al. "Molecular model of the ring-opening and ring-closure reaction of a fluorinated indolylfulgide". In: *Journal of Physical Chemistry A* 116.43 (2012), pp. 10518–10528. ISSN: 10895639. DOI: [10.1021/jp307437f](https://doi.org/10.1021/jp307437f).

- [75] Thomas Brust et al. "Stability and reaction dynamics of trifluorinated indolylfulgides". In: *Chemical Physics Letters* 477.4-6 (2009), pp. 298–303. ISSN: 00092614. DOI: [10.1016/j.cplett.2009.07.013](https://doi.org/10.1016/j.cplett.2009.07.013). URL: <http://dx.doi.org/10.1016/j.cplett.2009.07.013>.
- [76] Thomas Brust et al. "Photochemistry with thermal versus optical excess energy : Ultrafast cycloreversion of indolylfulgides and indolylfulgimides". In: *Journal of Photochemistry and Photobiology A: Chemistry* 207 (2009), pp. 209–216. DOI: [10.1016/j.jphotochem.2009.07.012](https://doi.org/10.1016/j.jphotochem.2009.07.012).
- [77] Thomas Brust et al. "Ultrafast dynamics and temperature effects on the quantum efficiency of the ring-opening reaction of a photochromic indolylfulgide". In: *Journal of Molecular Liquids* 141.3 (2008), pp. 137–139. ISSN: 01677322. DOI: [10.1016/j.molliq.2008.02.011](https://doi.org/10.1016/j.molliq.2008.02.011).
- [78] Simone Draxler et al. "Ultrafast reaction dynamics of the complete photo cycle of an indolylfulgimide studied by absorption, fluorescence and vibrational spectroscopy". In: *Journal of Molecular Liquids* 141.3 (2008), pp. 130–136. ISSN: 01677322. DOI: [10.1016/j.molliq.2008.02.001](https://doi.org/10.1016/j.molliq.2008.02.001).
- [79] B Heinz et al. "Compare photoinduce pericyclic ring open & closure: differences in the excited state pathways". In: *J. Am. Chem. Soc.* 129.27 (2007), pp. 8577–8584. ISSN: 0002-7863. DOI: [10.1021/ja071396i](https://doi.org/10.1021/ja071396i). URL: http://pubs3.acs.org/acs/journals/doilookup?in{_}doi=10.1021/ja071396i.
- [80] J. Voll et al. "Influence of static and dynamical structural changes on ultrafast processes mediated by conical intersections". In: *Journal of Photochemistry and Photobiology A: Chemistry* 190.2-3 (2007), pp. 352–358. ISSN: 10106030. DOI: [10.1016/j.jphotochem.2007.01.032](https://doi.org/10.1016/j.jphotochem.2007.01.032).
- [81] Thorben Cordes et al. "Wavelength and solvent independent photochemistry: the electrocyclic ring-closure of indolylfulgides." In: *Photochemical & Photobiological Sciences* 8.4 (2009), pp. 528–534. ISSN: 1474-905X. DOI: [10.1017/CBO9781107415324.004](https://doi.org/10.1017/CBO9781107415324.004). arXiv: [arXiv:1011.1669v3](https://arxiv.org/abs/1011.1669v3).
- [82] Mason A. Wolak et al. "Tuning the optical properties of fluorinated indolylfulgimides". In: *Journal of Organic Chemistry* 68.2 (2003), pp. 319–326. ISSN: 00223263. DOI: [10.1021/jo026374n](https://doi.org/10.1021/jo026374n).
- [83] G Rothenberger et al. "Solvent influence on photoisomerization dynamics". In: *Journal of Chemical Physics* 79.11 (1983). DOI: [10.1063/1.445699](https://doi.org/10.1063/1.445699).
- [84] Kim M Kerry and Graham R. Fleming. "Influence of solvent on photochemical isomerization: Photophysics of Diphenyl Butadiene in polar solvents". In: *Chemical Physics Letters* 93.4 (1982), pp. 2–6.
- [85] Stephan P. Velsko and Graham X. Fleming. "Solvent influence on photochemical isomerizations: photophysics of DODCI". In: *Chemical Physics* 65 (1982), pp. 59–70.

- [86] Rafal Klajn. "Immobilized azobenzenes for the construction of photoresponsive materials". In: *Pure Applied Chemistry* 82.12 (2010), pp. 2247–2279. DOI: [10.1351/PAC-CON-10-09-04](https://doi.org/10.1351/PAC-CON-10-09-04).
- [87] David T. Valley et al. "Steric hindrance of photoswitching in self-assembled monolayers of azobenzene and alkane thiols". In: *Langmuir* 29.37 (2013), pp. 11623–11631. ISSN: 07437463. DOI: [10.1021/la402144g](https://doi.org/10.1021/la402144g).
- [88] Thomas Moldt et al. "Tailoring the Properties of Surface-Immobilized Azobenzenes by Monolayer Dilution and Surface Curvature". In: *Langmuir* 31 (2015), pp. 1048–1057. DOI: [10.1021/la504291n](https://doi.org/10.1021/la504291n).
- [89] N.R. Krekiah et al. "UV/Vis Spectroscopy Studies of the Photoisomerization Kinetics in Self-Assembled Azobenzene-Containing Adlayers". In: *Langmuir* (2015). DOI: [10.1021/acs.langmuir.5b01645](https://doi.org/10.1021/acs.langmuir.5b01645).
- [90] Ajeet S. Kumar et al. "Reversible photo-switching of single azobenzene molecules in controlled nanoscale environments". In: *Nano Letters* 8.6 (2008), pp. 1644–1648. ISSN: 15306984. DOI: [10.1021/nl080323+](https://doi.org/10.1021/nl080323+).
- [91] Salvatore Sortino et al. "Monitoring photoswitching of azobenzene-based self-assembled monolayers on ultrathin platinum films by UV/Vis spectroscopy in the transmission mode". In: *Journal of Materials Chemistry* 14.5 (2004), p. 811. ISSN: 0959-9428. DOI: [10.1039/b314710j](https://doi.org/10.1039/b314710j). URL: <http://xlink.rsc.org/?DOI=b314710j>.
- [92] Kaoru Tamada, Haruhisa Akiyama, and Tian Xin Wei. "Photoisomerization reaction of unsymmetrical azobenzene disulfide self-assembled monolayers studied by surface plasmon spectroscopy: Influences of side chain length and contacting medium". In: *Langmuir* 18.13 (2002), pp. 5239–5246. ISSN: 07437463. DOI: [10.1021/la0157667](https://doi.org/10.1021/la0157667).
- [93] Lloyd F N Ah Qune et al. "Reversible work function changes induced by photoisomerization of asymmetric azobenzene dithiol self-assembled monolayers on gold". In: *Applied Physics Letters* 93.8 (2008), pp. 1–4. ISSN: 00036951. DOI: [10.1063/1.2969468](https://doi.org/10.1063/1.2969468).
- [94] Belinda Baisch et al. "Mounting freestanding molecular functions onto surfaces: The platform approach". In: *Journal of the American Chemical Society* 131.2 (2009), pp. 442–443. ISSN: 00027863. DOI: [10.1021/ja807923f](https://doi.org/10.1021/ja807923f).
- [95] Ulrich Jung et al. "Azobenzene-containing triazatriangulenium adlayers on Au(111): Structural and spectroscopic characterization". In: *Langmuir* 27.10 (2011), pp. 5899–5908. ISSN: 07437463. DOI: [10.1021/la104654p](https://doi.org/10.1021/la104654p).
- [96] Sergii V. Snegir et al. "STM Observation of Open- and Closed-Ring Forms of Functionalized Diarylethene Molecules Self-Assembled on a Au(111) Surface". In: *The Journal of Physical Chemistry Letters* 2.19 (2011), pp. 2433–2436. ISSN: 1948-7185. DOI: [10.1021/jz200875c](https://doi.org/10.1021/jz200875c). URL: <http://pubs.acs.org/doi/abs/10.1021/jz200875c>.

- [97] Nathalie Katsonis et al. "Reversible conductance switching of single diarylethenes on a gold surface". In: *Advanced Materials* 18.11 (2006), pp. 1397–1400. ISSN: 09359648. DOI: [10.1002/adma.200600210](https://doi.org/10.1002/adma.200600210).
- [98] Kazuki Uchida et al. "Reversible on/off conductance switching of single diarylethene immobilized on a silicon surface". In: *Journal of the American Chemical Society* 133.24 (2011), pp. 9239–9241. ISSN: 00027863. DOI: [10.1021/ja203269t](https://doi.org/10.1021/ja203269t).
- [99] Mina Han et al. "Light-driven molecular switches in azobenzene self-assembled monolayers: effect of molecular structure on reversible photoisomerization and stable cis state." In: *Chemical communications (Cambridge, England)* 46.20 (2010), pp. 3598–3600. ISSN: 1359-7345. DOI: [10.1039/b921801g](https://doi.org/10.1039/b921801g).
- [100] P. Dietrich et al. "An anchoring strategy for photoswitchable biosensor technology: Azobenzene-modified SAMs on Si(111)". In: *Applied Physics A: Materials Science and Processing* 93.2 (2008), pp. 285–292. ISSN: 09478396. DOI: [10.1007/s00339-008-4828-0](https://doi.org/10.1007/s00339-008-4828-0).
- [101] Hidehiko Asanuma, Erin M. Bishop, and Hua-Zhong Yu. "Electrochemical impedance and solid-state electrical characterization of silicon (111) modified with ω -functionalized alkyl monolayers". In: *Electrochimica Acta* 52.8 (2007), pp. 2913–2919. ISSN: 00134686. DOI: [10.1016/j.electacta.2006.08.060](https://doi.org/10.1016/j.electacta.2006.08.060). URL: <http://linkinghub.elsevier.com/retrieve/pii/S0013468606009406>.
- [102] Luuk Kortekaas et al. "A Remarkable Multitasking Double Spiropyran: Bidirectional Visible-Light Switching of Polymer-Coated Surfaces with Dual Redox and Proton Gating". In: *Journal of the American Chemical Society* 138.4 (2016), pp. 1301–1312. ISSN: 15205126. DOI: [10.1021/jacs.5b11604](https://doi.org/10.1021/jacs.5b11604).
- [103] Wesley R. Browne. "Photochemistry of immobilized photoactive compounds". In: *Coordination Chemistry Reviews* 252.23-24 (2008), pp. 2470–2479. ISSN: 00108545. DOI: [10.1016/j.ccr.2008.05.009](https://doi.org/10.1016/j.ccr.2008.05.009).
- [104] Thomas Moldt et al. "Differing Isomerization Kinetics of Azobenzene-Functionalized Self-Assembled Monolayers in Ambient Air and in Vacuum". In: *Langmuir* 32.42 (2016), pp. 10795–10801. ISSN: 15205827. DOI: [10.1021/acs.langmuir.6b01690](https://doi.org/10.1021/acs.langmuir.6b01690).
- [105] Stephan Rath et al. "Periodic organic nanodot patterns for optical memory". In: *Nano Letters* 7.12 (2007), pp. 3845–3848. ISSN: 15306984. DOI: [10.1021/nl072598f](https://doi.org/10.1021/nl072598f).
- [106] Ulrich Jung et al. "Photoswitching behavior of azobenzene-containing alkanethiol self-assembled monolayers on Au surfaces". In: *Langmuir* 26.17 (2010), pp. 13913–13923. ISSN: 07437463. DOI: [10.1021/la1015109](https://doi.org/10.1021/la1015109).
- [107] Oleksii Ivashenko et al. "UV/Vis and NIR Light-Responsive Spiropyran Self-Assembled Monolayers". In: *Langmuir* (2013).
- [108] Bala Krishna Pathem et al. "Surface-Enhanced Raman Spectroscopy to Probe Reversibly Photoswitchable Azobenzene in Controlled Nanoscale Environments". In: *Nano Letters* (2011), pp. 3447–3452.

- [109] Kingo Uchida et al. "Non-destructive readout of the photochromic reactions of diarylethene derivatives using infrared light". In: *Advanced Materials* 15.2 (2003), pp. 121–125. ISSN: 09359648. DOI: [10.1002/adma.200390023](https://doi.org/10.1002/adma.200390023).
- [110] Tamim A. Darwish et al. "Characterizing the photoinduced switching process of a nitrospiropyran self-assembled monolayer using in situ sum frequency generation spectroscopy". In: *Langmuir* 28.39 (2012), pp. 13852–13860. ISSN: 07437463. DOI: [10.1021/la302204f](https://doi.org/10.1021/la302204f).
- [111] Steffen Wagner et al. "Reversible photoisomerization of an azobenzene-functionalized self-assembled monolayer probed by sum-frequency generation vibrational spectroscopy." In: *Physical chemistry chemical physics : PCCP* 11.29 (2009), pp. 6242–6248. ISSN: 1463-9076. DOI: [10.1039/b823330f](https://doi.org/10.1039/b823330f).
- [112] Enrico Benassi et al. "Can Azobenzene Photoisomerize When Chemisorbed on a Gold Surface? An Analysis of Steric Effects Based on Nonadiabatic Dynamics Simulations". In: *Journal of Physical Chemistry C* 119 (2015), pp. 5962–5974. DOI: [10.1021/jp511269p](https://doi.org/10.1021/jp511269p).
- [113] Evgenii Titov et al. "Dynamics of Azobenzene Dimer Photoisomerization : Electronic and steric effects". In: *The Journal of Physical Chemistry Letters* 7 (2016), pp. 3591–3596. DOI: [10.1021/acs.jpcllett.6b01401](https://doi.org/10.1021/acs.jpcllett.6b01401).
- [114] X. L. Zhou, X. Y. Zhu, and J. M. White. "Photochemistry at adsorbate/metal interfaces". In: *Surface Science Reports* 13.3-6 (1991), pp. 73–220. ISSN: 01675729. DOI: [10.1016/0167-5729\(91\)90009-M](https://doi.org/10.1016/0167-5729(91)90009-M).
- [115] Jadranka Dokic et al. "Quantum Chemical Investigation of Thermal Cis-to-Trans Isomerization of Azobenzene Derivatives: Substituent Effects, Solvent Effects, and Comparison to Experimental Data". In: *The Journal of Physical Chemistry A* 113.24 (2009), pp. 6763–6773. ISSN: 1089-5639. DOI: [10.1021/jp9021344](https://doi.org/10.1021/jp9021344). URL: <http://pubs.acs.org/doi/abs/10.1021/jp9021344>.
- [116] J.M. Hicks et al. "Polarity-dependent barriers and the photoisomerization dynamics of molecules in solution". In: *Chemical Physics Letters* 135.4-5 (1987), pp. 413–420. ISSN: 00092614. DOI: [10.1016/0009-2614\(87\)85181-3](https://doi.org/10.1016/0009-2614(87)85181-3). URL: <http://linkinghub.elsevier.com/retrieve/pii/0009261487851813>.
- [117] Thomas Garm Pedersen, P S Ramanujam, and Per Michael Johansen. "Quantum theory and experimental studies of absorption spectra and photoisomerization of azobenzene polymers". In: *Optical Society of America B* 15.11 (1998), pp. 2721–2730.
- [118] J Peretti et al. "Remanent photoinduced birefringence in thin photochromic sol – gel films". In: *Applied Physics Letters* 74.12 (1999), pp. 1657–1659. DOI: [10.1063/1.123645](https://doi.org/10.1063/1.123645).

- [119] Jacques A. Delaire and Keitaro Nakatani. "Linear and Nonlinear Optical Properties of Photochromic Molecules and Materials". In: *Chemical Reviews* 100.5 (2000), pp. 1817–1846. ISSN: 0009-2665. DOI: [10.1021/cr980078m](https://doi.org/10.1021/cr980078m). URL: <http://pubs.acs.org/doi/abs/10.1021/jp0209289><http://pubs.acs.org/doi/abs/10.1021/cr980078m>.
- [120] S R Polo and M Kent Wilson. "Infrared Intensities in Liquid and Gas Phases". In: *J. Chem. Phys.* 23.May 2016 (1955), pp. 2376–2377. ISSN: 00219606. DOI: [10.1063/1.1741884](https://doi.org/10.1063/1.1741884).
- [121] Y.J. CHABAL. "Surface infrared spectroscopy". In: *Surface Science Reports* 8 (1988), pp. 211–357.
- [122] Edward D. Palik. *Handbook of Optical Constants of Solids*. Academic Press Handbook Series, 1985.
- [123] Ryoka Matsushima, Masafumi Nishiyama, and Masamichi Doi. "Improvements in the fatigue resistances of photochromic compounds". In: *Journal of Photochemistry and Photobiology A: Chemistry* 139.1 (2001), pp. 63–69. ISSN: 10106030. DOI: [10.1016/S1010-6030\(00\)00422-6](https://doi.org/10.1016/S1010-6030(00)00422-6).
- [124] Yongchao Liang, a.S Dvornikov, and P.M Rentzepis. "Solvent and ring substitution effect on the photochromic behavior of fluorescent 2-indolylfulgide derivatives". In: *Journal of Photochemistry and Photobiology A: Chemistry* 125.1-3 (1999), pp. 79–84. ISSN: 10106030. DOI: [10.1016/S1010-6030\(99\)00079-9](https://doi.org/10.1016/S1010-6030(99)00079-9).
- [125] Marie Christine Mc. Daniel and Didier Astruc. "Gold Nanoparticles: Assembly, Supramolecular Chemistry, Quantum-Size Related Properties and Applications toward Biology, Catalysis and Nanotechnology". In: *Chemical Reviews* 104 (2004), pp. 293–346. ISSN: 00092665. DOI: [10.1021/cr030698](https://doi.org/10.1021/cr030698). arXiv: [0403600v1](https://arxiv.org/abs/0403600v1) [[arXiv:cond-mat](https://arxiv.org/abs/0403600v1)].
- [126] Prashant V. Kamat. "Photophysical, Photochemical and Photocatalytic Aspects of Metal Nanoparticles". In: *The Journal of Physical Chemistry B* 106.32 (2002), pp. 7729–7744. ISSN: 1520-6106. DOI: [10.1021/jp0209289](https://doi.org/10.1021/jp0209289). URL: <http://pubs.acs.org/doi/abs/10.1021/jp0209289>.
- [127] E Boisselier and D Astruc. "Gold nanoparticles in nanomedicine: preparations, imaging, diagnostics, therapies and toxicity". In: *Chemical Society Reviews* 38.6 (2009), pp. 1759–1782. ISSN: 0306-0012 (Print) 0306-0012 (Linking). DOI: [10.1039/b806051g](https://doi.org/10.1039/b806051g). URL: <http://www.ncbi.nlm.nih.gov/pubmed/19587967><http://pubs.rsc.org/en/content/articlepdf/2009/cs/b806051g><http://www.ncbi.nlm.nih.gov/pubmed/19587967><http://pubs.rsc.org/en/content/articlepdf/2009/cs/b806051g>.
- [128] Partha Ghosh et al. "Gold nanoparticles in delivery applications". In: *Advanced Drug Delivery Reviews* 60.11 (2008), pp. 1307–1315. ISSN: 0169409X. DOI: [10.1016/j.addr.2008.03.016](https://doi.org/10.1016/j.addr.2008.03.016).

- [129] Erik C. Dreaden et al. "The golden age: gold nanoparticles for biomedicine". In: *Chemical Society Reviews* 41.7 (2012), p. 2740. ISSN: 0306-0012. DOI: [10.1039/c1cs15237h](https://doi.org/10.1039/c1cs15237h). URL: <http://xlink.rsc.org/?DOI=C1CS15237H>.
- [130] David A. Giljohann et al. "Gold nanoparticles for biology and medicine". In: *Angewandte Chemie - International Edition* 49.19 (2010), pp. 3280–3294. ISSN: 14337851. DOI: [10.1002/anie.200904359](https://doi.org/10.1002/anie.200904359).
- [131] K Saha et al. "Gold Nanoparticles in Chemical and Biological Sensing". In: *Chemical reviews* 112 (2012), pp. 2739–2779. ISSN: 1520-6890. DOI: [10.1021/cr2001178](https://doi.org/10.1021/cr2001178). arXiv: [NIHMS150003](https://arxiv.org/abs/NIHMS150003).
- [132] John Turkevich, Peter Cooper Stevenson, and James Hiller. "a Study of the Nucleation and Growth Processes I N the Synthesis of Colloidal Gold". In: *Discussions of the Faraday Society* 11.c (1951), pp. 55–75. DOI: [10.1039/DF9511100055](https://doi.org/10.1039/DF9511100055).
- [133] Matthew N. Martin et al. "Charged gold nanoparticles in non-polar solvents: 10-min synthesis and 2D self-assembly". In: *Langmuir* 26.10 (2010), pp. 7410–7417. ISSN: 07437463. DOI: [10.1021/la100591h](https://doi.org/10.1021/la100591h).
- [134] S D Perrault and W C W Chan. "Synthesis and Surface Modification of Highly Monodispersed, Spherical Gold Nanoparticles of 50-200". In: *Journal Of The American Chemical Society* 132.33 (2009), pp. 17042–17043. ISSN: 0002-7863. DOI: [10.1021/ja907069u](https://doi.org/10.1021/ja907069u).
- [135] Mathias Brust et al. "Synthesis of thiol-derivatised gold nanoparticles in a two-phase Liquid–Liquid system". In: *J. Chem. Soc., Chem. Commun.* 7 (1994), pp. 801–802. ISSN: 0022-4936. DOI: [10.1039/c39940000801](https://doi.org/10.1039/c39940000801). URL: <http://xlink.rsc.org/?DOI=C39940000801>.
- [136] Katsuyoshi Ikeda et al. "Plasmonic enhancement of raman scattering on non-SERS-active platinum substrates". In: *Journal of Physical Chemistry C* 113.27 (2009), pp. 11816–11821. ISSN: 19327447. DOI: [10.1021/jp901858t](https://doi.org/10.1021/jp901858t).
- [137] Susie Eustis and Mostafa A. El-Sayed. "Why gold nanoparticles are more precious than pretty gold: Noble metal surface plasmon resonance and its enhancement of the radiative and nonradiative properties of nanocrystals of different shapes". In: *Chem. Soc. Rev.* 35.3 (2006), pp. 209–217. ISSN: 0306-0012. DOI: [10.1039/B514191E](https://doi.org/10.1039/B514191E). arXiv: [NIHMS150003](https://arxiv.org/abs/NIHMS150003). URL: <http://xlink.rsc.org/?DOI=B514191E>.
- [138] Dominik Enders et al. "Surface-enhanced ATR-IR spectroscopy with interface-grown plasmonic gold-island films near the percolation threshold". In: *Physical Chemistry Chemical Physics* 13.11 (2011), p. 4935. ISSN: 1463-9076. DOI: [10.1039/c0cp01450h](https://doi.org/10.1039/c0cp01450h). URL: <http://xlink.rsc.org/?DOI=c0cp01450h>.
- [139] Rostislav Bukasov and Jennifer S. Shumaker-Parry. "Silver nanocrystals with infrared plasmonic properties as tunable substrates for surface enhanced infrared absorption spectroscopy". In: *Analytical Chemistry* 81.11 (2009), pp. 4531–4535. ISSN: 00032700. DOI: [10.1021/ac900477p](https://doi.org/10.1021/ac900477p).

- [140] Fei Le et al. "Metallic nanoparticle arrays: A common substrate for both surface-enhanced Raman scattering and surface-enhanced infrared absorption". In: *ACS Nano* 2.4 (2008), pp. 707–718. ISSN: 19360851. DOI: [10.1021/nn800047e](https://doi.org/10.1021/nn800047e).
- [141] Hidehiro Yamaguchi, Kenji Matsuda, and Masahiro Irie. "Excited-state behavior of a fluorescent and photochromic diarylethene on silver nanoparticles". In: *Journal of Physical Chemistry C* 111.10 (2007), pp. 3853–3862. ISSN: 19327447. DOI: [10.1021/jp065856q](https://doi.org/10.1021/jp065856q).
- [142] J. Zhang, J. K. Whitesell, and M. A. Fox. "Photoreactivity of self-assembled monolayers of azobenzene or stilbene derivatives capped on colloidal gold clusters". In: *Chemistry of Materials* 13.7 (2001), pp. 2323–2331. ISSN: 08974756. DOI: [10.1021/cm000752s](https://doi.org/10.1021/cm000752s).
- [143] Diana Dulić et al. "One-way optoelectronic switching of photochromic molecules on gold." In: *Physical review letters* 91.20 (2003), p. 207402. ISSN: 0031-9007. DOI: [10.1103/PhysRevLett.91.207402](https://doi.org/10.1103/PhysRevLett.91.207402).
- [144] Aurélie Perrier, François Maurel, and Jean Aubard. "Theoretical Study of the Electronic and Optical Properties of Photochromic Dithienylethene Derivatives Connected to Small Gold Clusters". In: *The Journal of Physical Chemistry A* 111.39 (2007), pp. 9688–9698. ISSN: 1089-5639. DOI: [10.1021/jp073436a](https://doi.org/10.1021/jp073436a). URL: <http://pubs.acs.org/doi/abs/10.1021/jp073436a>.
- [145] Päivi Ahonen et al. "Optical switching of coupled plasmons of Ag-nanoparticles by photoisomerisation of an azobenzene ligand." In: *Physical chemistry chemical physics : PCCP* 9.5 (2007), pp. 651–658. ISSN: 1463-9076. DOI: [10.1039/b615309g](https://doi.org/10.1039/b615309g).
- [146] Jingjing Cao et al. "Photo-responsive spiropyran monolayer protected gold nanorod". In: *Dyes and Pigments* 103 (2014), pp. 89–94. ISSN: 01437208. DOI: [10.1016/j.dyepig.2013.11.017](https://doi.org/10.1016/j.dyepig.2013.11.017). URL: <http://dx.doi.org/10.1016/j.dyepig.2013.11.017>.
- [147] Yasuhiro Shiraishi et al. "Light-triggered self-assembly of gold nanoparticles based on photoisomerization of spirothiopyran". In: *Angewandte Chemie - International Edition* 52.32 (2013), pp. 8304–8308. ISSN: 14337851. DOI: [10.1002/anie.201302430](https://doi.org/10.1002/anie.201302430).
- [148] O I Kobeleva et al. "Spectral-kinetic evidence of interaction of photochromic diarylethenes with silver nanoparticles". In: *Optics and Spectroscopy* 109.1 (2010), 101–105 ST –Spectral–kinetic evidence of interac. ISSN: 0030-400X. DOI: [10.1134/s0030400x10070167](https://doi.org/10.1134/s0030400x10070167).
- [149] Abhijit Manna et al. "Optimized photoisomerization on gold nanoparticles capped by unsymmetrical azobenzene disulfides". In: *Chemistry of Materials* 15.1 (2003), pp. 20–28. ISSN: 08974756. DOI: [10.1021/cm0207696](https://doi.org/10.1021/cm0207696).
- [150] Hiroyasu Nishi, Tsuyoshi Asahi, and Seiya Kobatake. "Enhanced photocycloreversion reaction of diarylethene polymers attached to gold nanoparticles in the solid state". In: *Journal of Photochemistry and Photobiology A: Chemistry* 221.2-3 (2011), pp. 256–260. ISSN: 10106030. DOI: [10.1016/j.jphotochem.2011.03.003](https://doi.org/10.1016/j.jphotochem.2011.03.003). URL: <http://dx.doi.org/10.1016/j.jphotochem.2011.03.003>.

- [151] Hiroyasu Nishi, Tsuyoshi Asahi, and Seiya Kobatake. "Plasmonic enhancement of a photocycloreversion reaction of a diarylethene derivative using individually dispersed silver nanoparticles". In: *ChemPhysChem* 13.16 (2012), pp. 3616–3621. ISSN: 14394235. DOI: [10.1002/cphc.201200442](https://doi.org/10.1002/cphc.201200442).
- [152] Florian Schulz et al. "Little Adjustments Significantly Improve the Turkevich Synthesis of Gold Nanoparticles". In: *Langmuir* 30.I (2014), pp. 10779–10784. ISSN: 15205827. DOI: [10.1021/la503209b](https://doi.org/10.1021/la503209b).
- [153] Anna Schaub et al. "Gold nanolayer and nanocluster coatings induced by heat treatment and evaporation technique." In: *Nanoscale research letters* 8.1 (2013), p. 249. ISSN: 1931-7573. DOI: [10.1186/1556-276X-8-249](https://doi.org/10.1186/1556-276X-8-249).
- [154] A. Faucheux et al. "Thermal decomposition of alkyl monolayers covalently grafted on (111) silicon". In: *Applied Physics Letters* 88.19 (2006), pp. 1–4. ISSN: 00036951. DOI: [10.1063/1.2202125](https://doi.org/10.1063/1.2202125).
- [155] A. Faucheux et al. "Mechanisms of thermal decomposition of organic monolayers grafted on (111) silicon". In: *Langmuir* 23.3 (2007), pp. 1326–1332. ISSN: 07437463. DOI: [10.1021/la061260i](https://doi.org/10.1021/la061260i).
- [156] Yong-jun Li, Wei-jun Huang, and Shi-gang Sun. "A Universal Approach for the Self-Assembly of Hydrophilic Nanoparticles into Ordered Monolayer Films at a Toluene/Water Interface**". In: *Angewandte Chemie International Edition* 45 (2006), pp. 2537–2539. DOI: [10.1002/anie.200504595](https://doi.org/10.1002/anie.200504595).
- [157] Yong-Kyun Park, Sang-Hoon Yoo, and SungHo Park. "Assembly of Highly Ordered Nanoparticle Monolayers at a Water/Hexane Interface". In: *Langmuir* 23.21 (2007), pp. 10505–10510. ISSN: 0743-7463. DOI: [10.1021/la701445a](https://doi.org/10.1021/la701445a). URL: <http://pubs.acs.org/doi/abs/10.1021/la701445a>.
- [158] Francois Reincke et al. "Spontaneous Assembly of a Monolayer of Charged Gold Nanocrystals at the Water/Oil Interface". In: *Angewandte Chemie International Edition* 43 (2004), pp. 458–462. DOI: [10.1002/anie.200352339](https://doi.org/10.1002/anie.200352339).
- [159] Katherine C. Grabar et al. "Preparation and Characterization of Au Colloid Monolayers". In: *Analytical Chemistry* 67.4 (1995), pp. 735–743. ISSN: 0003-2700. DOI: [10.1021/ac00100a008](https://doi.org/10.1021/ac00100a008). arXiv: [ac00100a008 \[10.1021\]](https://arxiv.org/abs/ac00100a008). URL: <http://pubs.acs.org/doi/abs/10.1021/ac00100a008>.
- [160] Jithin C. Mohan et al. "Functionalised gold nanoparticles for selective induction of in vitro apoptosis among human cancer cell lines". In: *Journal of Experimental Nanoscience* 8.1 (2013), pp. 32–45. ISSN: 1745-8080. DOI: [10.1080/17458080.2011.557841](https://doi.org/10.1080/17458080.2011.557841). URL: <http://www.tandfonline.com/doi/abs/10.1080/17458080.2011.557841>.
- [161] W. Rechberger et al. "Optical properties of two interacting gold nanoparticles". In: *Optics Communications* 220.1-3 (2003), pp. 137–141. ISSN: 00304018. DOI: [10.1016/S0030-4018\(03\)01357-9](https://doi.org/10.1016/S0030-4018(03)01357-9).

- [162] F. Hecht. "New development in freefem+". In: *Journal of Numerical Mathematics* 20.3-4 (2012), pp. 251–265. ISSN: 15702820. DOI: [10.1515/jnum-2012-0013](https://doi.org/10.1515/jnum-2012-0013).
- [163] Franz Schreier. "Optimized implementations of rational approximations for the Voigt and complex error function". In: *Journal of Quantitative Spectroscopy and Radiative Transfer* 112.6 (2011), pp. 1010–1025. ISSN: 00224073. DOI: [10.1016/j.jqsrt.2010.12.010](https://doi.org/10.1016/j.jqsrt.2010.12.010). URL: <http://dx.doi.org/10.1016/j.jqsrt.2010.12.010>.
- [164] Anne Faucheux. "Nouvelles fonctionnalités de l'interface silicium/dielectrique pour la microelectronique". PhD thesis. 2005.
- [165] H.G.G. Philipsen et al. "In-situ infrared study of silicon in KOH electrolyte: Surface hydrogenation and hydrogen penetration". In: *Surface Science* 644.111 (2016), pp. 180–190. ISSN: 00396028. DOI: [10.1016/j.susc.2015.10.040](https://doi.org/10.1016/j.susc.2015.10.040). URL: <http://linkinghub.elsevier.com/retrieve/pii/S0039602815003441>.

Titre: Photo-isomérisation des photochromes organiques sur des surfaces de silicium

Mots clés: photo-isomérisation, monocouche organique, silicium, interrupteurs moléculaires, FTIR-ATR

Résumé: Dans ce travail, la photo-isomérisation de monocouches (MC) de composés fulgimide a été étudiée. Des isomères de forme *ouverte* (E,Z) ou *fermée* (C) ont été ancrés de façon covalente sur des monocouches organiques fonctionnalisées greffées sur des surfaces hydrogénées de silicium. Leur concentration sur la surface a été déterminée par spectroscopie FTIR en utilisant une méthode d'analyse quantitative basée sur une calibration de l'intensité de bandes d'absorption spécifiques. Les processus d'isomérisation $E,Z \rightleftharpoons C$ sous illumination UV-Vis ont été étudiés par des mesures FTIR *in situ* en fonction de la densité de fulgimides, les conditions d'illumination (intensité et polarisation) et/ou la température.

La cinétique d'isomérisation sur les surfaces a été comparée à celle en solution pour des conditions d'illumination similaires. Des simulations Monte Carlo ont été développées qui permettent de rendre compte des sections efficaces d'isomérisation observées expérimentalement. Les résultats obtenus montrent une isomérisation plus lente sur les surfaces qui peut s'expliquer par i) des intensités de champ électrique local plus faibles sur les surfaces, ii) des effets d'orientation moléculaire et iii) des interactions entre photochromes voisins. Une augmentation de la vitesse de commutation a été observée en présence de nanoparticules d'Or déposées sur les MC de fulgimides résultant d'une amplification du champ électrique local due à des effets de résonance plasmon.

Title: Photo isomerization of organic photochromes on silicon surfaces

Keywords: Photo-isomerization, organic monolayer, silicon, molecular switches, FTIR-ATR

Abstract: In this work the photo-switching properties of fulgimide monolayers (MLs) on silicon surfaces are studied. Open (E,Z) or Closed (C) isomers were anchored through covalent linkage atop of functionalized alkyl monolayers grafted onto oxide free Si surfaces. Their surface concentration was determined by FTIR spectroscopy, using an analysis method based on the calibration of the intensity of specific IR absorption bands. The kinetics of the $E,Z \rightleftharpoons C$ photoisomerization processes were *in situ* investigated by FTIR measurements under UV-Vis illumination as a function of the fulgimide concentration, the illumination conditions (light intensity, polarization) and/or the temperature.

The isomerization kinetic on the surface was compared to that in solution for similar illuminations conditions. Monte Carlo simulations were developed that allows accounting decreasing cross sections observed experimentally. The results evidence less efficient isomerization processes on the surfaces that may be explained by i) a lower intensity of the local electric field on the surface, ii) molecular orientation effects and iii) interactions at molecular scale in between neighbour photochromes. It is also demonstrated that photo-isomerization rates are faster in presence of gold nanoparticles deposited onto the fulgimide ML resulting from local enhancement of the electric field due to plasmon resonance effects.

